



HAL
open science

Oxygen effect in medical ion beam radiation combined with nanoparticles

Marta Bolsa Ferruz

► **To cite this version:**

Marta Bolsa Ferruz. Oxygen effect in medical ion beam radiation combined with nanoparticles. Medical Physics [physics.med-ph]. Université Paris Saclay (COMUE), 2017. English. NNT : 2017SACLS476 . tel-02426213

HAL Id: tel-02426213

<https://theses.hal.science/tel-02426213>

Submitted on 2 Jan 2020

HAL is a multi-disciplinary open access archive for the deposit and dissemination of scientific research documents, whether they are published or not. The documents may come from teaching and research institutions in France or abroad, or from public or private research centers.

L'archive ouverte pluridisciplinaire **HAL**, est destinée au dépôt et à la diffusion de documents scientifiques de niveau recherche, publiés ou non, émanant des établissements d'enseignement et de recherche français ou étrangers, des laboratoires publics ou privés.

Oxygen effect in medical ion beam radiation combined with nanoparticles

Thèse de doctorat de l'Université Paris-Saclay
préparée à l'Université Paris-Sud

École doctorale n°571
Sciences chimiques : molécules, matériaux,
instrumentation et biosystèmes (2MIB)
Spécialité de doctorat : Physique

Thèse présentée et soutenue à Orsay, le 18/12/2017, par

Marta Bolsa Ferruz

Composition du Jury :

Laure Catala Professeur, Université Paris-Sud, Univ. Paris-Saclay, Institut de Chimie Moléculaires et des Matériaux d'Orsay (ICMMO), Orsay, France	Présidente
Kevin Prise Professeur, Queen's University, Centre for Cancer Research and Cell Biology Institute for Health Sciences, Belfast, Royaume Uni	Rapporteur
Jean-Louis Habrand Professeur des universités – praticien hospitalier, Centre de lutte contre le cancer François Baclesse, Caen, France	Rapporteur
Marie-Anne Pehnoat Maître de conférences, Univ. Pierre-et-Marie Curie, Institut de Minéralogie et Physique des Milieux Condensés Paris, France	Examinatrice
Sandrine Lacombe Professeur, Université Paris-Sud, Univ. Paris-Saclay, Institut des Sciences Moléculaires d'Orsay (ISMO) Orsay, France	Directrice de thèse
Erika Porcel Maître de conférences, Université Paris-Sud, Univ. Paris-Saclay, Institut des Sciences Moléculaires d'Orsay (ISMO), Orsay, France	Co-Encadrante de thèse



To my brother,

Contents

List of abbreviations	1
List of Figures	11
List of Tables	14
I Introduction	15
1 Motivation	15
2 State-of-art: nanoparticles for ion beam radiation therapy	19
3 Objectives of this work	23
II Ion Beam Radiation: from elementary processes to the clinic	25
1 Interaction of charged particles with biological matter	26
1.1 General principles	26
1.2 Physical stage	28
1.2.1 Stopping power	28
1.2.2 Interaction of secondary electrons with matter	34
1.2.3 Interaction of charged particles with metallic NPs	35

1.2.4	Electronic processes of relaxation	36
1.3	Radiation chemistry	39
1.3.1	Water radiolysis	39
1.3.2	Reaction of water by-products with biomolecules	42
1.3.3	Effect of molecular oxygen on radiation damage	43
1.3.4	High-LET ion radiolysis of water	44
1.4	Biological impact of radiation in living cells	46
1.4.1	Linear-quadratic model	46
1.4.2	Relative Biological Effectiveness (RBE)	47
1.4.3	Hypoxic tumors and Oxygen Enhancement Ratio (OER)	49
2	Clinical set-ups for Ion Therapy	52
2.1	Passive scattering and Spread Out Bragg peak (SOBP)	55
2.2	Pencil Beam Scanning (PBS)	57
2.3	PBS versus passive scattering (SOBP)	58
III Materials and methods		61
1	Characteristics of nanoparticles	62
1.1	Gold NPs	62
1.2	Platinum NPs	63
2	Cellular models	65
2.1	HeLa cells	65
2.2	BxPC-3 cells	65

CONTENTS

2.3	Cell sample preparation	66
3	Nanoparticles uptake	67
3.1	Localization of NPs in the cells	67
3.2	Quantification of NPs in the cells	68
4	Irradiation protocols under anoxic conditions	70
4.1	Passive scattering	70
4.2	Pencil Beam Scanning	74
4.3	Gamma-rays	78
5	Experimental analysis of radiation effects	79
5.1	Quantification of cell killing by clonogenic survival assay	79
5.2	Quantification of the NP impact: definition of SER, DEF and RBE	80
IV	Results	81
1	Localization of NPs in the cells	82
1.1	Intracellular distribution of PtNPs in HeLa cells	82
1.2	Intracellular distribution of AuNPs in HeLa and BxPC-3 cells	83
1.3	Co-localization of AuNPs with cell organelles in HeLa and BxPC-3 cells	85
1.3.1	Co-localisation of AuNPs with lysosomes	85
1.3.2	Co-localisation of AuNPs with mitochondria	86
1.3.3	Statistical analysis	87
2	Quantification of PtNPs and AuNPs in cells	89

3	Effect of PtNPs and AuNPs on radiation induced cell-killing	91
3.1	Irradiation experiments using passive scattering delivery system	91
3.1.1	Effect of carbon-ion radiation ($LET_d = 50 \text{ keV}/\mu\text{m}$, SOBP width = 6 cm) in HeLa cells	92
3.1.2	Effect of carbon-ion radiation ($LET_d = 50 \text{ keV}/\mu\text{m}$, SOBP width = 6 cm) in BxPC-3 cells	96
3.1.3	Effect of helium-ion beam ($LET_d = 12 \text{ keV}/\mu\text{m}$, SOBP width = 6 cm) in BxPC-3 cells	101
3.1.4	RBE of ion radiation	107
3.2	Irradiation experiments using PBS delivery system	108
3.2.1	Effect of carbon-ion beam ($LET_d = 50 \text{ keV}/\mu\text{m}$, PBS) in HeLa cells	109
3.2.2	Effect of carbon-ion beam ($LET_d = 100 \text{ keV}/\mu\text{m}$, PBS) in HeLa cells	111
V	Discussion	117
1	Summary of the radio-enhancement of NPs activated by ion beams	118
2	Molecular scale effects	119
2.1	From early stage processes to the action of oxygen	119
2.2	Influence of the radiation LET	121
2.3	Dependence of the oxygen effect on the LET	123
3	Influence of NPs on radiation induced effects	124
3.1	Ion radiation using passive scattering delivery system	124
3.2	Ion radiation using PBS delivery system	125

CONTENTS

VI Conclusion and perspectives	127
Bibliography	146
Annex A. List of publications	147
Annex B. Synthèse en français	149
Acknowledgements	153

List of abbreviations

AGuIX Activation-Guided Irradiation by X-ray, Gd-based nanoparticles

ARGENT Advanced Radiotherapy, Generated by Exploiting Nanoprocesses and Technologies

ATCC American Type Culture Collection (non-profit organization)

AuNPs Gold nanoparticles functionalized with DTDTPA

AuNPs-Cy5 Gold nanoparticles functionalized with DTDTPA and tagged with cyanine 5 fluorophore

BRF Bar-Ridge Filter

BxPC-3 Pancreatic cancer cell line

CHO Chinese Hamster Ovary cells

CLUPS Centre Laser de l'Université Paris-Sud (Orsay, France)

CNAO Centro Nazionale di Adroterapia Oncologica, Pavia (Italy)

CPBM Centre de Photonique BioMédical (University Paris Sud, Orsay, France)

CT Computed Tomography

DEA Dissociative Electron Attachment

DEF Dose Enhancing factor

DMEM Dubelcco's Modified Eagle Medium

DMSO Dimethyl sulfoxide

- DNA** Deoxyribonucleic acid
- DTDTPA** Dithiolated derivate of the Diethylene-Triaminepentaacetic Acid
- DU145** Prostate cancer cell
- ESR** Early Stage Researcher
- GSI** Society for Heavy Ion Research (Darmstadt, Germany)
- HBSS** Hank's Balanced Salt Solution
- HeLa** Uterine cervical cancer cell
- HIMAC** Heavy Ion Medical Accelerator (Chiba, Japan)
- HIT** Heidelberg Ion Therapy Centre (Heidelberg, Germany)
- ICP-MS** Inductively Coupled Plasma – Mass Spectrometry
- ISMO** Institut des Sciences Moléculaires d'Orsay (Orsay, France)
- ITN** Initial Training Network
- KEK** High Energy Accelerator Research Organization (Tsukuba, Japan)
- L132** Lung epithelial cells
- LEM** Local Effect Model
- LET** Linear Energy Transfer
- LET_d** Dose-average Linear Energy Transfer
- LQ** Linear-Quadratic
- MDA-MB-231** Breast cancer cell
- MRI** Magnetic Resonance Imaging
- Nano-SIMS** Nanoscale Secondary Ion Mass Spectrometry
- NIRS** National Institute of Radiological Science (Chiba, Japan)
- NPs** Nanoparticles
- OER** Oxygen Enhancement Ratio

LIST OF ABBREVIATIONS

PBS Pencil Beam Scanning

PCC Pearson Correlation Coefficient

PdI Polydispersity Index

PEG Poly(ethylene glycol)

PMMA Polymethyl Metacrylate

PtNPs Platinum core nanoparticles

QST National Institutes for Quantum and Radiological Science and Technology (Chiba, Japan)

RBE Relative Biological Effectiveness

ROS Reactive Oxygen Species

SER Sensitizing Enhancement Ratio

SF Surviving Fraction

SOBP Spread Out Bragg Peak

TEL Transfert d'énergie linéique

TEM Transmission Electron Microscopy

TIFPA Trento Institute for Fundamental Physics and Applications (Trento, Italy)

U-87-MG Glioblastoma cell

UT2A Ultra Trace Analyses Aquitaine technological center (Pau, France)

UTINAM Univers, Temps-fréquence, Interfaces, Nanostructures, Atmosphère et environnement, Molécules (Bourgogne-Franche-Comté University, Besançon, France)

List of Figures

I.1	Illustration of highly penetrating X-ray radiation (A), ballistic effects of ions showing no energy deposition behind the tumor (B) and potential improvement of ion beam radiation effects in the tumor in the presence of nanoparticles (C). (Adapted from Lacombe et al. 2017, Cancer Nanotechnology)	17
I.2	Schematic representation of the amplification effect of nanoparticles at nanoscopic scale (left) and cellular level (right).	20
II.1	Scheme of the interaction processes of radiation with a biological medium as a function of time. These processes are divided into three steps: physical, chemical and biological. Adapted from [Joiner and der Kogel, 2016].	26
II.2	Radiation damage on biomolecules (e.g. DNA) and oxygen fixation of damage. Adapted from [Twentyman, 1993]	27
II.3	Beam energy (dashed line) and deposited energy (solid line) versus penetration depth in the absence of energy loss fluctuations. Adapted from ICRU REPORT 73 [Bimbot et al., 2005].	29
II.4	Stopping power of protons (blue) and carbon-ions in water (red). The red solid line indicates the contribution of electronic stopping power and the dashed line the nuclear stopping power for carbon ions. Adapted from [Schardt et al., 2010]	30

II.5 Monte-Carlo simulations showing individual tracks of secondary electrons produced by fast protons and carbon-ions penetrating tissue. The particles enter at $x = 0$ and move along the z -axis. Adapted from [Krämer, 1995]. 33

II.6 Scheme of possible mechanisms involved in the amplification of ion beam by NPs. (A) Incident ion activating a NPs due to strong coulomb interaction. (B) Interaction of secondary electrons produced in the ion track with NPs. (C) Plasmon excitation. 35

II.7 Electron relaxation via Auger de-excitation process in the case of a $K L_1 L_{23}$ transition. 37

II.8 Electron relaxation via fluorescence process in the case of a $K L_{23}$ transition. 38

II.9 Fluorescence field as a function of the atomic number. Data are based on [Krause, 1979]. 38

II.10 Electron capture on a positively charged nanoparticle. 39

II.11 Scheme of the species produced by water radiolysis. Adapted from [Lousada et al., 2016] 40

II.12 (A) LET values as a function of ion energy per nucleon for six ions [Ziegler, 1998]. (B), (C) and (D): Primary g values of hydrated electron, hydroxyl radical and hydrogen peroxide respectively as a function of LET. In panel (D), solid and open data points correspond to irradiation under anoxic conditions and oxic conditions respectively. Adapted from [Yamashita et al., 2008]. 44

II.13 Linear-quadratic model for high and low LET. Adapted from [Joiner and Van der Kogel, 2009]. 46

II.14 RBE for carbon-ions ($E = 290\text{MeV/u}$, SOBP width = 6cm) relative to cobalt-60 gamma rays as a function of depth in the water phantom. The depths investigated are: "initial plateau" ($\text{LET}_d = 13.7 \text{ keV}/\mu\text{m}$), beginning, middle and end of the 6-cm SOBP ($\text{LET}_d = 40.9, 49.4$ and $70.7 \text{ keV}/\mu\text{m}$, respectively). Adapted from [Gueulette et al., 2004]. 48

II.15 RBE versus mean LET for monoenergetic and extended Bragg peak data using mammalian cell survival data measured <i>in vitro</i> . The cells were irradiated under oxic conditions and the end point was 10% cell survival. The results are compiled from eight different cell systems. Adapted from [Blakely et al., 1983].	49
II.16 From oxic to anoxic cells in tumors. Adapted from [Thambi et al., 2014] .	50
II.17 The Oxygen Enhancement Ratio is shown as a function of the LET for a human cell line. All the data were collected with monoenergetic charged particles and 250 kVp X-rays, for which a LET of 1.3 keV/ μ m was assume. Adapted from [Barendsen, 1968]	51
II.18 Heavy Ion Medical Accelerator facility, Chiba, Japan. http://www.nirs.qst.go.jp/ENG/core/cpt/cpt01.html	53
II.19 Heavy Ion Therapy Centre at Heidelberg (HIT, Germany). Adapted from [Schoemers et al., 2015]	54
II.20 A: Bar-ridge filter. Adapted from [Torikoshi et al., 2007]. B: Depth-dose distribution for a spread-out Bragg peak of a ion beam (dotted line). The dose distribution is created by adding the contribution of several single energy beams (pristine Bragg peak) (solid lines). Scheme adapted from [Terasawa et al., 2009].	55
II.21 The passive beam irradiation system of the treatment and experimental rooms at the HIMAC facility. Adapted from [Kanai et al., 1999]	56
II.22 Pencil beam scanning irradiation system used at HIT facility. Adapted from [Haberer et al., 1993].	58
III.1 (A) Schematic representation of AuNPs. (B) Photograph of AuNPs colloids containing 50 mM Au and 0.5 mM Au. Adapted from [Alric et al., 2013]. .	63
III.2 (A) Schematic representation of PtNPs. (B) Photograph of PtNPs colloids containing 10 mM Pt.	64
III.3 Confocal microscope at the “Centre de Photonique BioMédical” (CPBM), Laser Center of the University Paris Sud (CLUPS) (Orsay, France)	67

III.4 A) Custom-made glass dish. B) Inside of the gas chamber. C) The gas chamber is closed and connected to the control apparatus and the humidifier. D) Gas chamber positioned vertically in front of the ion beam. The chamber moves automatically to the right after each sample has been irradiated. 71

III.5 The gas chamber is placed in front of the beam exit at the irradiation room of HIMAC. 72

III.6 Dose-averaged linear energy transfer (LET_d) as a function of depth in water for spread-out Bragg peak (SOBP) beam of 6 cm width for carbon-ions. Adapted from [Kanai et al., 2006]. 74

III.7 Hypoxic set-up used at HIT. A) Cell support composed of a ring and two biofoils pasted on each side. B) Individual hypoxic chamber. Adapted from [Walter Tinganelli, 2012]. C) Individual chambers connected in between them and to the gas bottle. D) Serie of individual chambers placed vertically on the irradiation table. 75

III.8 LET_d and dose versus the depth for carbon-ion radiation (configuration used to obtain a LET_d of 100 keV/ μ m 35-mm depth). 5 different energy slices within the range from 124.5 to 136.9 MeV/u were scanned to obtain a homogenous LET over a 10 mm depth. 78

III.9 Petri dishes containing HeLa (left) and BxPC-3 colonies (right). They correspond to control samples (0 Gy, no irradiation). 79

IV.1 Nano-SIMS images of a HeLa cell loaded with PtNPs. Panels (A), (B) and (C) correspond to CN^- , P^- and $^{194}Pt^-$ respectively. Panel (D) is the merged image of (B) and (C). The arrows show an identified low concentration P^- region in the cell cytoplasm. 83

IV.2 Merged image of the transmission and fluorescence images of HeLa cells loaded with AuNPs-Cy5 (red) 84

IV.3 Merged image of the transmission and fluorescence images of BxPC-3 cells loaded with AuNPs-Cy5 (red) 84

LIST OF FIGURES

IV.4 Fluorescence image of HeLa cells loaded with LysoTracker (green) (A), AuNPs-Cy5 (0.5 mM, 6 h) (red) (B). (C) is the merged image of (A) and (B) images. 85

IV.5 Fluorescence image of BxPC-3 cells loaded with LysoTracker-green (A), AuNPs-Cy5 (0.5 mM, 6 h) (red) (B). (C) is the merged image of (A) and (B) images. 86

IV.6 Fluorescence image of HeLa cells loaded with Mitotracker (green) (A), AuNPs-Cy5 (0.5 mM, 6 h) (red) (B). (C) is the merged image of (A) and (B) images. 86

IV.7 Fluorescence image of BxPC-3 cells loaded with Mitotracker (green) (A), AuNPs-Cy5 (0.5 mM, 6 h) (red) (B). (C) is the merged image of (A) and (B) images. 87

IV.8 AuNPs and PtNPs per cell internalized in HeLa and BxPC-3 cells. 89

IV.9 Surviving fraction curve for HeLa cells free of NPs (control) irradiated with carbon-ions ($LET_d = 50 \text{ keV}/\mu\text{m}$, SOBP width = 6 cm) in oxic ($pO_2 = 20\%$) and anoxic ($pO_2 = 0\%$) conditions. 92

IV.10 Surviving fraction curve for HeLa cells irradiated with carbon-ions ($LET_d = 50 \text{ keV}/\mu\text{m}$, SOBP width = 6 cm) in the presence of PtNPs (0.5 mM, 6 h incubation) in oxic ($pO_2 = 20\%$) (A) and anoxic ($pO_2 = 0\%$) (B) conditions. The green dashed lines and the purple solid lines indicate the surviving fraction at 2 Gy and the dose at 10% of survival respectively. . . 93

IV.11 Surviving fraction curve for HeLa cells irradiated with carbon-ions ($LET_d = 50 \text{ keV}/\mu\text{m}$, SOBP width = 6 cm) in the presence of AuNPs (0.5 mM, 6 h incubation) in oxic ($pO_2 = 20\%$) (A) and anoxic ($pO_2 = 0\%$) (B) conditions. 94

IV.12 Surviving fraction curve for BxPC-3 cells free of NPs (control) irradiated with carbon-ions ($LET_d = 50 \text{ keV}/\mu\text{m}$, SOBP width = 6 cm) in oxic ($pO_2 = 20\%$), hypoxic ($pO_2 = 0.5\%$) and anoxic ($pO_2 = 0\%$) conditions. . . . 97

IV.13 Surviving fraction curve for BxPC-3 cells irradiated with carbon-ions ($LET_d = 50 \text{ keV}/\mu\text{m}$, SOBP width = 6 cm) in the presence of PtNPs (0.5 mM, 6 h incubation) in oxic ($pO_2 = 20\%$) (A) and anoxic ($pO_2 = 0\%$) (B) conditions. 98

IV.14 Surviving fraction curve for BxPC-3 cells irradiated with carbon-ions ($LET_d = 50 \text{ keV}/\mu\text{m}$, SOBP width = 6 cm) in the presence of AuNPs (0.5 mM, 6 h incubation) in oxic ($pO_2 = 20\%$) (A), hypoxic ($pO_2 = 0.5\%$) (B) and anoxic ($pO_2 = 0\%$) (C) conditions. 99

IV.15 Surviving fraction curve for BxPC-3 cells free of NPs (control) irradiated with helium-ions ($LET_d = 12 \text{ keV}/\mu\text{m}$, SOBP width = 6 cm) in oxic ($pO_2 = 20\%$) and anoxic ($pO_2 = 0\%$) conditions. 102

IV.16 Surviving fraction curve for BxPC-3 cells irradiated with helium-ions ($LET_d = 12 \text{ keV}/\mu\text{m}$, SOBP width = 6 cm) in the presence of PtNPs (0.5 mM, 6 h incubation) in oxic ($pO_2 = 20\%$) (A) and anoxic ($pO_2 = 0\%$) (B) conditions. 103

IV.17 Surviving fraction curve for BxPC-3 cells irradiated with helium-ions ($LET_d = 12 \text{ keV}/\mu\text{m}$, SOBP width = 6 cm) in the presence of AuNPs (0.5 mM, 6 h incubation) in oxic ($pO_2 = 20\%$) (A) and anoxic ($pO_2 = 0\%$) (B) conditions. 104

IV.18 Surviving fraction curve for BxPC-3 cells irradiated with helium-ions ($LET_d = 12 \text{ keV}/\mu\text{m}$, SOBP width = 6 cm) in the presence and absence of DMSO (0.5 mM, 1 h): control cells and cells loaded with AuNPs (0.5 mM, 6 h incubation) in oxic ($pO_2 = 20\%$) (A) and anoxic ($pO_2 = 0\%$) (B) conditions. 106

IV.19 Surviving fraction curve for HeLa (A) and BxPC-3 (B) cells free of NPs (control) irradiated with photon, carbon-ion ($LET_d = 50 \text{ keV}/\mu\text{m}$, SOBP width = 6 cm) and helium-ion ($LET_d = 12 \text{ keV}/\mu\text{m}$, SOBP width = 6 cm) radiation. 107

IV.20 RBE of carbon- and helium-ions for BxPC-3 and HeLa: cells free of NPs (control) and cells loaded with PtNPs or AuNPs (0.5 mM, 6 h incubation). 108

IV.21 Surviving fraction curve for HeLa cells free of NPs (control) irradiated with carbon-ions ($LET_d = 50 \text{ keV}/\mu\text{m}$, PBS) in oxic ($pO_2 = 20\%$) and anoxic ($pO_2 = 0\%$) conditions. 109

IV.22	Surviving fraction curve for HeLa cells irradiated with carbon-ions ($LET_d = 50 \text{ keV}/\mu\text{m}$, PBS) in the presence of AuNPs (1 mM, 6 h incubation) in oxic ($pO_2 = 20\%$) and anoxic ($pO_2 = 0\%$) conditions.	110
IV.23	Surviving fraction curve for HeLa cells free of NPs (control) irradiated with carbon-ions ($LET_d = 100 \text{ keV}/\mu\text{m}$, PBS) in oxic ($pO_2 = 20\%$) and anoxic ($pO_2 = 0\%$) conditions.	112
IV.24	Surviving fraction curve for HeLa cells irradiated with carbon-ions ($LET_d = 100 \text{ keV}/\mu\text{m}$, PBS) in the presence of AuNPs (1 mM, 6 h incubation) in oxic ($pO_2 = 20\%$) (A) and anoxic ($pO_2 = 0\%$) conditions (B).	113
IV.25	Surviving fraction curve for HeLa cells irradiated with carbon-ions ($LET_d = 100 \text{ keV}/\mu\text{m}$, PBS) in the presence and absence of DMSO (1 mM, 1 h): cells free of NPs and cells loaded with AuNPs (0.5 mM, 6 h incubation) in oxic ($pO_2 = 20\%$) condition.	115
V.1	Processes involved in the cells at molecular scale when cells are irradiated by A) carbon-ions, B) carbon-ions in the presence of NPs, C) helium-ions, D) helium-ions in the presence of NPs. The early stage effects (left column), and physico-chemical effects in anoxic (central central) or oxic conditions (right column) are depicted.	120
V.2	Oxidation of organic molecules by $\bullet\text{OH}$ and fixation by O_2	121
V.3	(A) Correlation between carbon ion tracks (red) and a cell layer (cell nucleus in blue) (adapted from [Niklas et al., 2013]). (B) and (C) Scheme of a cell loaded with nanoparticles (black dots) exposed to carbon (red) and helium (green) ion radiation. A larger halo represents a higher LET.	122
VI.1	Oxygen effect in medical ion beam radiation combined with metallic nanoparticles. From nanoscopic mechanisms to cellular effects.	132

List of Tables

IV.1	Quantification of AuNPs and PtNPs in HeLa cells at different time points and initial concentrations.	89
IV.2	Outline of section §3 (Effect of PtNPs and AuNPs on radiation induced cell-killing).	91
IV.3	Table of α and β values for HeLa cells irradiated with carbon-ions ($LET_d = 50 \text{ keV}/\mu\text{m}$, SOBP width = 6 cm) in oxic ($pO_2 = 20\%$) and anoxic ($pO_2 = 0\%$) conditions for cells free of NPs (control) and cells loaded with PtNPs or AuNPs (0.5 mM, 6 h incubation).	95
IV.4	Table of SER and DEF values for HeLa cells irradiated with carbon-ions ($LET_d = 50 \text{ keV}/\mu\text{m}$, SOBP width = 6 cm) in oxic ($pO_2 = 20\%$) and anoxic ($pO_2 = 0\%$) conditions for cells free of NPs (control) and cells loaded with PtNPs or AuNPs (0.5 mM, 6 h incubation).	95
IV.5	Table of α and β values for BxPC-3 cells irradiated with carbon-ions ($LET_d = 50 \text{ keV}/\mu\text{m}$, SOBP width = 6 cm) in oxic ($pO_2 = 20\%$), hypoxic ($pO_2 = 0,5\%$) and anoxic ($pO_2 = 0\%$) conditions for cells free of NPs (control) and cells loaded with PtNPs or AuNPs (0.5 mM, 6 h incubation).	100
IV.6	Table of SER and DEF values for BxPC-3 cells irradiated with carbon-ions ($LET_d = 50 \text{ keV}/\mu\text{m}$, SOBP width = 6 cm) in oxic ($pO_2 = 20\%$), hypoxic ($pO_2 = 0.5\%$) and anoxic ($pO_2 = 0\%$) conditions for cells free of NPs (control) and cells loaded with PtNPs or AuNPs (0.5 mM, 6 h incubation).	101

IV.7	Table of α and β values for BxPC-3 cells irradiated with helium-ions ($LET_d = 12 \text{ keV}/\mu\text{m}$, SOBP width = 6 cm) in oxic ($pO_2 = 20\%$) and anoxic ($pO_2 = 0\%$) conditions for cells free of NPs (control) and cells loaded with PtNPs or AuNPs (0.5 mM, 6 h incubation).	105
IV.8	Table of SER and DEF values for BxPC-3 cells irradiated with helium-ions ($LET_d = 12 \text{ keV}/\mu\text{m}$, SOBP width = 6 cm) in oxic ($pO_2 = 20\%$) and anoxic ($pO_2 = 0\%$) conditions for cells free of NPs (control) and cells loaded with PtNPs or AuNPs (0.5 mM, 6 h incubation).	105
IV.9	RBE of carbon- and helium-ions for BxPC-3 and HeLa: cells free of NPs (control) and cells loaded with PtNPs or AuNPs (0.5 mM, 6 h incubation).	108
IV.10	Table of α and β values for HeLa cells irradiated with carbon-ions ($LET_d = 50 \text{ keV}/\mu\text{m}$, PBS) in oxic ($pO_2 = 20\%$) and anoxic ($pO_2 = 0\%$) conditions for cells free of NPs (control) and cells loaded with AuNPs (1 mM, 6 h incubation).	111
IV.11	Table of α and β values for HeLa cells irradiated with carbon-ions ($LET_d = 100 \text{ keV}/\mu\text{m}$, PBS) in oxic ($pO_2 = 20\%$) and anoxic ($pO_2 = 0\%$) conditions for cells free of NPs (control) and cells loaded with AuNPs (1 mM, 6 h incubation).	113
IV.12	Table of SER and DEF values for HeLa cells irradiated with carbon-ions ($LET_d = 100 \text{ keV}/\mu\text{m}$, PBS) in oxic ($pO_2 = 20\%$) and anoxic ($pO_2 = 0\%$) conditions for cells free of NPs (control) and cells loaded with AuNPs (1 mM, 6 h incubation).	114
V.1	Radio-enhancement of PtNPs and AuNPs activated by helium-ions ($LET_d = 12 \text{ keV}/\mu\text{m}$, SOBP), carbon-ions ($LET_d = 50 \text{ keV}/\mu\text{m}$, SOBP), carbon-ions ($LET_d = 50 \text{ keV}/\mu\text{m}$, PBS) and carbon-ions ($LET_d = 100 \text{ keV}/\mu\text{m}$, PBS) for BxPC-3 and HeLa cells. The following symbology was used: $SER \leq 5\%$ (-), $5\% < SER < 30\%$ (+), $SER \geq 30\%$ (++)	118

Chapter I

Introduction

1 Motivation

With the increased longevity and aging of population combined with an improved control of epidemics and infectious diseases in current times, cancer has become one of the main causes of mortality particularly in the so-called first world. Long periods of convalescence and suffering associated with it have also contributed to raise awareness of an illness that, despite the huge improvements in its treatment over the last decades, is still regarded with despair by patients and their relatives. Surgery, radiation therapy and chemotherapy are currently the standard methods of cancer treatment. About 50% of cancer patients who are healed benefit from radiation therapy alone or in combination with other treatment modalities. The majority of these are treated with “conventional” radiotherapy, which is based on the use of high-energy (2-30 MV) X-rays photons.

Conventional radiotherapy consists in the use of radiation beams traveling through the tissues and allows the treatment of tumors found deep inside the body in a non-invasive way. Unfortunately, radiation is not tumor-selective and damage in healthy tissues is inevitably induced. This can provoke severe side effects or even secondary cancers. Hence, the concentration of the radiation effects within the targeted mass (tumor) is a major challenge in radiation therapies. Major improvements in its efficacy are associated with significant progress in technology such as more effective diagnostic tools and radiation delivery methods [Bhide and Nutting, 2010].

Combination of nanoparticles (NPs) with radiation treatments has attracted increasing interest over the last decade. NPs enhance radiation effects in tumors thanks to their preferential accumulation in cancer cells. The number of works published in specialized journals is now exploding and the first clinical trials using nanoagents composed of heavy elements such as hafnium (NBTXR3) [Bonvalot et al., 2017] and gadolinium (AGuIX) [Kotb et al., 2016a, Verry et al., 2016] (developed respectively by the companies Nanobiotix, Paris, France and Nano-H, St Quentin Fallavier, France) have shown promising results combining nanodrugs and conventional radiotherapy.

Despite conventional radiotherapy being significantly improved by these developments, the use of highly-penetrating photons still results critical for the treatment of tumors located in sensitive organs [?] (i.e. eyes, brain, spinal cord) or the treatment of pediatric cases in which damage of surrounding tissues can have lifelong consequences [Laprie et al., 2015]. Moreover, conventional radiotherapy seems unable to eradicate rare but highly aggressive radioresistant cancers such as glioblastoma and chordoma, for which treatment outcomes remain poor. In particular tumors containing regions of low oxygen concentration or hypoxia – generated by insufficient vascularization of solid tumors – presents resistance to many drugs and conventional radiotherapy.

Cells located at a sufficiently long distance from a functional blood vessel can become deprived of oxygen and nutrients. The radioresistance of hypoxic cells is a result of a lack of oxygen in the radiochemical process by which ionizing radiation impacts cells. The magnitude of this phenomenon is well described by the oxygen enhancement ratio (OER), i.e. the ratio between the dose needed at low oxygen concentration and the dose needed in oxygenated conditions that reaches the same biological effect (for photons, the OER is ≈ 3).

Ion therapy (also called ion beam therapy or hadrontherapy), a modality of radiation therapy based on the use of charged atoms accelerated to high energies (70 to 400 MeV/u), is proposed as a superior technique to eradicate radioresistant tumors as well as those located in critical organs. The advantage of ions stems from their physical properties to interact with matter and the resulting energy deposition. The main characteristic of ions is the differential energy deposition, which is low at the beginning of the track and reaches a peak at the end of their trajectory (the Bragg peak). By correctly choosing the energy of the ions, they can be stopped in the tumor, contrary to X-rays, which cross through the entire body (figure I.1 A and B). The depth and the magnitude of the Bragg peak is determined by the mass and energy of the particle.

1. MOTIVATION

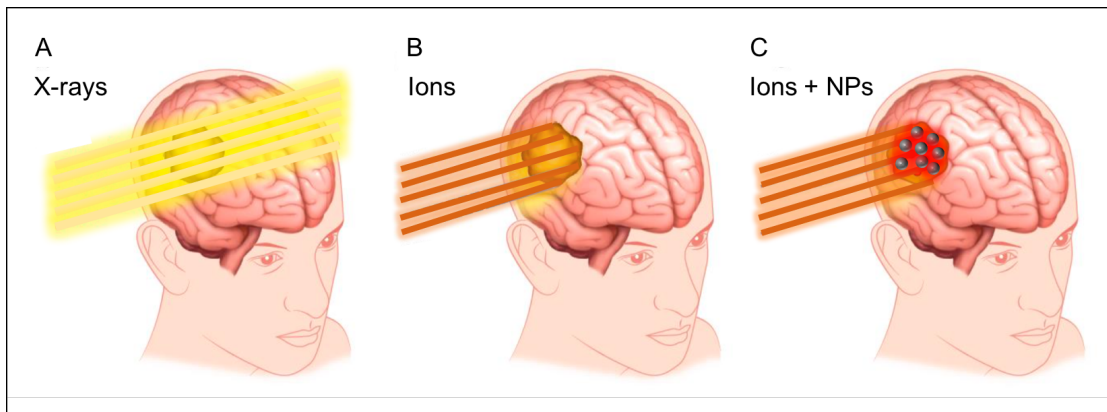


Figure I.1: Illustration of highly penetrating X-ray radiation (A), ballistic effects of ions showing no energy deposition behind the tumor (B) and potential improvement of ion beam radiation effects in the tumor in the presence of nanoparticles (C). (Adapted from Lacombe et al. 2017, *Cancer Nanotechnology*)

The high-energy deposition at the end of the track has strong consequences for the response of biological systems. Ions therefore increase the efficiency of cell-killing compared with photons, which is characterized by the Relative Biological Effectiveness (RBE). The determination of this value is quite complex since it depends on the type of particle, the energy used in the beams, the dose, the dose per fraction, the type of tissue or the biological end point, among other variables. The treatment with ions is less sensitive to the cell cycle compared to conventional radiotherapy, which also represents a remarkable advantage for the treatment of slow-growth tumors. Ion therapy is also the best option for the treatment of hypoxic tumors because ion-induced complex damages decrease the dependence on the oxygen concentration.

Nonetheless, a major limitation of ion therapy is the low but significant dose deposited at the entrance of the track before reaching the tumor (figure I.1B). In order to overcome this limitation, the group at Institut des Sciences Moléculaires d'Orsay (ISMO, Orsay, France) proposed some years ago a new strategy based on the use of high-Z NPs to amplify the effect of ions in the tumor [Porcel et al., 2010] (figure I.1C).

Ion therapy is as explained indicated to treat radioresistant tumors. However these tumors often host hypoxic regions. In order to design treatments using NPs, it is therefore urgent to characterize the influence of oxygen on the radio-enhancement effect evidenced before by the group.

The goal of my thesis has been to study the influence of oxygen on medical ion radia-

tion effects in the presence of gold and platinum NPs. This was performed using two radioresistant human cancer cell lines: HeLa (uterine cervix) and BxPC-3 (pancreas). Different radiation modalities used in current ion therapy centers were probed: carbon and helium ion beams delivered by a passive scattering delivery system and carbon ion beams delivered by a pencil beam scanning system.

2 State-of-art: nanoparticles for ion beam radiation therapy

The effect of high-Z compounds to improve ion beam radiation was first demonstrated at molecular scale using platinum complexes and helium ions (143 MeV/u, LET = 2.24 keV/ μm) as ionizing radiation [Usami et al., 2005]. DNA plasmids were used to probe the induction of bio-damage at nanoscale. In particular, Usami and co-workers demonstrated for the first time that the induction of complex breaks is strongly amplified in the presence of platinum. Later, they demonstrated that these platinum complexes amplify the effect of carbon ions (290 MeV/u, LET_d = 13 and 70 keV/ μm) in mammalian cells [Usami et al., 2008]. The production of hydroxyl radicals was attributed to the action of platinum. More interestingly, the authors demonstrated that high-Z agents amplify the radiation effects even though they are localized in the cytoplasm of the cells and not in the nucleus.

Kim and co-workers demonstrated the effectiveness of high-Z NPs to amplify the proton radiation effects [Kim et al., 2012]. They observed that NPs composed of gold or iron (diameter 1.9 - 14 nm) enhance the regression of mouse tumors treated with fast protons (40 MeV). The efficiency of gold NPs to enhance the effects of proton radiation was confirmed *in vitro* by the experiments of Polf and co-workers using 44-nm gold NPs and 160-MeV protons [Polf et al., 2011]. Tumor regression and mice survival treated by 40-MeV protons was shown to be related to the production of Reactive Oxygen Species (ROS) [Kim et al., 2012]. This result was in agreement with the results obtained with platinum-complexes, which demonstrated the major role of hydroxyl radicals in amplification of the cell-killing.

Jeyne and co-workers did not find any amplification of the cell-killing combining 50-nm gold NPs with 3-MeV proton radiation in bladder cancer cells [Jeynes et al., 2014]. On the contrary, *in vitro* studies in human squamous carcinoma exposed to 1.3 MeV proton radiation in the presence of 5- and 10-nm gold NPs showed an amplification effect [Li et al., 2016].

More recently, the group at ISMO studied the molecular damage induced by 150-MeV proton radiation in plasmids used as nano-bio-dosimeters, when platinum and gadolinium-based NPs are added [Schlatholter et al., 2016]. They observed a clear amplification of nanosize damages due to the production of hydroxyl radicals. More important, they established that the damage was more pronounced in the region of the Bragg peak than in the entrance region of the tracks.

The first evidence of the efficacy of metal NPs to amplify radiation effects of carbon ions was found by the group in 2010 (figure I.2) [Porcel et al., 2010]. This was performed at molecular scale using platinum NPs in combination with carbon ion beams of 290 MeV/u (LET = 13 and 110 keV/ μm). The major role of hydroxyl radicals was highlighted. Interestingly, a significant role of the nanoparticle design (concentration of the metallic atoms in nanoparticle) was observed. Metallic NPs were more efficient than metallic complexes at the same concentration.

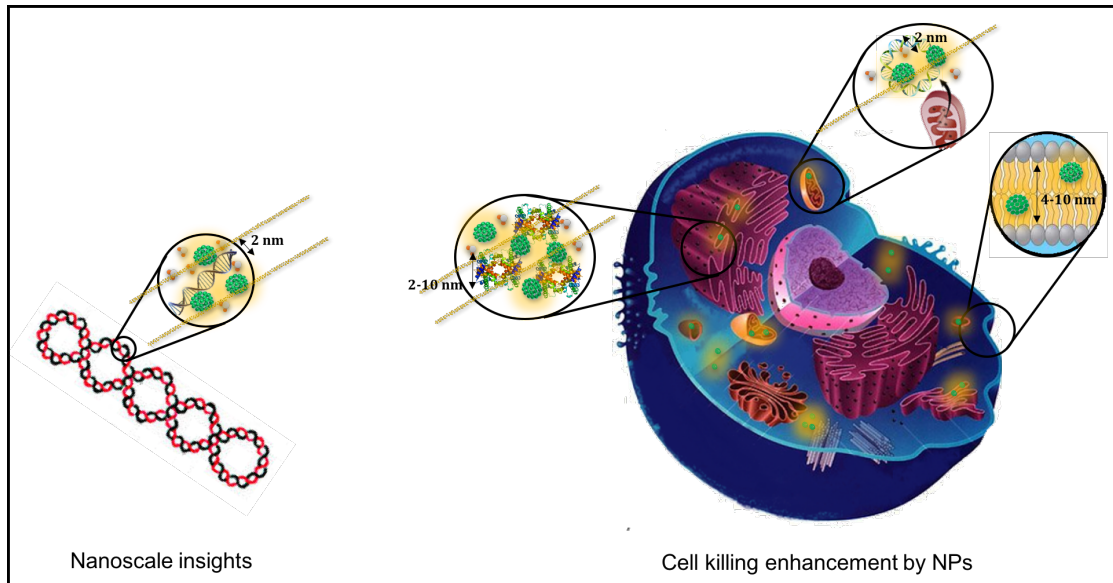


Figure I.2: Schematic representation of the amplification effect of nanoparticles at nanoscopic scale (left) and cellular level (right).

Later, Kaur and co-workers have shown that gold NPs (Glu-AuNPs, 5 nm diameter, 5.5 $\mu\text{M}/\text{mL}$ and an incubation time of 6 h) amplify cell-killing of uterine cervical cancer cells (HeLa) treated with carbon ion radiation (62 MeV, LET = 290 keV/ μm) [Kaur et al., 2013]. They obtained a dose reduction of 29% for Glu-AuNPs.

Cell-killing enhancement in HeLa cells loaded with gold NPs (14 nm diameter, citrate-capped) and irradiated by carbon ions (165 MeV/u, LET = 30 keV/ μm) has been also reported [Liu et al., 2015]. The radio-enhancement effect was found to be concentration dependent: the maximum enhancement factor of hydroxyl radical production was found at 5.52 $\mu\text{g}/\text{ml}$ (0.028 mM) for carbon-ions and 3.66 $\mu\text{g}/\text{ml}$ (0.017 mM) for X-rays radiation (after 24 h of incubation).

The amplification of medical carbon radiation effects was also evidenced using MRI

active compounds such as gadolinium based nanoagents. Porcel and co-workers demonstrated that AGuIX NPs (Nanobiotix, Lyon, France) increase cell-killing when treated with carbon ion radiation (280 MeV/u, $LET_d = 13 \text{ keV}/\mu\text{m}$) [Porcel et al., 2014]. NPs were found located in the cytoplasm, which confirmed that the primary mechanisms responsible for the enhancement of cell-killing are initiated out of the nucleus. This study opened the perspective to implement theranostics (diagnosis and therapy) in carbon ion therapy. More recently experiments combining carbon-ions ($E = 75 \text{ MeV/u}$, $LET = 33.6 \text{ keV}/\mu\text{m}$) with AGuIX confirmed the results of Porcel and co-workers [Wozny et al., 2017].

The simulation of the nanoscale mechanisms involved by NPs was firstly evaluated in the case of photon irradiation. The amplification of radiation effects was explained in terms of a nanoscale enhancement of the local dose close to the NPs. This was demonstrated by McMahan and co-workers [McMahan et al., 2011] through adapting the Local Effect Model (LEM) [Scholz and Kraft, 1996], which was initially developed for ion beams. It was seen that simply including the high local enhancement of the dose due to Auger electrons emitted from the NPs leads to a significant effect on the radial dose.

In the case of ion beam radiation, an amplification of radiation effects has been observed in the presence of NPs through different experimental studies. However, the explanation given for photons is not valid for ions since the dose is already highly localized along the tracks. In this case the enhancement of radiation effect is not understood yet. The first study approaching this problem has been done using the particle track structure code [Krämer and Kraft, 1994] to analyze at nanoscale a possible dose enhancement in high-Z (Au, Pt, Ag, Fe and Gd) NPs traversed by proton beam [Walzlein et al., 2014]. A relevant increase in local dose around the nanoparticle was found, but the relative enhancement was much smaller than in photon irradiation. The simulation was performed in the condition of ion traversing across the nanoparticle, which with typical fluencies adopted in protontherapy ($10^6 - 10^9 \text{ cm}^{-2}$) rarely occurs. Using Monte Carlo (GATE/GEANT4-DNA code) for simulating the dose deposition of proton radiation in the presence of Au and Gd NPs, Martinez-Rovira and Prezado found a very small increase in the dose deposition localized within 1-3 nm from the nanoparticle surface and concludes that the physical effects as consequence of NPs activation may not be the main responsible of the amplification effect observed in previous biological studies [Martinez-Rovira and Prezado, 2015]. Lin and co-workers demonstrated the need of a much higher concentration of NPs in case of protons as compared to photons, in order to observe a relevant enhancement effect [Lin et al., 2015]. This concentration should

further increase at lower proton energies.

Verkhovtsev and co-workers proposed the channel of surface plasmon excitation, which was shown to couple strongly to a high production of secondary electrons, thus arguing a possible new component for dose enhancement [Verkhovtsev et al., 2014a, Verkhovtsev et al., 2014b].

So far simulations have been performed using protons as incident ions only. Up to now, any *in silico* study modeling the effects of other ions has not been published. These studies are necessary in order to explore the possible effects of the track structure for different particles. Not only the physical processes arising from the ion-NPs interaction but also the consequent radiation chemistry and biological pathways should be taken into account.

In summary, these studies have demonstrated the great potential of using NPs in combination with ion therapy to overcome the limitations of radiation therapy cancer treatments and improve tumor targeting. However, important questions remained to be answered such as the role of oxygen, a major parameter in tumor metabolism. Only one work has been published on the oxygen effect associated with the presence of NPs using photon radiation [Jain et al., 2014]. In this work, Jain and co-workers demonstrated a reduction of the radio-enhancement of NPs when the intracellular oxygen diminished. This effect was partially attributed to a decrease on the NPs internalization in hypoxic conditions.

3 Objectives of this work

The aim of this work was to study the influence of intracellular oxygen concentration on the effect of NPs combined with medical ion beams.

For this purpose, ultra-small (2-3 nm) gold and platinum NPs were tested in two human cancer cell lines (uterine and pancreatic cancer) *in vitro*. Three different oxygen concentrations were considered (0, 0.5 and 20% O₂) for the irradiation experiments. Carbon-ion radiation was run using the two current beam delivery modalities (passive scattering and pencil beam scanning). Additionally, helium-ion radiation experiments were performed for comparison.

This work includes: i) the distribution of NPs in the cell and the co-localization of NPs with cell organelles, ii) the quantification of NPs in the cells and iii) the biological impact of NPs combined with ion beam radiation in different oxygen conditions.

This project is included in a more ambitious program dedicated to the quantification and understanding of “Advanced Radiotherapy, Generated by Exploiting Nanoprocesses and Technologies”, project funded by the EU commission (FP7 European ITN Marie Curie Action Initial Training Network – ARGENT). The main objective of the multidisciplinary ARGENT ITN was to create a new generation of researchers and experts able to develop and propose to society new tools and concepts for the improvement of cancer therapy treatments [Bolsa Ferruz et al., 2017] (<http://itn-argent.eu/>).

During the last three years, ARGENT trained 13 Early Stage Researchers (ESR) of different disciplines: physicists and medical physicists, chemists, biologists and pharmacists. The consortium brought together researchers, medical doctors and small/medium-sized enterprises (SMEs). The research activities were divided into three main work topics:

- Nanodosimetry. Experimental and computational techniques were combined to disentangle the fundamental mechanisms present in radiation-induced damage in cells. The study of biomolecules, NPs and their mutual interaction when activated by ions was studied.
- Therapeutic Nanoagents. Chemists, pharmacists, biologists and medical physicists worked in the synthetization, characterization and testing of the properties and effects of the new generation of NPs. The internalization and localization of the

NPs within the cells were also included in the research. The combination of NPs with medical radiation (photons and ions) was studied from molecular to cellular scales, up to *in vivo*.

- Preclinical evaluation. The investigation of how nanoscale processes initiated by the interaction of radiation with living matter affect biological responses was used to establish the link between nanoscale interactions and clinical effects. Combining advanced experimental techniques and modeling tools, this workpackage intended to explore the clinical applicability of the new therapeutic protocols.

These activities had three main objectives: to go deeper in the understanding of physicochemical processes initiated by the interaction of radiation with biological matter in the perspective to predict and control the effects of new treatments, to develop new nanodrugs able to improve the application of the nanoscale phenomena for the best patient benefit and to discern how the effect of these nanoscale phenomena can potentially change clinical practice. New methods and tools were developed in this project with the sole purpose of improving patient outcomes.

Chapter II

Ion Beam Radiation: from elementary processes to the clinic

Chapter II is divided in two main sections. Section §1 includes the general principle of the interaction of charged particles with biological matter (section 1.1) and each of the three stages that it is composed of: physical, chemical and biological (section 1.2, 1.3 and 1.4). The clinical facilities where the experiments were performed and the type of beam delivery systems used are presented in section §2.

1 Interaction of charged particles with biological matter

1.1 General principles

Photons and charged particles (electrons and ions) are called ionizing radiation when they carry enough energy to ionize matter (i.e. extract electrons from the atoms and molecules of the medium). When biological matter is concerned, a specific cascade of events, involved in the 10^{-19} s to long time after irradiation, may be described as follows [Joiner and Van der Kogel, 2009] (figure II.1).

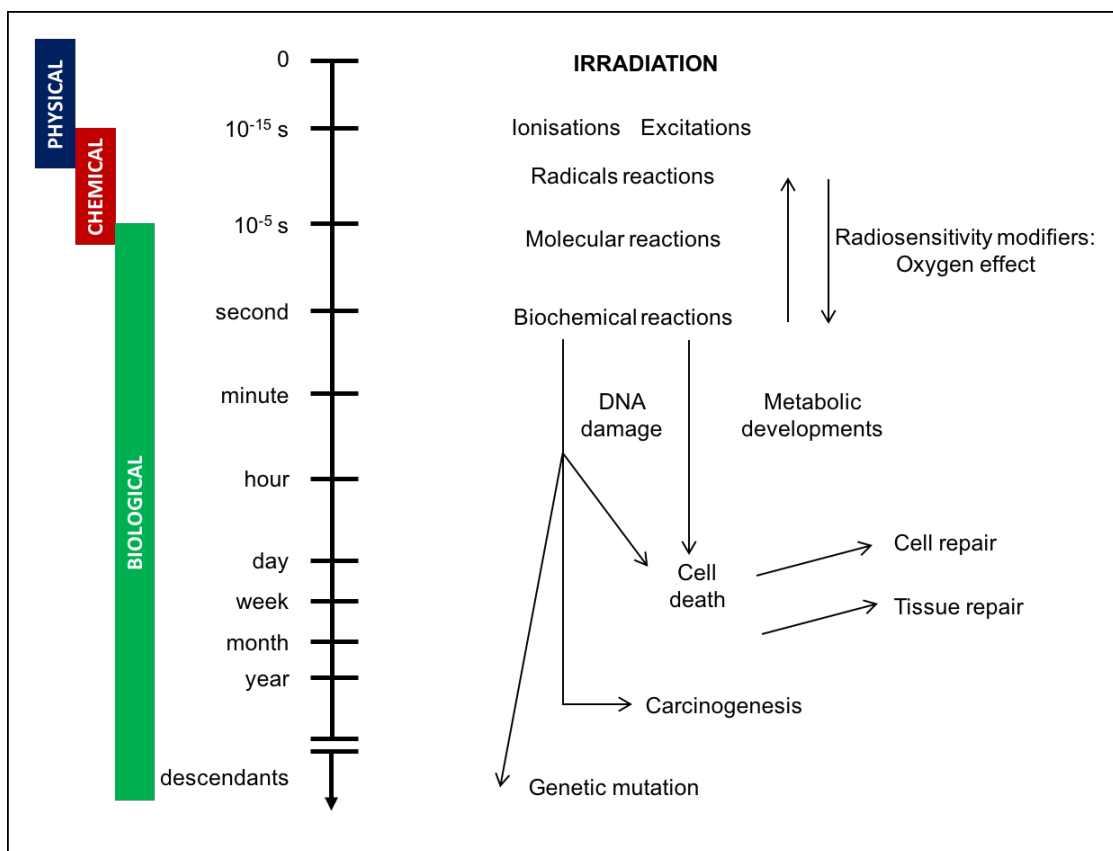


Figure II.1: Scheme of the interaction processes of radiation with a biological medium as a function of time. These processes are divided into three steps: physical, chemical and biological. Adapted from [Joiner and der Kogel, 2016].

The physical stage includes the interaction in between charged particles and the atoms of which the matter is composed. The primary process of ionization and excitation of

1. INTERACTION OF CHARGED PARTICLES WITH BIOLOGICAL MATTER

e^- (i.e. transfer of an electron to a more energetic state) takes place in the 10^{-18} – 10^{-14} s range. If the secondary electrons emitted by ionization processes are sufficiently energetic, they may ionize or excite other atoms and molecules of the medium, giving rise to a cascade of ionization events. When radiation interacts with the atoms of the DNA molecule, or some other cellular components critical to the survival of the cell, we refer to as a direct effects (figure II.2).

The interaction with water, principal component of the cells, with charged particles of energies higher than 13.6 eV leads to water radiolysis. The relaxation and fragmentation of excited water molecules (physical-chemistry stage, 10^{-14} and 10^{-12} s) lead to the formation of free radicals and water by-products. The resulting products may diffuse away from the radiation track and/or react with biological molecules (chemical stage, 10^{-12} and 10^{-6} s). The interactions of water by-products with biomolecules are called indirect effects (figure II.2). An important characteristic of the chemical phase is the competition between scavenging reactions (for example, sulfhydryl compounds that inactivate the free radicals), and fixation reaction by O_2 molecules that lead to stable chemical changes in biomolecules.

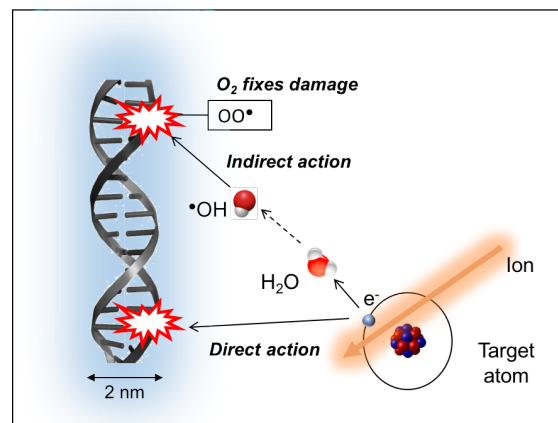


Figure II.2: Radiation damage on biomolecules (e.g. DNA) and oxygen fixation of damage. Adapted from [Twentyman, 1993]

The biological step includes all subsequent processes taking place at longer times after irradiation (from 10^{-6} s after irradiation and beyond). DNA and other biomolecules damage can be successfully repaired. However, complex lesions may fail to repair and alter the biological function due to metabolic response such as mutation and/or cell

death. Sometimes, irradiated cells may undergo a number of mitotic divisions before dying (delayed cell death). The aim of radiation therapies is to kill cells and eradicate the growth of cancer tissue. Secondary effects of cell-killing may be compensated by cell proliferation repairing the tissue. At later times after irradiation of health tissue, late reactions, such as blood vessel damage, appears. An even later manifestation of radiation damage is the appearance of second tumors (carcinogenesis). The observable effects of ionizing radiation extend up to many years after exposure and can be visible in descendants as genetic mutations.

1.2 Physical stage

Heavy charged particles (protons or heavier ions such as carbon, helium or oxygen) passing through matter slow down by losing their kinetic energy mainly through electromagnetic interactions with atoms of the medium. As a main advantage compared to high energy photons [Attix, 2004], ions stop within matter at a known depth with a maximum energy deposition in the Bragg peak [Bragg and Kleeman, 1905] (figure II.3). This effect is described by the stopping power as presented in section 1.2.1. The primary interaction between ions and matter leads to the production of secondary electrons that can, in turn, interact with matter. The interaction of these electrons with target atoms is presented in section 1.2.2. The special case of charged particles (incident ions or secondary electrons) interacting with a high-Z atoms (i.e. metallic NPs) is discussed in section 1.2.3. The target atoms and molecules, after being excited by charged particles, eventually come back to the ground state through relaxation processes which are described in section 1.2.4.

1.2.1 Stopping power

a) Mean energy loss

The stopping power is defined as the average loss of kinetic energy, E , per path length, x , resulting from Coulomb interactions with electrons and nuclei from the target atoms [Seltzer et al., 2011a].

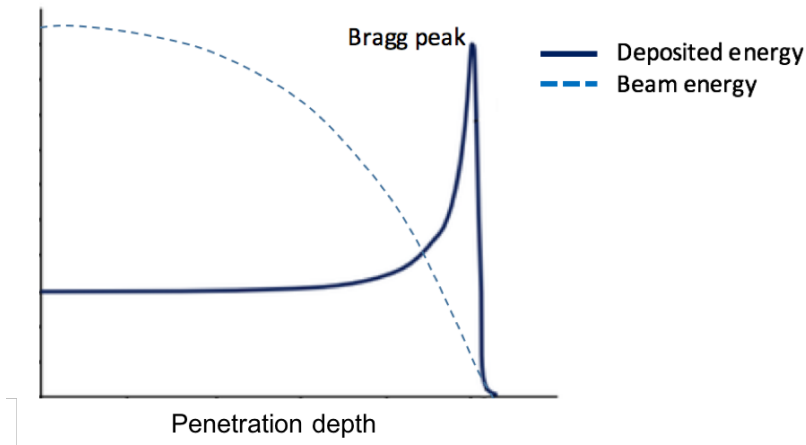


Figure II.3: Beam energy (dashed line) and deposited energy (solid line) versus penetration depth in the absence of energy loss fluctuations. Adapted from ICRU REPORT 73 [Bimbot et al., 2005].

The stopping power can be expressed as a sum of independent components by:

$$S = -\frac{dE}{dx} = S_{el} + S_{nuc} + S_{rad} \quad (\text{II.1})$$

The electronic stopping power (or collision stopping power) (S_{el}) due to interactions with atomic electrons is the biggest contribution to the energy loss. On the contrary, the nuclear stopping power (S_{nuc}) resulting from elastic interactions with the atomic nuclei has only a minor contribution. It becomes dominant only for very low energies of the order of 10 keV/u (last few μm of the track) [Schardt et al., 2010]. At therapeutic energies, radiative stopping power (S_{rad}) due to emission of bremsstrahlung in the electric fields of atomic nuclei or atomic electrons is negligible. The stopping power as a function of the ion specific energy (incident energy per nucleon, MeV/u) is shown in figure II.4 for protons and for carbon-ions passing through water.

b) Electronic stopping power

The electronic stopping power is due to the interactions with the atomic electrons of the medium. Depending on the distance between the primary ion and the target electron, the target atom can be either excited by launching the electron to a higher

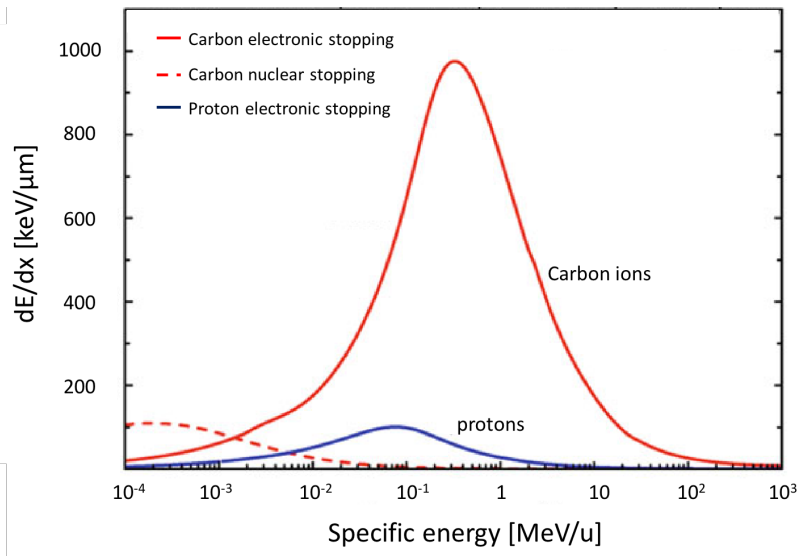


Figure II.4: Stopping power of protons (blue) and carbon-ions in water (red). The red solid line indicates the contribution of electronic stopping power and the dashed line the nuclear stopping power for carbon ions. Adapted from [Schardt et al., 2010]

orbital or be ionized by ejecting the electron. In the latest case, a positively charged site is created in the atomic target. A small fraction of these secondary electrons, known as δ -electrons, has large energies compared to the ionization potential. They are emitted mainly in the forward direction, and those with comparatively lower energies have larger angles and shorter tracks.

The Bethe-Bloch equation describes the mass electronic stopping power of charged particles (ICRU REPORT 49 [Berger et al., 1993]):

$$\frac{S_{col}}{\rho} = -\frac{1}{\rho} \left(\frac{dE}{dx} \right)_{el} = \frac{4\pi z^2 e^4}{mc^2 \beta^2} \frac{1}{u} \frac{Z}{A} L(\beta) \quad (\text{II.2})$$

where z is the atomic number of the incident ion, βc is the speed of the ion, c is the speed of light, e is the electron charge, mc^2 is the electron rest mass energy, u is the atomic mass unit and Z and A are the atomic number and relative atomic mass of the target atom.

The quantity L is called the stopping number. The factor preceding L take into account the gross features of the energy-loss process, whereas L , accounts for fine corrections. L

can be expressed as the sum of three terms:

$$L = L_0(\beta) + zL_1(\beta) + z^2L_2(\beta) \quad (\text{II.3})$$

The first term is given by:

$$L_0(\beta) = \frac{1}{2} \ln \left(\frac{2mc^2\beta^2 W_m}{1 - \beta^2} - \beta^2 - \ln(I) - \frac{C}{Z} - \frac{\delta}{2} \right) \quad (\text{II.4})$$

where $\ln(I)$ is the logarithm of the mean excitation energy of the medium. It encloses most of the dependence on the target material. The $\frac{C}{Z}$ is the shell correction term and accounts for the internal structure of the target atoms, playing a role only for low energies, in the order of a few MeV/u. The density-effect correction term is expressed by $\delta/2$. It takes into account the polarization effects in solid media, and is only important for ultra-relativistic energies, above 1 GeV/u. W_m is the largest possible energy loss in a single collision with a free electron.

The Barkas first-order correction ($zL_1(\beta)$) models the difference between negatively and positively charged projectiles. Finally, the Bloch second-order correction ($z^2L_2(\beta)$) models ion-electron interactions with high impact parameter.

Due to the major dependence of the stopping power with $1/\beta^2$ ($L(\beta)$ varies slowly with β^2), the stopping power increases when the particle velocity decreases. This explains the maximum of energy loss at the end of the track when the particle velocity is close to zero (Bragg peak). The maximum energy-loss rate determines the position of the Bragg peak. It is reached at a ion velocity of $v_p \approx z^{\frac{2}{3}}v_B$, where $v_B = e^2/\hbar$ is the Bohr velocity. For proton and carbon-ions, it occurs at a specific energy of about 25 keV and 350 keV/u, respectively [Scharadt, 2016].

At high velocities, the incident ion charge is equal to the atomic charge number (z). At lower velocities (for light ions below 10 MeV/u), the mean charge state decrease due to the interplay of ionization and electron capture processes and z has to be replaced by the empirical Barkas-formula that gives the effective atomic charge [Bichsel, 1990].

An extensive analysis of the physical processes which influence the stopping power of charged hadrons in matter can be consulted in the ICRU Reports 49 and 73 [Berger et al., 1993, Bimbot et al., 2005].

c) Linear Energy Transfer (LET) and ion track structure

The linear energy transfer (or restricted linear electronic stopping power) (L_{Δ} , LET) of a material for charged particles of a given type and energy is the mean energy loss by the charged particles due to electronic interactions (dE_{Δ}) per unit track length (dx) minus the energy carried away by energetic secondary electrons having initial kinetic energies greater than Δ (ICRU REPORT 85, [Seltzer et al., 2011b]).

$$L_{\Delta} = \frac{dE_{\Delta}}{dx} \quad (\text{II.5})$$

It can also be expressed by:

$$L_{\Delta} = S_{el} - \frac{dE_{ke,\Delta}}{dx} \quad (\text{II.6})$$

Where S_{el} is the electronic stopping power (equation (II.2)) and $dE_{ke,\Delta}$ is the mean sum of the kinetic energies greater than Δ . If no energy cutoff is imposed the unrestricted linear energy transfer, L_{∞} , is equal to S_{el} . The LET is often expressed in keV/ μm .

The LET is approximately proportional to z^2/v^2 , with z and v being the ion charge and speed, respectively. As ions lose energy, their speeds decrease, which results in an increased ionizing density, more specifically in the Bragg peak. Moreover, as heavier ions such as carbon-ions have a larger z than protons, they have a higher LET. The ion track of a proton and a carbon-ion in water are represented in figure II.5.

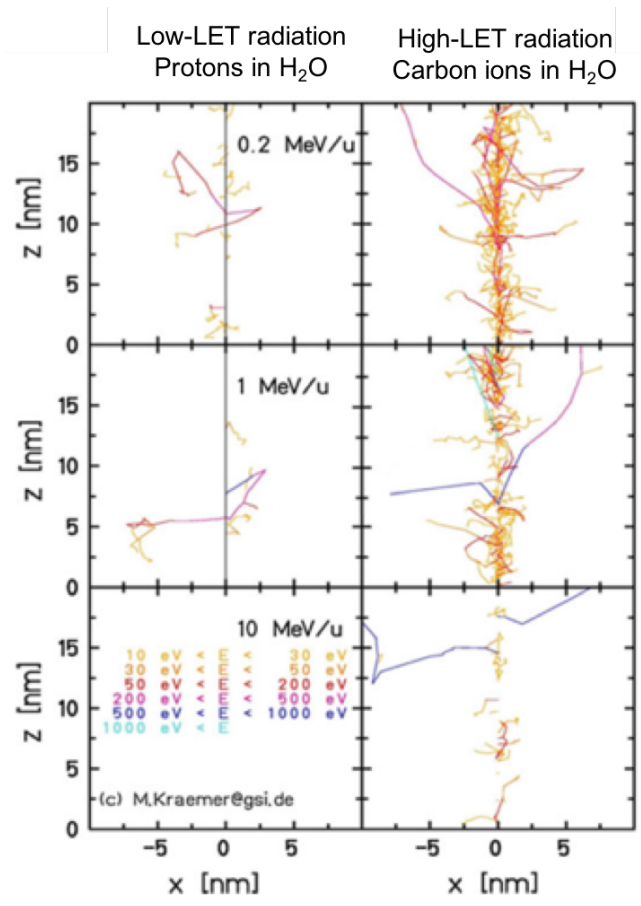


Figure II.5: Monte-Carlo simulations showing individual tracks of secondary electrons produced by fast protons and carbon-ions penetrating tissue. The particles enter at $x = 0$ and move along the z -axis. Adapted from [Krämer, 1995].

We can observe in figure II.5, that carbon-ions produce a larger number of secondary electrons with higher energies than protons at the same energy per nucleon. A more dense ionization track is formed by carbon-ions. In addition, these simulations shows higher ionization as the energy of the ion decreases with a maximum at the Bragg peak (few hundred $\text{keV}/\mu\text{m}$).

The dose-average LET (LET_d) value is commonly used to characterize a mixed radiation field with a LET distribution (i.e. radiation field composed by particles of different energies) [Guan et al., 2015]. The weighting factor for the LET_d calculation is the absorbed dose, which is defined as the mean energy absorbed per unit mass measured in Gray ($1 \text{ Gy} = 1 \text{ Joule} / 1 \text{ kg}$).

The dose-averaged LET (LET_d) is given by:

$$LET_d(z) = \frac{\int_0^\infty S_{el}(E) \times D(E, z) dE}{\int_0^\infty D(E, z) dE} \quad (\text{II.7})$$

where $S_{el}(E)$ is the electronic stopping power of primary charged particles with kinetic energy E and $D(E, z)$ is the absorbed dose contributed by primary charged particles with kinetic energy E at location z .

1.2.2 Interaction of secondary electrons with matter

Secondary electrons lose their energy primarily through Coulomb interactions with bound target electrons through elastic or inelastic scattering. In the first case, the electrons do not lose their energy but they are strongly deflected. Through inelastic collisions, the electrons transfers part of its energy to a target electron.

Electrons of high energy (MeV) can be deflected by an atomic nucleus. This leads to a loss of kinetic energy, which is instantaneously released through the emission of an X-ray photon (bremsstrahlung). The ratio of energy loss by radiation relative to that by ionization and excitation is approximately $ZE/800$, where Z is the atomic number of the target nucleus and E is the electron energy in MeV. A 10-MeV electron slowing in water ($Z = 8$) would lose less than 10% of the energy loss per unit path length via radiation [Mozumder and Hatano, 2004]. Secondary electrons emitted by medical ion beams have energies below MeV. Thus, the probability of inducing bremsstrahlung radiation is low.

For electrons with energies greater than 1 keV, interactions in water (low-Z medium) such as simple ionization and electronic excitation represent the most likely mechanism of the electron energy loss. Ionization occurs in about 90% of the interactions [Mozumder and Hatano, 2004]. Secondary electrons ionize other atoms and molecules of the medium until its energy drops below a threshold where further ionization is no longer possible.

The dissociative electron attachment (DEA) takes place for electrons of energies below 25 eV, which have energies of the same order than the electrons of the target molecules. These electrons can attach to the target molecules and form intermediate species in

negative excited states $(AB^-)^*$. The de-excitation of these excited species may lead to the auto-detachment of the electron with excitation of the molecule (i.e. $(AB)^* + e^-$) or the dissociative attachment with fragmentation of the molecules (i.e. $A + B^-$).

1.2.3 Interaction of charged particles with metallic NPs

The explanation of the radio-enhancement properties of NPs under ion beam radiation on the fundamental level is not fully understood. The most important mechanism is associated with the emission of secondary electrons induced by either the primary beam or the secondary electrons produced along the track. The possible mechanisms in the amplification of ion beam by NPs are represented schematically in figure II.6.

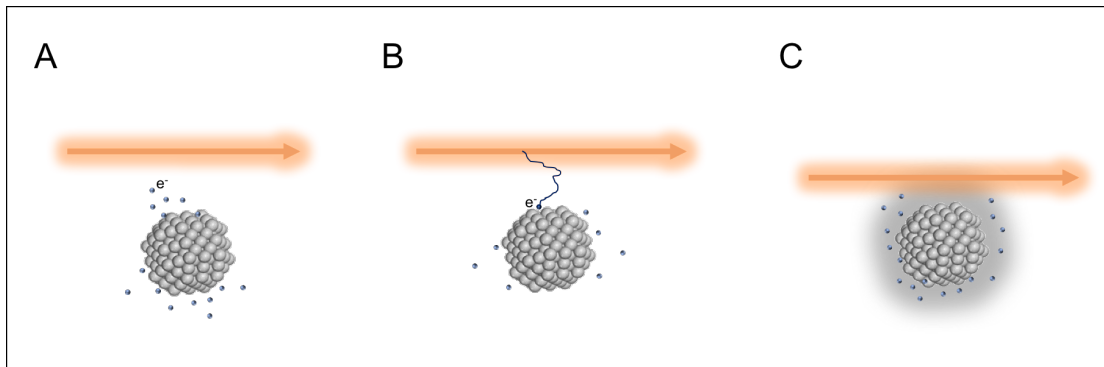


Figure II.6: Scheme of possible mechanisms involved in the amplification of ion beam by NPs. (A) Incident ion activating a NPs due to strong coulomb interaction. (B) Interaction of secondary electrons produced in the ion track with NPs. (C) Plasmon excitation.

Charged particles (incident ions or secondary electrons) interact with a NPs comprised of high-Z atoms via Coulomb interactions with a cross section that depends mainly on the kinetic energy and charge of the incident particle and on the impact parameter (radial distance from the particle track to the target). For high-Z targets, nuclear stopping is negligible and fast ions or electrons, typically with energies greater than 1 MeV/u, lose energy mainly via inelastic collisions with the atomic electrons. The electronic stopping power is mostly due to interactions with outer valence shell electrons until the incident ion or electron energy has sufficiently slowed to energies comparable to the mean orbital energy of inner shell (e.g. L, K) electrons [Hatano et al., 2011]. Hence, the early excitation/ionization stage of NPs is promptly followed by the de-excitation of the system via rearrangement of electronic states resulting in fluorescent photon emission and Auger

electron emission (figure II.6 A and B). This de-excitation processes are described more extensively in section 1.2.4. The number of electrons emitted depends on the ion charge and velocity, the composition, size and molecular coating as well as the chemical environment in which the collision takes place. The secondary electrons generated by these events can continue to excite and ionize surrounding biomolecules and neighboring NPs.

When an external electrical field produced by charged particles (electrons or ions) interacts with an assembly of free electrons, like in the conduction band of metals, the transfer of energy can induce collective density oscillations inside the electron plasma called plasmons. The energy quantum of this oscillation is the volume plasmon which is of the order of some eV. The de-excitation of the surface and volume plasmons leads to the emission of a photon or an electron (figure II.6C).

1.2.4 Electronic processes of relaxation

After interaction with charged particles and secondary electrons, the target atoms are left in a highly-excited state. In particular, when inner shells are ionized, the electrons reorganize to bring the system back to its fundamental state. The excess energy associated with this phenomenon can be released through two possible processes: Auger de-excitation (non- radiative process) or fluorescence (radiative process). These two mechanisms are described below.

Auger de-excitation

After ionization of an inner shell (e.g. K or L shell), the atom de-excite by transfer of an electron from the upper shell (e.g. L₁ to K shell) with a release of energy to another electron (e.g. L₂₃ electron, see figure II.7). The emitted electron is called Auger electron. Following the previous example, the kinetic energy (E_A) of the emitted Auger electron is expressed by the following equation:

$$E_A = E_e - E_{b(K)} - E_{b(L_{23})} \quad (\text{II.8})$$

Where E_e is the energy of the incident electron, $E_{b(k)}$, the binding energy of the emitted electron from the K-shell orbital and $E_{b(L_{23})}$, the binding energy of the Auger electron.

After this electronic relaxation process, the target atom is left with two positive charges. This mode of de-excitation continues until the rearrangement of the entire electronic cloud. Auger de-excitation is responsible for the amplification of the electronic emission. Following the Auger cascade, the atoms remain strongly positively charged. They may capture electrons from surrounding water molecules and induce strong perturbation in the close environment [Feldman and Mayer, 1986].

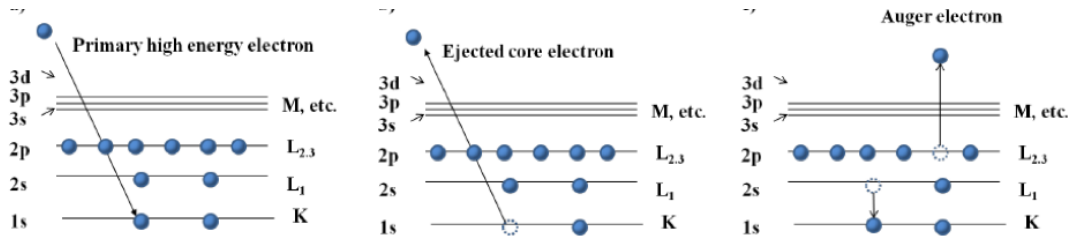


Figure II.7: Electron relaxation via Auger de-excitation process in the case of a K L₁ L_{2,3} transition.

Radiative process

When a vacancy in the inner shell is formed, the electrons re-organize with release of the excess energy in the emission of an X-ray photon (figure II.8). If the K-shell of the atom is ionized, the energy of the emitted X-ray photon (E_x) is equal to

$$E_x = E_{b(k)} - E_{b(L_{23})} \quad (\text{II.9})$$

Where $E_{b(k)}$ is the binding energy of the emitted electron from the K-shell orbital and $E_{b(L_{23})}$, the binding energy of the re-located electron from an upper shell.

The de-excitation of the ionized atom results in a series of electronic cascades of reorganization, accompanied by emissions of X photons and Auger electrons. The competition between the two de-excitation mechanisms is characterized by the fluorescence yield ω defined as the number of photons X divided by the number of electron holes:

$$\omega_K = \frac{\text{Number of photons } X_K}{\text{Number of holes in } K} \quad (\text{II.10})$$

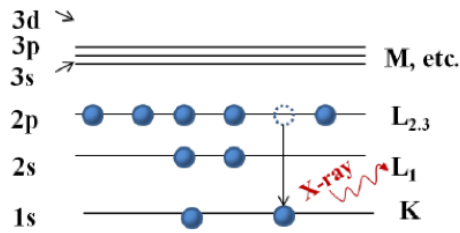


Figure II.8: Electron relaxation via fluorescence process in the case of a K L₂₃ transition.

The fluorescence yield as a function of the atomic number of the target for K- and L-shell (average) vacancies is shown in figure II.9.

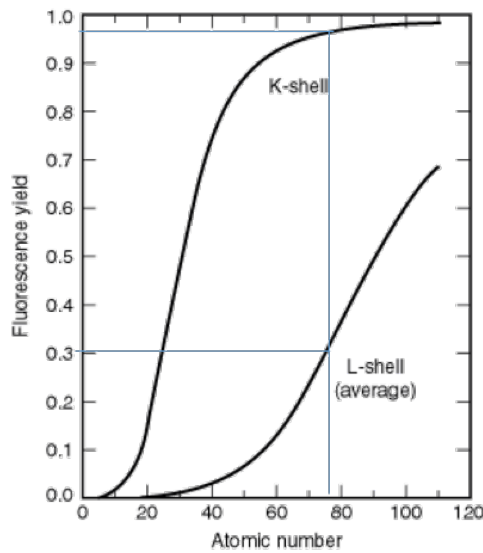


Figure II.9: Fluorescence field as a function of the atomic number. Data are based on [Krause, 1979].

The fluorescence yield increases with the atomic number of the target. The Auger process is dominant in the light elements that compose the biological system (C, O and N). In the case of K-shell vacancies, the fluorescence relaxation predominates for heavy atoms (Au, Pt, Gd).

The fluorescence yield behavior is strongly different for the L-shell ionization. For metallic atoms, it remains below 50% and the relaxation via Auger de-excitation is thus dominant. In the case of Pt ($Z = 78$), there is around 97% of fluorescence after K-shell ionization and around 70% of Auger electron emission after L-shell ionization.

Electron capture by positively charged sites

After relaxation processes by Auger cascades, target atoms (NPs) are highly positively charged. The atoms may neutralize via capture of electrons from surrounding molecules (water for instance) [Kočiček et al., 2013] as show in figure II.10.

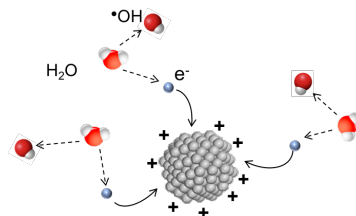


Figure II.10: Electron capture on a positively charged nanoparticle.

1.3 Radiation chemistry

1.3.1 Water radiolysis

The transfer of energy from the incident ion to biological systems is responsible for the ionization of water molecules (water radiolysis), and cellular constituent (nuclear acids, lipids, proteins...).

As an example, a dose of 10 Gy, which kills almost all mammalian cells correspond to 2×10^6 ionizations per cell. Since a cell contains about 10^{13} water molecules and 10^8 larger molecules, the proportion of molecules which suffer an ionization is very small. However, it is enough to result in the production of significant lesions [Tubiana M., Dutreix J., 1990].

The phenomenon of water radiolysis leads to the production of radicals, which refers to an atom or molecule that contains an unpaired electron. They can be neutral or charged and are highly reactive. A scheme of the water radiolysis is found in figure II.11.

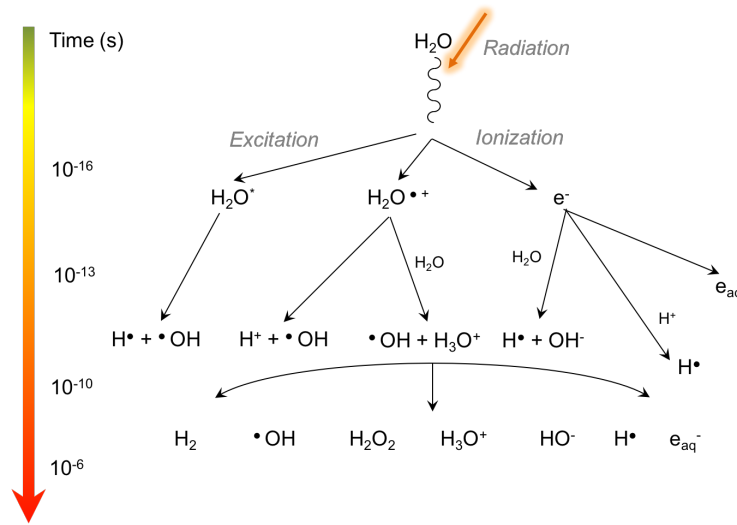
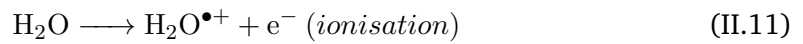
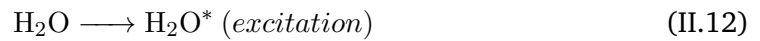


Figure II.11: Scheme of the species produced by water radiolysis. Adapted from [Lousada et al., 2016]

Direct ionization of water produces a radical ion and a free electron.



The transfer of energy can also produce water in an excited state.



The time scale for the formation of these species is on the order of 10^{-16} s .

The radical ion of water can dissociate to produce a hydroxyl radical and a hydrogen ion:



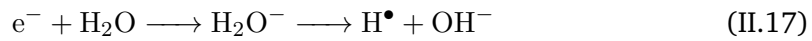
Or it can undergo the ion-molecule reaction:



The excited water molecules dissipates the excess of energy by bond breakage to produce hydroxyl and hydrogen radicals:



The free electron can react with H^+ or water molecules to form hydrogen radicals and hydroxide ions:

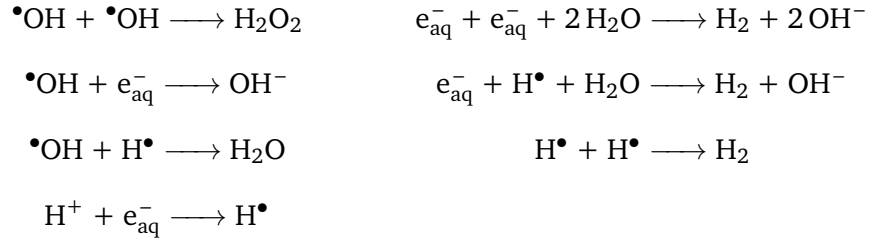


The electrons detached by ionization have at their origin a kinetic energy which is sufficient to travel a significant distance making recombination unlikely (e.g. for 10 eV the distance is about 15 nm, corresponding to 70 water molecules). They progressively lose their energy by multiple interactions with their surrounding environment. After electrons are sufficiently slowed down, if they have not reacted yet with water or hydrogen ions, they are captured by water through dipolar interactions, becoming solvated (also called hydrated or aqueous electron). This new entity is more stable than the free electron [Alpen, 1997].



The principal primary radicals are the hydrated electron, e_{aq}^- , which is a powerful reductant (compound that donates an electron to another chemical specie) and the hydroxyl radical, $\bullet\text{OH}$, which is a powerful oxidant (compound that removes one or more electrons from another chemical specie). The hydrogen atom, H^\bullet , is not an important species in neutral or alkaline solution, but it becomes the major reductant in acidic solution [Maurizot, 2008].

After 10^{-12}s , the radicals $\bullet\text{OH}$, H^\bullet and e_{aq}^- begin to migrate randomly. As this diffusion proceeds, individual pairs may come close enough together to react with each other (recombination). A variety of reactions are possible in the track of the charged particle [Tubiana M., Dutreix J., 1990].



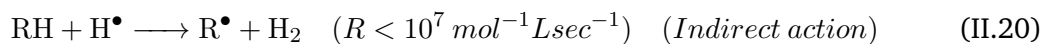
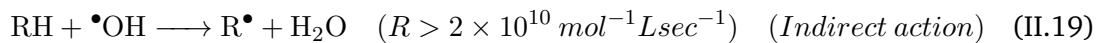
In the presence of oxygen (oxic conditions), aqueous electrons may attach to O_2 to form superoxide ($\text{O}_2^{\bullet-}$) with a rate constant of $R = 1.9 \times 10^{10} \text{ mol}^{-1} \text{ Lsec}^{-1}$. H^\bullet may react with O_2 to produce HO_2^\bullet ($R = 1.2 \times 10^{10} \text{ mol}^{-1} \text{ Lsec}^{-1}$). Reactive chemical species containing oxygen are known as Reactive Oxygen Species (ROS).

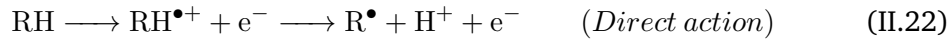
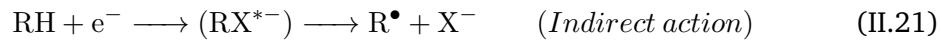
The chemical development of the track is over at 10^{-6} s , when all the reactive species have diffused sufficiently far that further reactions are unlikely.

The proportions and spatial distribution of the radicals and molecules after the passage of the ionizing particle vary according to the nature of the incident beam and the composition of the environment (presence of oxygen, radical scavengers or metallic NPs).

1.3.2 Reaction of water by-products with biomolecules

Water radicals can migrate and react with organic molecules dissolved in the medium. They can induce oxidation and reduction reactions on biomolecules such as DNA, proteins, lipids, hydrogen-donators (i.e. NADH, NADPH) and other cell constituents, causing cell damage [Tubiana M., Dutreix J., 1990]. The effects of interaction of water radicals produced by ionizing radiation in the solvent with biomolecules are called indirect effects. It is admitted that the most damaging radical is $\bullet\text{OH}$. Radicals of organic molecules can also be produced by direct action [Chapman et al., 1973]. Equations II.19 to II.22 show the production of organic molecules radicals due to the interaction of water by-products [Alpen, 1997].





$\bullet\text{OH}$ is highly reactive and in a cellular environment their diffusion length is very short (few nm). DNA has always been considered as the main target responsible for cell-killing. However, it is demonstrated that damage of cytoplasmic molecules may strongly perturb cell metabolism [Houée-Lévin et al., 2015].

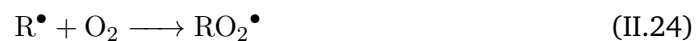
1.3.3 Effect of molecular oxygen on radiation damage

The presence of oxygen has a strong influence on the effectiveness of radiation to produce damage. It alters the intracellular redox state of mammalian cells. The "oxygen fixation hypothesis" stands that biomolecule radicals may react either with radical-reducing species, resulting in "chemical repair", or with radical oxidizing species, resulting in "fixation" of radical damage to a potentially lethal form [Chapman et al., 1973].

After the production of organic radicals (equations II.19 to II.22), sulfhydryl compound may interact with biomolecules radicals and restore them. One of the most important of this compounds is reduced glutathione, which is abundantly present in most cells [Alpen, 1997]. The reaction is called chemical repair:



However a competing reaction may take place with oxygen that fixes the state of the radical in the biomolecule and presumably leads to chemically irreparable damage. This reaction is central in the sensitizing effect of oxygen:



Oxygen molecules may cause the damage fixation of important molecules such as DNA. The product, a peroxidated radical, is more stable and therefore more long lived than

the original DNA radical. It is more likely to proceed to irreversible damage or misrepair of the DNA molecule. $O_2^{\bullet-}$ does not react directly with biomolecules but with radical derivatives.

1.3.4 High-LET ion radiolysis of water

The yield of water radiolysis by-products depends on the radiation quality and thus the LET of incident ions. The g values (number of product formed per 100 eV of energy absorbed) of the main products when using with high-LET radiation are reviewed here. For more details see [Yamashita et al., 2008, Wishart and Rao, 2010]. Figure II.12A shows the LET (eV/nm = keV/ μ m) versus the specific energy of six different ions. The g values of e_{aq}^- , \bullet OH and H_2O_2 for these ions are reported in figure II.12 B, C and D.

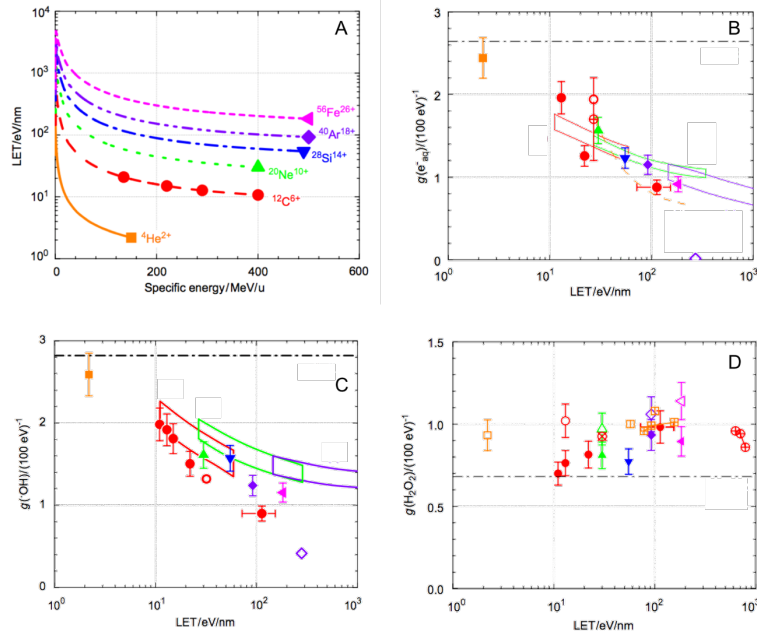


Figure II.12: (A) LET values as a function of ion energy per nucleon for six ions [Ziegler, 1998]. (B), (C) and (D): Primary g values of hydrated electron, hydroxyl radical and hydrogen peroxide respectively as a function of LET. In panel (D), solid and open data points correspond to irradiation under anoxic conditions and oxic conditions respectively. Adapted from [Yamashita et al., 2008].

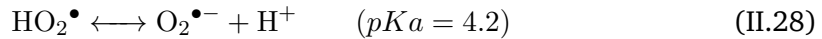
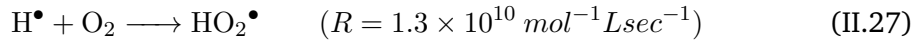
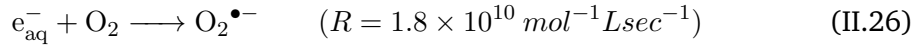
The $g(e_{aq}^-)$ value for carbon ion radiolysis goes down from about 2 to less than 1 $(100\text{eV})^{-1}$ when the LET values increase from 10 to 100 eV/nm. In comparison with

the data of neon or silicon ions having LET value comparable to one of the carbon ion beams, confirmed that the $g(e_{aq}^-)$ value for lighter ion is smaller than that of heavier ion. Similarly to e_{aq}^- , $\bullet\text{OH}$ yield decreases with increasing LET, and the $\bullet\text{OH}$ yield obtained with helium ion beams (LET = 20 keV/ μm) is almost equivalent to that with low LET radiation. The $g(\bullet\text{OH})$ for carbon ion radiolysis decreases also with the increase of LET. However, similarly to e_{aq}^- , the primary g values of $\bullet\text{OH}$ for heavier ion is higher than those for lighter ions with comparable LET. The enhancement of $\bullet\text{OH}$ destruction in the intra-track reactions is more sensitive to the increase of LET than e_{aq}^- .

H_2O_2 is much more stable than other water decomposition products though it can be destroyed by e_{aq}^- having escaped from the intra-track reactions:



The increase of the $g(\text{H}_2\text{O}_2)$ with increasing LET is not clear due to the small differences. However a clear tendency is observable for the data series of carbon ion beams. The presence of O_2 enhances the H_2O_2 production. This could be explained by two reasons: one is the increase of H_2O_2 production via $\text{O}_2^{\bullet-}$,



and the other is the decrease of H_2O_2 destruction by e_{aq}^- in long-time region represented in equations II.25. Yamashita and co-workers confirmed that lighter ion gives smaller radical yields ($\bullet\text{OH}$) and larger molecular yields H_2O_2 .

1.4 Biological impact of radiation in living cells

1.4.1 Linear-quadratic model

The linear-quadratic (LQ) model describes the cellular response to ionizing radiation. The surviving fraction (SF) of cells after radiation exposure decreases exponentially with the radiation dose. It can be fitted by a second-order polynomial with a zero constant term to ensure that $SF = 1$ at zero dose (figure II.13). The LQ model is mathematically expressed by the following equation:

$$SF = \exp(-\alpha D - \beta D^2) \quad (\text{II.30})$$

The linear component results from the contribution of lesions which are directly lethal for the cell, whereas the quadratic component arises from the contribution of additive sub-lethal lesions. The survival curve of heavy ion radiation (high LET) is almost an exponential curve with mainly linear component. The lethality is essentially due to direct lethal damage. In the case of photon or light ions radiation (low LET), the curve is strongly bent and the cell-killing undergoes mainly due to cumulative sub-lethal damage.

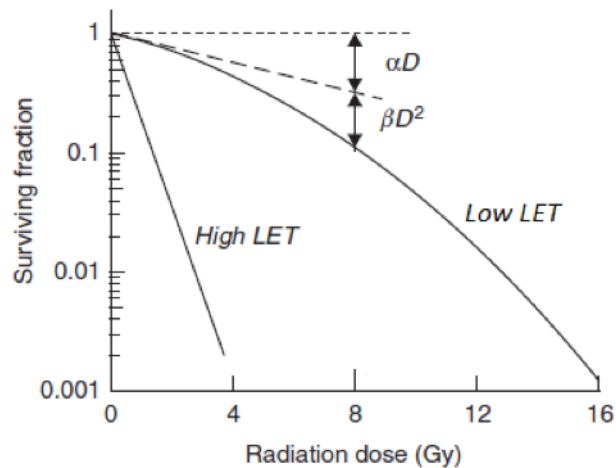


Figure II.13: Linear-quadratic model for high and low LET. Adapted from [Joiner and Van der Kogel, 2009].

The measurement of the SF allows to evaluate and to compare the radio-enhancement

effect due to the addition of NPs for the different experimental conditions at cellular level.

1.4.2 Relative Biological Effectiveness (RBE)

The concept of Relative Biological Effectiveness (RBE) was introduced to account for the increased efficiency of ions vis-à-vis photons. The differences in effectiveness are related to differences in energy deposition at the level of the particle tracks and subcellular structures. The RBE is defined as the ratio of the absorbed dose of a reference beam of photons to the absorbed dose of any other radiation, notably, high LET radiation, to produce the same biological effect (equation (II.31))

$$RBE = \frac{D_{photons}^{SF_0}}{D_{ions}^{SF_0}} \quad (II.31)$$

RBE cannot be uniquely defined for a given radiation. The RBE of a given type of radiation will vary with the particle type and energy, dose, dose per fraction, degree of oxygenation, cell or tissue type, biological end point, etc. [IAEA, 2008] In the case of ion radiation, the situation is particularly complex and the RBE is a strong function of position within the treatment beam (figure II.14).

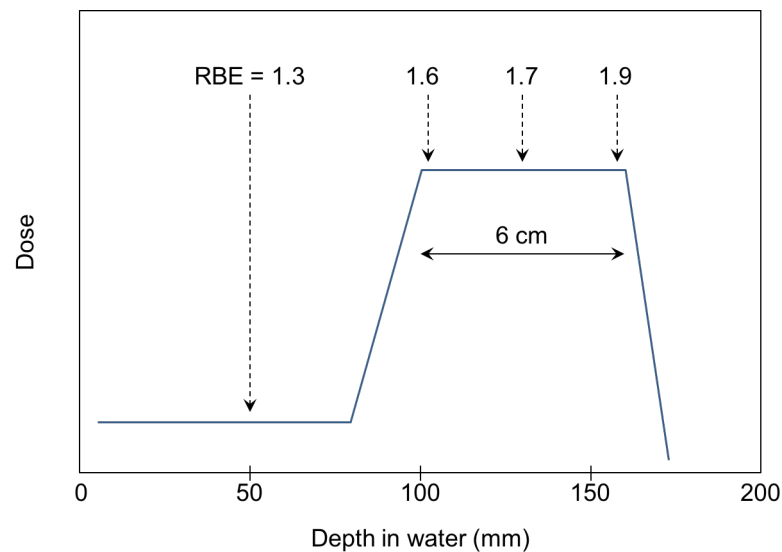


Figure II.14: RBE for carbon-ions ($E = 290\text{MeV/u}$, SOBP width = 6cm) relative to cobalt-60 gamma rays as a function of depth in the water phantom. The depths investigated are: "initial plateau" ($\text{LET}_d = 13.7 \text{ keV}/\mu\text{m}$), beginning, middle and end of the 6-cm SOBP ($\text{LET}_d = 40.9, 49.4$ and $70.7 \text{ keV}/\mu\text{m}$, respectively). Adapted from [Gueulette et al., 2004].

The RBE values as a function of the LET for eight different cell lines exposed to monoenergetic and extended Bragg peak radiation are shown in figure II.15.

RBE increases with LET but appears to reach a maximum at LET values of approximately 100–200 $\text{keV}/\mu\text{m}$ before declining in the 'overkilling' region where the fluencies required for doses of a few Gy become very small and a certain fraction of the cells may not be hit at all.

Figure II.15 shows that even at the same value of LET, RBE is a function of ion type. This is a result of differences in the fine structure of energy deposition for different ion types even at the same LET. It indicates that LET, while often adequate, is not a perfect predictor of RBE. For carbon ions, the maximum of the RBE curve almost coincides with the maximum of the Bragg curve leading to a maximal effect for the tumor, for particles heavier than carbon the RBE maximum shifts to proximal part of the Bragg peak.

Some findings on the RBE dependence can be assumed to apply to all tumor or normal tissues in the extended Bragg Peak region of an ion beam: RBE increases with LET, decreases with increasing particle energy, increases with decreasing fraction size (dose/fraction) and is higher for some late versus early responding tissues.

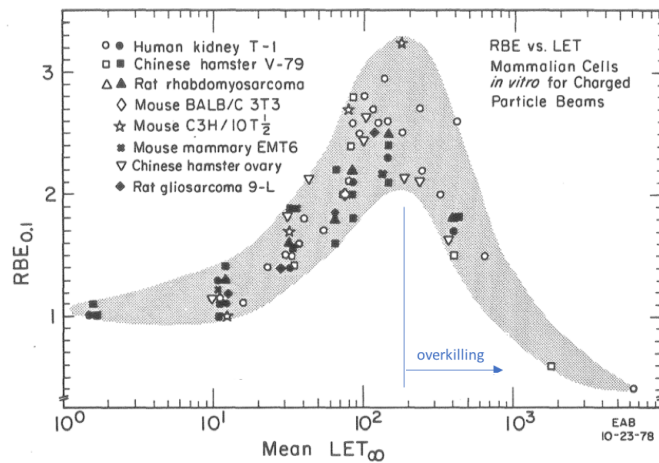


Figure II.15: RBE versus mean LET for monoenergetic and extended Bragg peak data using mammalian cell survival data measured *in vitro*. The cells were irradiated under oxic conditions and the end point was 10% cell survival. The results are compiled from eight different cell systems. Adapted from [Blakely et al., 1983].

If radiation oncologists benefit from the vast experience with photon radiation and the knowledge gained with respect to doses required for tumor cure and the tolerance of normal tissues, then it becomes mandatory to have the ability to convert doses of photon radiation into equally effective doses of other radiations, namely, ions — hence, the need for the concept of RBE.

1.4.3 Hypoxic tumors and Oxygen Enhancement Ratio (OER)

The presence of hypoxia (regions of low levels of oxygen) in human tumors was postulated by Thomlinson and Gray 50 years ago [Thomlinson and Gray, 1955]. Hypoxia arises in tumors through the uncontrolled proliferation of cancer cells in the absence of an efficient vascular bed. Due to the rapid proliferation of cancer cells, the tumor quickly exhausts the nutrient and oxygen supply from the normal vasculature. Typically cells residing at a distance greater than 70 μm from functional blood vessels receive inadequate amounts of oxygen (figure II.16) [Vaupel et al., 1989]. Oxygen concentrations in human tumors are highly heterogeneous with many regions at very low levels (less than 5 mmHg partial pressure of oxygen (pO_2) which corresponds to approximately 0.7% O_2 in the gas phase or 7 μM in solution), with median values much lower than the normal tissues from which the tumors arose (30 - 50 mmHg) [Brown and Wilson,

2004]. Identifying hypoxic cells in human tumors by the help of new imaging is crucial for the development of tumor-selective therapies [Sun et al., 2011].

Hypoxia in tumors is associated with a poor clinical outcome as compared to patients with tumors lacking hypoxia [Höckel et al., 1991, Brown and Giaccia, 1998]. The cells in these hypoxic regions are resistant to both radiotherapy and chemotherapy. In addition, it has also been demonstrated that hypoxia in tumors tends to select for a more malignant phenotype. By enhancing metastasis, hypoxia can compromise curability of tumors by surgery.

The hypoxic cell radioresistance is a result of lack of oxygen in the radiochemical process by which ionizing radiation is known to interact with cells (section 1.3.3). The Oxygen Enhancement Ratio (OER) is commonly used to quantify the oxygen effect.

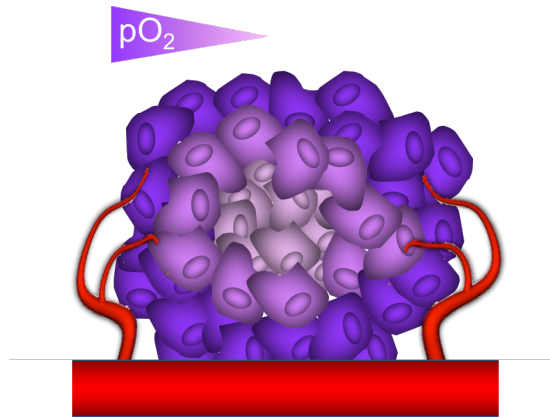


Figure II.16: From oxic to anoxic cells in tumors. Adapted from [Thambi et al., 2014]

OER is defined as the ratio of the dose required for a given biological end point (i.e. level of cell-killing, 10% surviving fraction) in a fully oxygenated medium to the dose required to achieve the same level in anoxic/hypoxic medium:

$$OER = \frac{D_{anoxic/hypoxic}^{SF_0}}{D_{oxic}^{SF_0}} \quad (II.32)$$

As mentioned previously (section 1.3.3), the radiosensitivity due to oxygen may be caused by the damage fixation reaction making the biological damage permanent. The importance of this mechanism relies on the indirect effect, and thus the quality of the radiation. For this reason, OER is dependent on LET and moreover, it decreases as the

1. INTERACTION OF CHARGED PARTICLES WITH BIOLOGICAL MATTER

LET increases as observed experimentally [Barendsen, 1968, Hirayama et al., 2015] (figure II.17). Because of the production of complex clustered damage at high LET, the oxygen fixation mechanism is less important than at low LET, and the dose required in well oxygenated medium and poorly oxygenated medium for the same cell-killing level tends to be the same (OER=1).

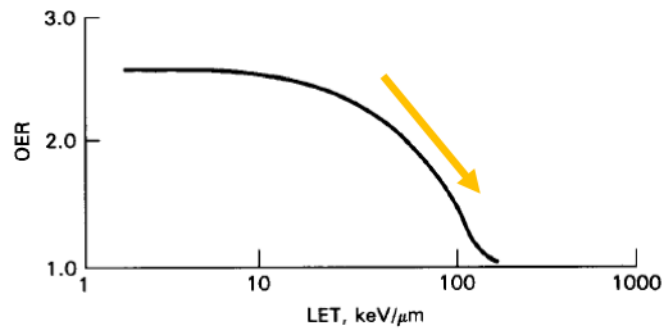


Figure II.17: The Oxygen Enhancement Ratio is shown as a function of the LET for a human cell line. All the data were collected with monoenergetic charged particles and 250 kVp X-rays, for which a LET of 1.3 keV/μm was assume. Adapted from [Barendsen, 1968]

2 Clinical set-ups for Ion Therapy

Particle therapy requires powerful particle accelerators in order to reach the energy necessary for a depth in tissue up to 30 cm. For protons and helium-ions, energies up to 250 MeV/u are required, for carbon-ions up to 430 MeV/u and for heavier ions, like oxygen-ions, more than 500 MeV/u. Hence, heavy ion beam therapies are considerable more expensive than protontherapy. Most therapy facilities offering exclusively protons are operated with cyclotrons, while facilities with heavy ions are using synchrotrons. Cyclotrons offer continuous beam and stable intensities. However, they do not provide the energy variation and a passive degrader is necessary. Synchrotrons offer fast energy variation (from pulse to pulse), but they need an injector and a delicate extraction system [Ma and Lomax, 2013].

Two major modalities are currently used to deliver the ion beam to the patient: passive scattering using a modulated broad beam (SOBP) to cover the total volume of the tumor and Pencil Beam Scanning (PBS) where a mini beam of various energies is scanned over the tumor. More details about this two modalities are given in section 2.1 and section 2.2 respectively.

The experiments with the passive scattering modality were performed at HIMAC and the experiments with the PBS system at HIT. A wider description of these particle therapy facilities is given below:

Heavy Ion Medical Accelerator (HIMAC, Chiba, Japan)

The National Institute of Radiological Science (NIRS) constructed HIMAC as the world's first heavy-ion accelerator facility dedicated to medical use. Since 1994, HIMAC has been treating cancer with high-energy carbon ions. NIRS-HIMAC has by far the greatest experience in carbon ion treatment worldwide.

The HIMAC accelerator complex consists of two ion sources, a linear accelerator and two synchrotrons. The primary accelerator accelerates ion beams (from H to Xe) up to 800 MeV/u. The size of the accelerator is about 50 m long and 25 m wide.

There are three clinical treatment rooms (A, B and C), one biological experiment room, two large general experimental halls, and a low-energy experimental room for the linac

2. CLINICAL SET-UPS FOR ION THERAPY

beams. Room A has a vertical beam line, room C and biological experiment room have a horizontal beam line in each, and room B has both vertical and horizontal. Identical irradiation systems, by passive scattering, are installed in each clinical treatment room and the biological experiment room.

Until 2011, patients were treated with the passive scattering delivery system. Static and moving tumors has been successfully operated with a pencil-beam 3D scanning (developed by NIRS), since May 2011. In addition, a heavy-ion rotating beam delivery system (gantry) has been developed with a superconducting technology and is in a beam-commissioning stage [Kamada et al., 2015, Noda et al., 2017].

NIRS has just started a study of a multi-ions irradiation for more sophisticated LET-painting and a design study of a superconducting synchrotron for more compact heavy-ion radiotherapy facility.

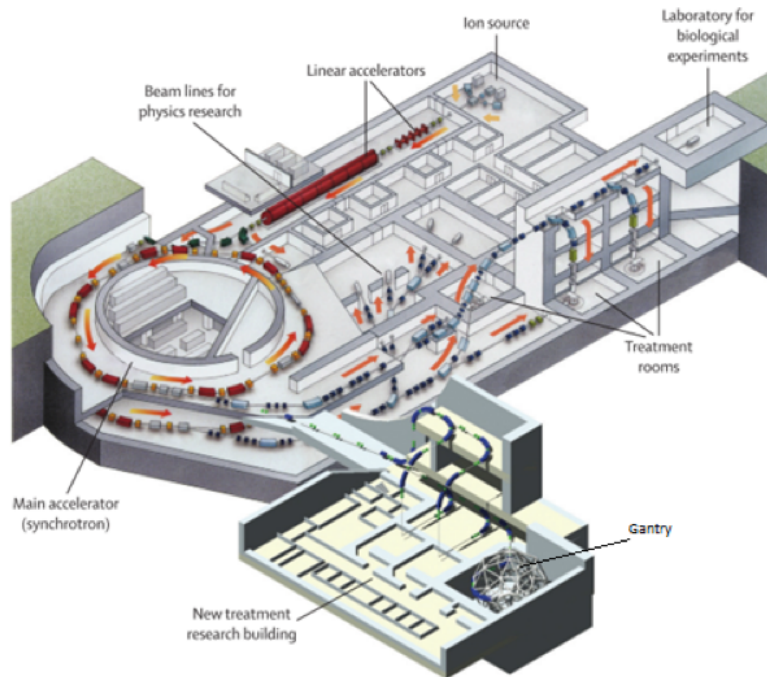


Figure II.18: Heavy Ion Medical Accelerator facility, Chiba, Japan. <http://www.nirs.qst.go.jp/ENG/core/cpt/cpt01.html>

Heidelberg Ion Therapy Centre (HIT, Heidelberg, Germany)

Since 1997, carbon-ion radiation therapy have been available in Germany at GSI. In 2000, GSI presented the feasibility study for the Heidelberg heavy ion therapy centre (HIT). The treatment of the patients at HIT started at the end of 2009, being HIT the first ion therapy facility who used intensity-modulated scanning in the world.

A library of pencil beams variable in energy, focus and intensity, ion species ranging from protons to oxygen are provided by a linear accelerator-synchrotron combination with a diameter of 20 m. HIT has two treatment rooms equipped with a horizontal beamline, and one with the world's first carbon ion gantry (figure II.19). In addition, there is one room equipped with a horizontal beamline with equivalent beam scanning technology dedicated to quality assurance and research, where we have performed our experiments. The maximal energy (for clinical applications) is 221 MeV/u for protons and 430 MeV/u for carbon ions [Combs et al., 2010].

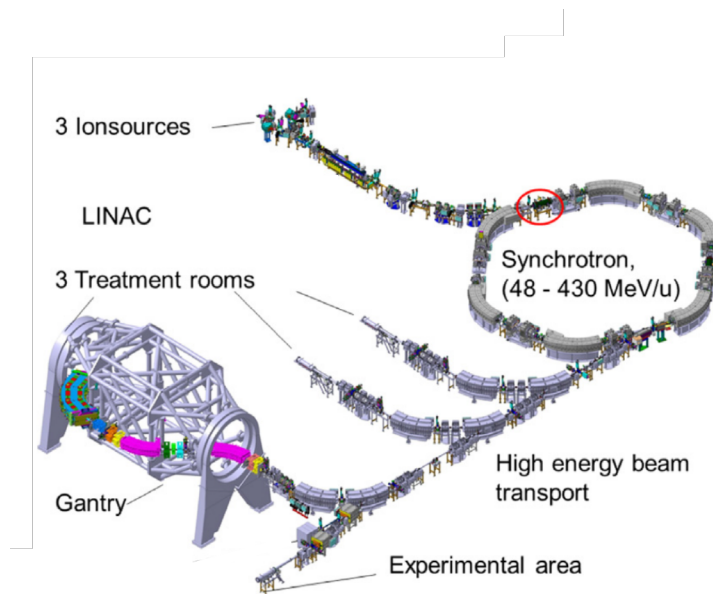


Figure II.19: Heavy Ion Therapy Centre at Heidelberg (HIT, Germany). Adapted from [Schoemers et al., 2015]

2.1 Passive scattering and Spread Out Bragg peak (SOBP)

Passive scattering, was the first method to be developed and still is most commonly used in proton and ion beam radiation therapy. As mentioned the experimental room at HIMAC is supplied by passive scattering. It comprises wobbler magnets, scatterer, neutron shutter, beam monitors, ridge filter, range shifter and collimators. A detailed description of this system is detailed in [Kanai et al., 1999, Torikoshi et al., 2007].

Briefly, the accelerated ion beam is focused on the irradiation delivery system, which is represented in figure II.21. A pair of wobbler magnets and a scatterer are used to produce uniform irradiation fields up to 22-cm diameter, which less than 2% intensity difference. The bar-ridge filter (BRF) is inserted in the beam course to produce the spread out Bragg peak (SOBP). When each mono-energetic ion penetrates through a different thickness. The ions have now different energies and thus different penetration energies (figure II.20). The SOBP is composed of various LET components with different weighting factors at each depth. The design of the ridge filter was aimed to result in uniform cell-killing by the beam in the SOBP [Kanai et al., 1997, Kanai et al., 1999].

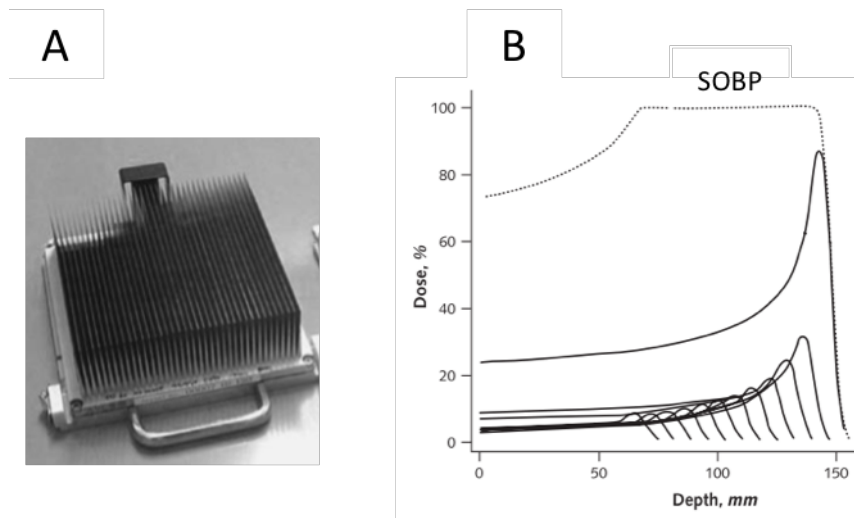


Figure II.20: A: Bar-ridge filter. Adapted from [Torikoshi et al., 2007]. B: Depth-dose distribution for a spread-out Bragg peak of an ion beam (dotted line). The dose distribution is created by adding the contribution of several single energy beams (pristine Bragg peak) (solid lines). Scheme adapted from [Terasawa et al., 2009].

Because only a few energy levels are available at HIMAC, an additional range shifter for fine tuning of the ion beam range (radiological desired depth in patients). It is placed

right after the BRF. The range is set in steps of 0.5 mm by selecting various thicknesses of polymethyl methacrylate (PMMA) plates of the range shifter. The irradiation field of each patient is defining by using a multileaf collimator. A bolus (compensator) can be used for shaping the distal part of the irradiation field according to the tumor shape. The bolus is made from a polyethylene block according to the designed shape using a treatment-planning system.

To reduce the secondary radiations like neutron to acceptable limits a neutron shutter is used. The irradiation dose to patients in the beam delivery is measuring using five monitors along the irradiation course. X-ray tubes and image intensifier detectors are used to fix the target on the irradiation site.

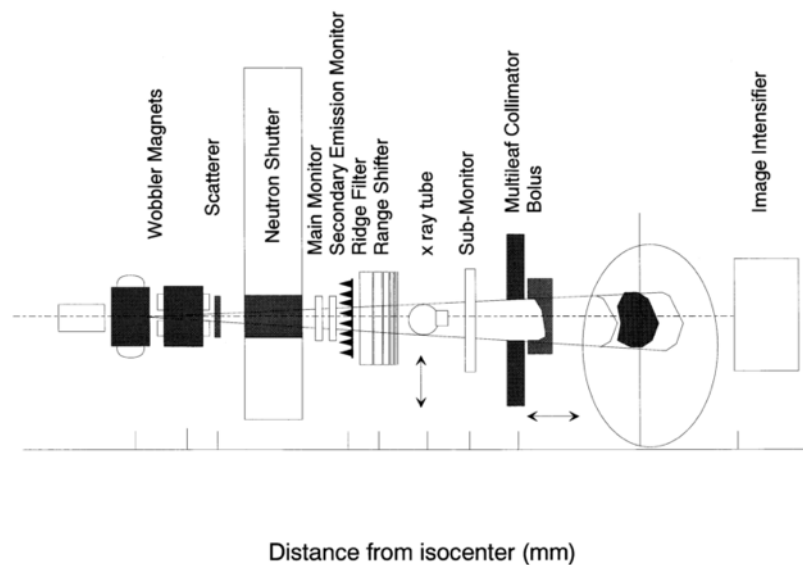


Figure II.21: The passive beam irradiation system of the treatment and experimental rooms at the HIMAC facility. Adapted from [Kanai et al., 1999]

The passive beam delivery technique has three important disadvantages. The dose is only shaped to the distant end of the target, but not to the proximal end. The compensator shifts the SOBP towards the entrance region and a considerable amount of dose is deposited in the normal tissue in front of the tumor. A large number of patient specific compensators needs to be produce. In addition, the amount of material line along the beam course leads to an increase in nuclear fragments which have low energy and thus high LET. This residual radiation increase the biological effective dose of the beam in the entrance region.

2.2 Pencil Beam Scanning (PBS)

The pencil beam delivery system is a more advanced irradiation deliver technique that allows to improve the radiation dose conformity compared to passive scattering. This technique was developed in the early 1990s almost in parallel at PSI (Switzerland) for protons and at GSI (Germany) for heavy ions. Both the spot scanning system (PSI) and the raster scanning system (GSI) represent fully active techniques in the sense that no passive elements are used for adapting the dose deposition optimally to the target volume. The first commercial ion scanning system was introduced at HIT in November 2009.

The basic principle of the raster scanning system is shown in figure II.22. The pencil like beam is moved in horizontal and vertical direction by fast deflection magnets and, in contrast to passive scattering technique, no scattering device is required. When the desired dose, which is controlled by the beam monitor, in one voxel is reached, the beam is moved to the next voxel. The spacing between adjacent raster points is typically 2 mm and smaller than the beam-spot. The treatment dose is delivered slice by slice. Each slice correspond to a constant beam energy. After completion of one slice the synchrotron beam extraction is instantly interrupted and the beam energy for the next slice is selected and delivered with the next synchrotron pulse. The scanning control system is linked with the accelerator control system and request the appropriate beam parameters for each slice irradiation during execution of the treatment plan [Haberer et al., 1993]. PBS adapts the dose distribution to any complex shape of the target volume, individually for each patient and without any patient-specific hardware.

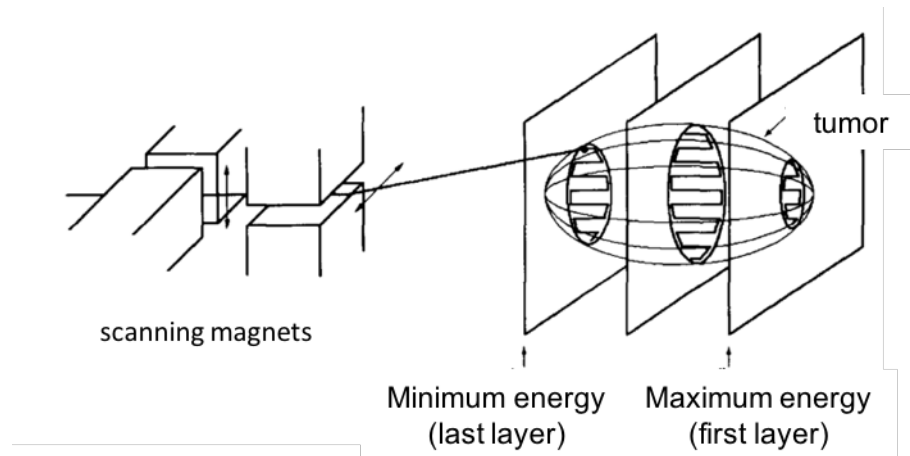


Figure II.22: Pencil beam scanning irradiation system used at HIT facility. Adapted from [Haberer et al., 1993].

2.3 PBS versus passive scattering (SOBP)

When a passive scattering is used, the modulation of the primarily Bragg peak into a broader peak cause a continuous fluctuation of LET values throughout the SOBP. The fluctuation of the LET causes a variation of the biological effect. The modulation of heavy ions beams has to be taken into account more seriously than the modulation of proton beams. Since protons are low LET radiations and thus RBE close to 1, the SOBP requires only a uniform dose distribution throughout the target tissues. For this reason, data on cellular inactivation resulting from mixed irradiation with heavy ion beams of different LET are needed to design the SOBP [Kanai et al., 1999]. Understanding the relationship between the biologically relevant effects induced by SOBP, and how this relationship depends on cell radiosensitivity is essential for a radiobiological comparison of different beams as well as for improving radiobiological models to be used in treatment planning.

Belli and co-workers studied the carbon-ion induced inactivation of several cancer and normal cell lines irradiated either with monoenergetic carbon beams or at different positions along a carbon ion beam SOBP. For monoenergetic beams, the general trend is a decrease in the surviving fraction – at a fixed dose of 2 Gy – with increasing LET up to 94 keV/ μm followed by an increase at higher LET values. At the highest LET value (303 keV/ μm), the differences in the surviving fraction at 2 Gy among the various cell lines are strongly reduced. SOBP irradiation also resulted in an increase in cell inactivation with LET_d. The LET dependence of cell inactivation was more pronounced in photon

radioresistant cell lines [Belli et al., 2008].

Belli's work reported the RBE values relative to SOBP and monoenergetic beams. The RBE values for SOBP beams are lower than those relative to monoenergetic beams, such differences depends on the cell line. Larynx cancer cells have shown differences in its survival curve shape depending whether they are irradiated with monoenergetic or SOBP beams. Mixed fields tends to increase the curvature. Not only the RBE values for the two beams are expected to differ, but this difference will also depend on the level of biological effect that is considered. The difference between the responses to monoenergetic and SOBP carbon-ion beams poses the question whether the dose-averaged LET in a point of a SOBP carbon beam is equivalent, from the radiobiological point of view, to the same LET of a monoenergetic beam. They concluded that mixed fields as those generated by SOBP beams are less effective than monoenergetic beams of the same dose-averaged LET and therefore, their biological effectiveness cannot be evaluated through this parameter. If the LET distribution along the SOBP is large enough to include high LET values that fall close or beyond the RBE maximum, then the "overkill" effect could result in a further decrease in the biological effectiveness of the beam. Low LET fragments in the SOBP could also play a role.

The RBE variations with LET, which were smaller for radiosensitive than for radioresistant cell lines following irradiation with monoenergetic beams, were even smaller for SOBP irradiation. This observation clearly indicates that those cells that are relatively resistant to photons and whose response varies considerable when more densely ionizing radiation is used, are on the contrary sensitive biological detectors of variations in radiation quality along SOBP.

The biological response resulting from mixed irradiation with high- and low- LET beams depends not only on the LET_d of mixed beams but also on the LET spectra of the mixed beams [Kanai et al., 1999].

Chapter III

Materials and methods

In this section, the material and the experimental protocols are presented. It includes the description of the NPs characteristics (section §1), the cell lines characteristics and the preparation of the samples (section §2), as well as the description of the methods to localize (section 3.1) and quantify the NPs in the cells (section 3.2). The different sources and protocols of irradiation (ions and photons) are described in section §4 with a particular emphasis on the different oxygenation conditions. The experimental analysis of the radiation effect is presented in section §5.

1 Characteristics of nanoparticles

Two different NPs were chosen for the purpose of this thesis project: gold and platinum NPs. Both NPs consists of a spherical metal core of about 3 nm diameter. They are biocompatible and stable in a wide range of pH in a biological medium. In addition, the synthesis is reproducible and NPs can be stored for several weeks. The synthesis of these agents was not a purpose of my work, but a brief description of the NPs characteristics is presented here.

1.1 Gold NPs

Gold NPs (AuNPs) were synthesized in the laboratory of Professor Stéphane Roux (Bourgogne - Franche-Comté University, UTINAM, Besançon) by Gloria Jimenez Sanchez during her PhD thesis (2013-2017, Bourgogne - Franche-Comté University) and Farhan Bouraleh Hoch (2nd year PhD, Bourgogne-Franche-Comté University).

AuNPs are obtained by chemical synthetization according to the protocol of Brust et al. (1995). $\text{HAuCl}_4 \cdot 3\text{H}_2\text{O}$ is reduced with NaBH_4 in the presence of thiols (stabilizers) to ensure control of the size and the stability of the colloid [Brust et al., 1995, Miladi et al., 2014]. The stabilizer consists of a dithiolated derivate of the diethylene-triaminepentaacetic acid (DTPA), named DTDTPA, which is provided by ChemaTech (Dijon, France). The use of appropriated biocompatible ligand allows the production of NPs without further chemical treatment, except purification.

Gold core diameter was shown to be 2.4 ± 0.5 nm. With DTDTPA conjugation, its hydrodynamic size to 6.6 ± 1.8 nm (see figure III.1). The overall surface charge is -29.6 eV at pH 7.4. These NPs exhibit a homogenous distribution in solution with a polydispersity Index (PdI) of 0.30 ± 0.02 [Alric et al., 2013]. These measurements were also performed in cellular complete medium containing 10% FBS and no significant changes were observed. This indicates a high degree of stability [Butterworth et al., 2016].

AuNPs present several advantages. Our interest on AuNPs relies on its ability to induce the destruction of cancerous cells after external activation by radiation [Butterworth et al., 2012]. They can be functionalized with additional ligands. For *in vivo* and *in*

1. CHARACTERISTICS OF NANOPARTICLES

in vitro studies using fluorescent techniques, AuNPs are labelled with cyanine (Cy5) (an organic fluorescent dye). *In vivo* experiments have demonstrated that AuNPs circulate freely in the blood vessels without undesirable accumulation in the lungs, spleen and liver [Alric et al., 2013]. They can also be functionalized with Gd ions. The presence of Gd^{3+} ions entrapped in the organic shell was demonstrated to enhance the image contrast of Magnetic Resonance Imaging (MRI). In addition, gold core provides a strong X-ray absorption. These properties makes AuNPs-Gd a good candidate as contrast agents for X-ray computed tomography (CT) imaging and MRI [Alric et al., 2008, Debouttière et al., 2006]. The development of these powerful NPs opens the possibility to use AuNPs as a contrast agent for diagnosis and radio-enhancer for radiotherapy (theranostic).

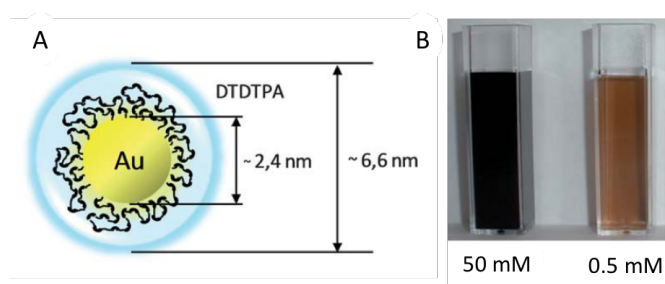


Figure III.1: (A) Schematic representation of AuNPs. (B) Photograph of AuNPs colloids containing 50 mM Au and 0.5 mM Au. Adapted from [Alric et al., 2013].

1.2 Platinum NPs

Platinum NPs (PtNPs) were synthesized by radiolysis and developed in the thesis of Erika Porcel (2008-2011, Paris Sud University) under the direction of Sandrine Lacombe in collaboration with Hynd Remita (University Paris Sud, LCP). The method was then improved during the thesis of Daniela Salado (2013-2016, Paris Sud University) who provided the PtNPs for my work.

Briefly, an aqueous solution containing $(Pt(NH_3)_4Cl_2 \cdot H_2O)$ and poly(ethylene glycol) (PEG) ($H(OCH_2CH_2)nOH$) ($n \sim 22.3$) was deaerated by bubbling with nitrogen and exposed to a panoramic ^{60}Co gamma source at the dose rate of $95.5 Gy.min^{-1}$. Thanks to water radiolysis, reductive species appear in the solution which reduce the Pt^{2+} ions in metal Pt^0 , which then aggregate in small NPs. The major added value of this method is the absence of additional chemicals to reduce the precursor and the possibility to *in situ* coating the metal NPs with biocompatible polymers. Moreover gamma radiation sterilizes the solution and no further purification is necessary for biological use.

PtNPs are composed of a spherical core of 3.2 ± 0.8 nm. The hydrodynamic size in water is 8.8 ± 3.1 nm (see figure III.2). The overall surface charge is -16.6 ± 5.1 eV at pH 7. PtNPs exhibit a homogenous distribution in solution with a PDI of 0.238 ± 0.004 . No significant changes were observed in cellular complete medium contained 10% FBS (PhD thesis of Daniela Salado, 2013-2016). In particular, these NPs are of great interest since its surface allows the grafting of specific molecules for developing functionalized nano-agents. PtNPs grafted with fluorescent ligands for *in vivo* biodistribution are still in development.

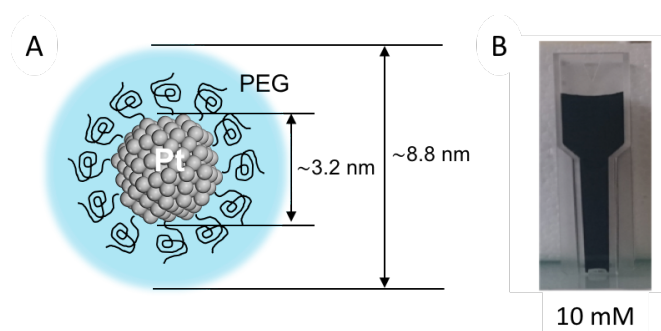


Figure III.2: (A) Schematic representation of PtNPs. (B) Photograph of PtNPs colloids containing 10 mM Pt.

2 Cellular models

The effect of AuNPs and PtNPs was probed using two human immortalized cell lines, HeLa (ATCC[®] CCL-2[™]) and BxPC-3 (ATCC[®] CRL-1687[™]), which correspond to cervix uterine and pancreatic cancers cells, respectively. Both cancer types are resistant to conventional cancer therapies and nowadays, if possible, treated under carbon-ion radiation therapy [Kamada et al., 2015].

2.1 HeLa cells

HeLa cells were derived from cervix uterine cancer in 1951 from a 31-years-old black woman. Their morphology is epithelial and they are adherent in cell culture. They have a doubling time of about 24 hours and plating efficiency of 50-60%.

They were the first immortalized human cancer line. Their remarkable resistance and proliferation drew the attention of researchers and became a commonly used model in cell biology which led to numerous medical breakthroughs [Rahbari et al., 2009].

Despite adjuvant treatment with radiation and chemotherapy in addition to radical surgery [Höckel et al., 1991], clinical observation has shown that tumor hypoxia in cervical carcinoma is involved in the malignant progression of the disease: high probability for lymphatic spread and for recurrence.

2.2 BxPC-3 cells

BxPC-3 cells were derived from pancreatic cancer in 1980 from a 91-years-old white woman. Their morphology is epithelial and they are adherent in cell culture. They have a doubling time of 48-60 hours and a plating efficiency of 10-20% [Tan et al., 1986].

The lethality of pancreatic cancer relies on the late diagnosis and resistance to conventional radiotherapy [Garrido-Laguna and Hidalgo, 2015]. The work published by Koong et al. (2000) showed the first evidence that a significant population of tumor cells within pancreatic cancers is hypoxic [Koong et al., 2000].

2.3 Cell sample preparation

HeLa and BxPC-3 cells were grown in Dubelcco's Modified Eagle Medium (DMEM) and RPMI-1640, respectively. The medium was enriched with 4.5 g/L glucose and supplemented with 10% foetal bovine serum, 1% antibiotics (100 U/mL penicillin, 100 μ g/mL streptomycin) and 1% glutamine. Cells were cultured at 37°C in a humidified 95% air / 5% CO₂ atmosphere. The cell passage was performed at confluence (~80%) using 0.05% trypsin-EDTA.

Cells were seeded on flasks, dishes or bio-foils, depending on the experimental set-up, 24 h prior to irradiation. Details on the number of cells seeded, as well as the surface of the sample holder, are given in the experimental protocols (section 4.1 and section 4.2).

3 Nanoparticles uptake

3.1 Localization of NPs in the cells

Confocal microscopy was used to characterize the localization of AuNPs in the cells. The experiments are based on the measurement of the fluorescence signal of fluorophores grafted on the NPs. In this purpose, AuNPs were grafted with cyanine 5 (AuNPs-Cy5). In the work of Vladimir Ivosev (ESR of the ARGENT Project and supervised by S. Lacombe) was found that the presence of this ligand does not affect the AuNPs uptake.

The confocal images were recorded with a LEICA SP5 confocal system at the Centre de Photonique BioMédical (CPBM) which is located at the Centre Laser de l'Université Paris-Sud (CLUPS) (Orsay, France) (figure III.3). The experiments were performed in collaboration with Sandrine Lécart (research engineer at CLUPS), Michaela Ferencakova (PhD student at the University of Pavol Jozef Šafárik, Košice, Slovakia) and Fiona Cesarin (undergraduate student, Vallée de Chevreuse High School, Gif-sur-Yvette, France).

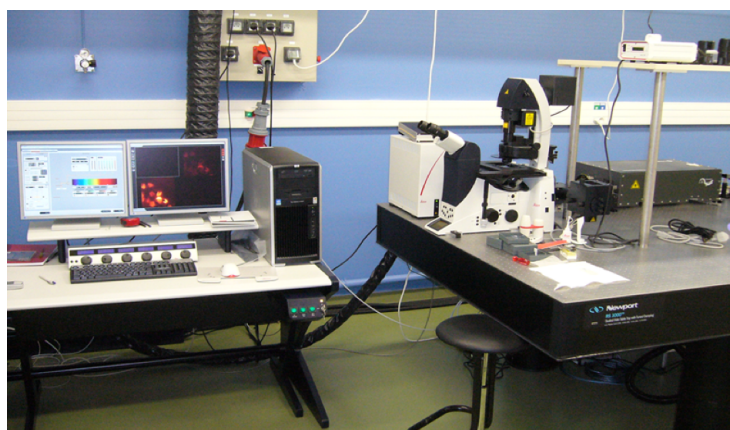


Figure III.3: Confocal microscope at the “Centre de Photonique BioMédical” (CPBM), Laser Center of the University Paris Sud (CLUPS) (Orsay, France)

Cell localization

50,000 HeLa or BxPC-3 cells were grown in 8-well LabTek chambers 1 day before the imaging. Cells were incubated with 0.5 mL of medium containing AuNPs-Cy5 (0.5 mM Au) for 1 or 20 h before the imaging. After incubation the cells were rinsed with

phosphate buffered saline 1x and transparent DMEM or Hank's Balanced Salt Solution (HBSS) was added to HeLa and BxPC-3 cells respectively. Since the microscope is mounted in a thermostatted enclosure which is regulated in CO₂, it is possible to perform the images in living cells so that, no fixation of cells was required.

Cyanine 5 was excited at 633 nm and the fluorescence emission was detected in the 650-750 nm range. The localization was studied in around 30 cells. Images were processed with the ImageJ software.

Co-localisation with cell organelles

50,000 BxPC-3 cells were grown in 8-well LabTek chambers 1 day before the NPs incubation. BxPC-3 were incubated with LysoTracker-green (Invitrogen) (75 nM) or MitroTracker-green (200 nM) overnight. The trackers were washed out with phosphate buffered saline before incubation during 1 h with 0.5 mM of AuNPs-Cy5. After NPs incubation the cells were rinsed with phosphate buffered saline, fixed using 4% paraformaldehyde (PFA) and phosphate buffered saline 1x was added. The samples were kept in the fridge during few days for its observation.

The lysotracker and mitotracker were excited at 488 nm and the fluorescence emission was detected in the 505-600 nm range. The trackers have no spectral overlap with Cy5 (excitation at 633 nm and fluorescence emission at 650-750 nm). The co-localization were calculated for more than 15 cells. The co-localization of AuNPs was quantified using the ImageJ software and the JACoP statistical plug-in.

3.2 Quantification of NPs in the cells

The intracellular concentration of gold and platinum was measured using Inductively Coupled Plasma – Mass Spectrometry (ICP-MS). The cells were incubated with AuNPs or PtNPs for different incubation times (6 or 20 h) at various concentrations (0.5 or 1 mM). Then, the cells were washed with phosphate buffered saline, harvested, counted and centrifuged. The remaining solution (supernatant) was discarded. The pellet containing around 2 million cells was kept in a centrifuge tube and frozen (-80 °C). The tubes were sent in dry ice to Ultra Trace Analyses Aquitaine (UT2A) technological center (Pau, France) who was in charge of the ICP-MS measurement. The center UT2A provided the quantity of Pt and Au found in each sample expressed in ng of Pt or Au per tube.

3. NANOPARTICLES UPTAKE

The number of AuNPs or PtNPs per cell was calculated using the following equation:

$$\left[\frac{NPs}{cell} \right] = \frac{[ng/tube]}{[cells/tube]} \times \frac{N_A}{M_w} \times 10^{-9} \times \frac{1}{[atoms/NP]} \quad (III.1)$$

where:

$$N_A = 6.022 \times 10^{23} \text{ mol}^{-1}$$

$$M_w(Au) = 196.97 \text{ g/mol}$$

$$[\text{atoms of Au / AuNPs}] \sim 400$$

$$M_w(Pt) = 195.08 \text{ g/mol}$$

$$[\text{atoms of Pt / PtNPs}] \sim 1,000$$

4 Irradiation protocols under anoxic conditions

In this section, we present the protocols and setup used during the irradiation experiments. Different radiation sources were used in this work: two ions (carbon and helium), two ion beam delivery systems (passive scattering and PBS) and a photon irradiation source. The objective was to study the amplification effect of AuNPs and PtNPs under three different oxygen conditions: oxic ($pO_2 = 20\%$), hypoxic ($pO_2 = 0.5\%$) and anoxic ($pO_2 = 0\%$).

4.1 Passive scattering

The irradiation experiments using passive scattering beam delivery system were performed at HIMAC (chapter II, section §2). The experiments were performed in collaboration with Dr. Ryoichi Hirayama (National Institutes for Quantum and Radiological Science and Technology, QST, NIRS, Chiba, Japan) and Dr. Noriko Usami (High Energy Accelerator Research Organization, KEK, Tsukuba, Japan). We counted with the kindly support of Prof. Yoshiya Furusawa (QST-NIRS, Chiba, Japan).

Figure III.4 displays photographs that corresponds to the whole setup used for irradiation experiments in oxic and anoxic conditions at HIMAC. A picture of the gas chamber in front of the ion exit at the irradiation room is shown in figure III.5.

The procedure including the sample preparation, the NPs incubation, the de-oxygenation and the irradiation is described below:

- Cell preparation – 24 h before irradiation

200,000 cells were seeded onto custom-made glass dishes (34 mm of diameter) one day before the irradiation. The dishes have a lid to prevent any leakage of the medium while the cells were standing vertically in front of the horizontal ion beam. Because the medium was kept in the pocket formed by the lid during the irradiation, cells were only seeded in the dish's surface that is not covered by the lid. This was done to avoid irradiation of cells through the cell culture medium. (figure III.4A).

4. IRRADIATION PROTOCOLS UNDER ANOXIC CONDITIONS

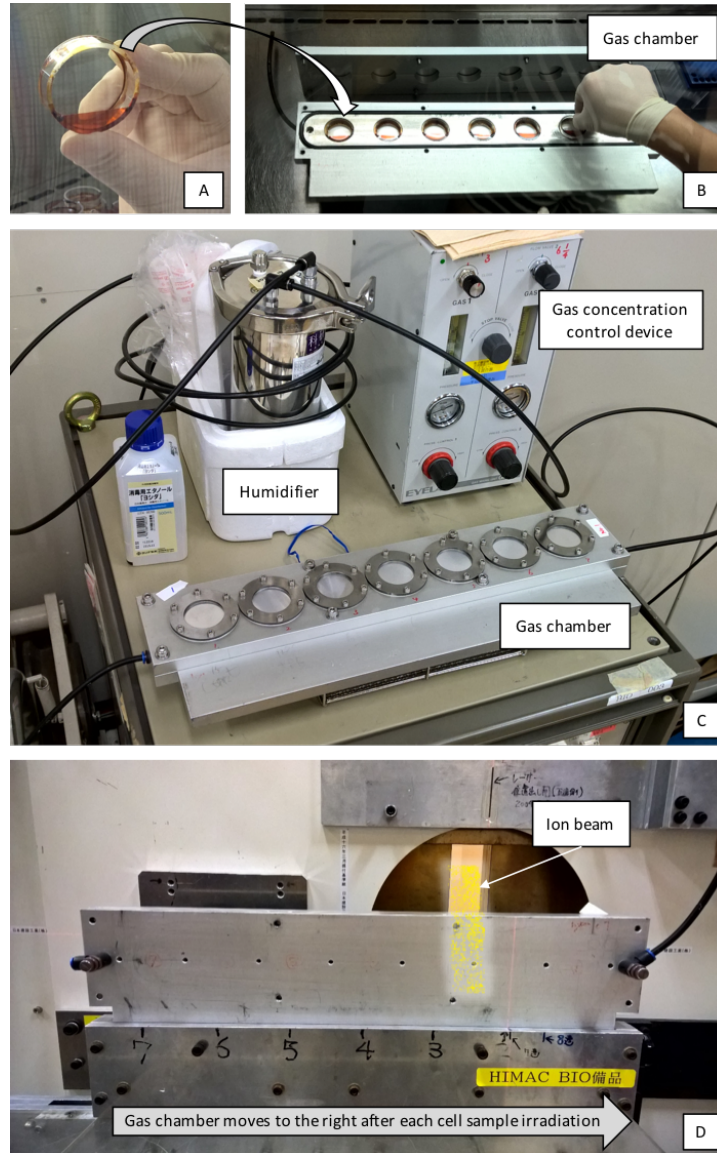


Figure III.4: A) Custom-made glass dish. B) Inside of the gas chamber. C) The gas chamber is closed and connected to the control apparatus and the humidifier. D) Gas chamber positioned vertically in front of the ion beam. The chamber moves automatically to the right after each sample has been irradiated.



Figure III.5: The gas chamber is placed in front of the beam exit at the irradiation room of HIMAC.

– Incubation of cells with NPs – 6 or 20 h before irradiation

The final NPs concentration in medium was 0.5 or 1 mM for AuNPs and 0.5 mM for PtNPs. The initial concentrations of AuNPs and PtNPs were 45 mM and 10 mM, respectively. The initial volume of AuNPs solution required to obtain a final concentration of 0.5 mM Au in medium was 4.5 times smaller than the initial volume of PtNPs solution needed to obtain 0.5 mM Pt. Sterilized filtered water was added in the AuNPs sample as well as in the medium used in the control samples to make the water volumes equal with AuNPs and PtNPs.

Cells were incubated with 3 mL of medium with or without NPs 6 or 20 hours before irradiation. After 5 or 19 hours, the medium with or without NPs was reduced to 0.9 mL. In this way, the medium stays inside the lid while the sample is in the vertical position. This way, the medium and the NPs contained in it did not affect the irradiation effects.

– De-oxygenation of the samples – 1 h before irradiation

Seven dishes were inserted in the wells that compose the gas chamber. Once the chamber was hermetically sealed, a system of hose couplings was used to allow the exit of the atmospheric air and the entrance of the mixture gas required for the study. The gas

4. IRRADIATION PROTOCOLS UNDER ANOXIC CONDITIONS

mixture was made by the gas-concentration control device fed by N₂, CO₂ and air. A humidifier is additionally placed in between the control device and the gas chamber to maintain humidity. The whole set-up was developed by Y. Furusawa at NIRS and adapted to our experiment by R. Hirayama.

To achieve anoxic conditions (0% O₂, 95% N₂ and 5% CO₂), the gas chamber was flushed for 1 h just before irradiation with a mixture of N₂/CO₂ (1000/50 mL/min). The pO₂ level in the hypoxia medium was measured in previous works using an oxygen electrode as described elsewhere and it was consistently found to be less than 0.2 mmHg (0.0026%) [Hirayama et al., 2009]. For hypoxic conditions (0.5% O₂, 95% N₂ and 5% CO₂), the gas chamber was flushed for 1h prior irradiation with a mixture of N₂/CO₂/air (950/50/25 mL/min). For oxic conditions, dishes were placed in the hypoxic chamber only 30 min before irradiation (figure III.4B and C).

– Irradiation

After 1 h of gas flushing, the gas chamber's valves were closed to avoid any gas exchange during the irradiation. One dish was irradiated at a time. When the desired dose of a cell sample was achieved, the gas chamber was moved automatically to place the next sample in front of the beam. Each dish corresponds to a different irradiation dose. Each chamber contains all the dose points needed to build a complete survival curve at a defined condition (figure III.4D).

A complete survival curve in oxic conditions takes 10-15 minutes and in anoxic conditions, 20-25 minutes. Irradiation experiments were performed in slots of 4 hours where up to 8 survival curves were measured. A total of 11 slots (44 hours of beam) were necessary for this project.

– Beam features

The irradiation was done using a passive beam delivery system. The beam diameter is 10 cm and the dose homogeneity is $\pm 5\%$ in this area. Ions pass through the collimator (25 x 5 cm). Carbon- and helium-ions at different LET_ds were used for the experiments. The initial carbon ion energy was 290 MeV/u, similar to the one used for patient treatments.

For helium ions, we used an initial energy of 150 MeV/u. A SOBP of 6 cm was chosen for both ions with the perspective of performing *in vivo* experiments under the same conditions. Cell samples were irradiated at the centre of the SOBP. The dose rate for carbon- and helium-ions was ~ 3 Gy/min. The LET_d for carbon- and helium-ions at the centre of the SOBP is 50 and 12 keV/ μ m, respectively [Kanai et al., 2006]. As an example, the LET_d as a function of depth in water for carbon ions is presented in figure III.6.

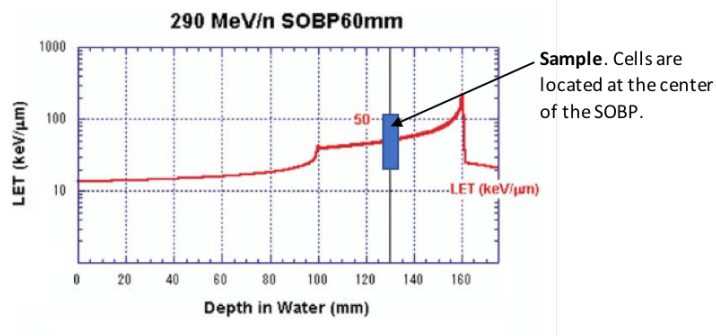


Figure III.6: Dose-averaged linear energy transfer (LET_d) as a function of depth in water for spread-out Bragg peak (SOBP) beam of 6 cm width for carbon-ions. Adapted from [Kanai et al., 2006].

4.2 Pencil Beam Scanning

The experiments with the PBS delivery system were performed at HIT. They were carried out in collaboration with Daria Boscolo, ESR of the ARGENT project and PhD student at GSI, Darmstadt, Germany. She was supervised by Emanuele Scifoni (researcher at TIFPA, Trento, Italy), Michael Kraemer (researcher at GSI) and Marco Durante (director of TIFPA). The project was also performed with the help of Olga Sokol (PhD student at GSI), Julia Wiedemann (post-doc at GSI) and Walter Tinganelli (researcher at TIFPA).

Figure III.7 shows the set-up used for irradiation experiments in anoxic conditions at HIT.

4. IRRADIATION PROTOCOLS UNDER ANOXIC CONDITIONS

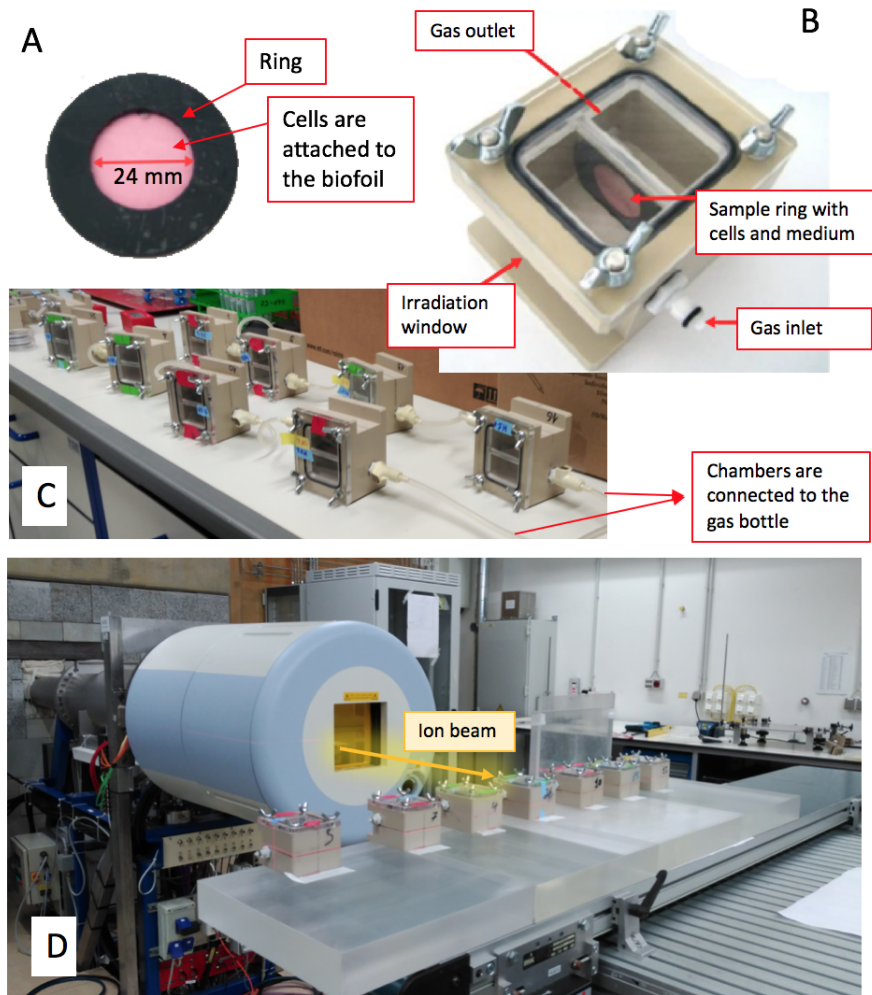


Figure III.7: Hypoxic set-up used at HIT. A) Cell support composed of a ring and two biofoils pasted on each side. B) Individual hypoxic chamber. Adapted from [Walter Tinganelli, 2012]. C) Individual chambers connected in between them and to the gas bottle. D) Serie of individual chambers placed vertically on the irradiation table.

The procedure including sample preparation, NPs incubation, de-oxygenation and irradiation is described below:

– Cell preparation – 24 h before irradiation

The cell support consists on a ring made of polyvinyl-chloride. The ring has an internal diameter of 24 mm and a thickness of 3 mm. One side of the ring was covered with a gas permeable biofoil of 25 μm thickness. 150,000 cells were seeded onto the biofoil one day before irradiation (figure III.7A).

– Incubation of cells with NPs – 6 h before irradiation

Cells were incubated with 1.3 mL of medium with/without AuNPs (0.5 mM Au) 8 h before irradiation. After 6 h, the medium was changed to 1.5 mL of fresh medium. The ring was then sealed with a second biofoil. This way, the medium without NPs was confined between the two biofoil while the chamber was irradiated vertically. No NPs was contained in the medium during the irradiation to avoid any effect of NPs in solution.

– De-oxygenation of the samples – 1 h before irradiation

Each sealed ring was inserted 2 h prior irradiation in individual gas chambers. The chamber were developed and patented at GSI [Schicker et al., 2009]. The chamber is cut out of one piece of polyetheretherketone (PEEK). The front wall is used as irradiation window and has a thickness of 1mm. The top cover is transparent made of polymethylmethacrylate (PMMA) and allows positioning of the sample ring. A system of hose couplings allows to exchange the gas of the individual chambers.

For achieving anoxic conditions (0% O₂, 95% N₂ and 5% CO₂), the irradiation chambers were flushed for 2 h just before irradiation with 200 mL/min using a gas bottle containing 95% N₂ / 5% CO₂. The gas flow was measured in previous work of GSI with a thermal mass flow meter and the expected oxygen level was correct. For oxic conditions, rings were placed in the chambers 2 h before irradiation and kept outside the incubator (figure III.7B and C).

4. IRRADIATION PROTOCOLS UNDER ANOXIC CONDITIONS

– Irradiation

After 2 h of gas flushing, the gas bottle was disconnected and the hose couplings kept gas-tight afterwards for irradiations. One sample was irradiated at a time. When the dose required for a sample was achieved, the table moves horizontally and a new sample is placed in front of the beam. Each individual gas chamber corresponds to a different irradiation dose. All the gas chambers necessary for building a complete surviving curve are placed on the irradiation table. After the irradiation the cells were harvested and prepared for the clonogenic assay. A new series of samples were placed on the table and the next irradiations were executed (figure III.7D).

A complete survival curve in oxic conditions takes 10-15 minutes and in anoxic conditions, 20-25 minutes. Irradiation experiments were performed in slots of 5 hours where up to 5 survival curves were measured. A total of 7 slots (35 hours of beam) were necessary.

– Beam features

Two ion beams have been used for the experiments, carbon-ions. The LET_d used for carbon ion was 50 and 100 keV/ μm . Because the pristine Bragg peak of a single ion energy produces a sharp gradient of LET, 5 to 11 energy slices were scanned to form a broader beam. In this way, we obtained an homogeneous LET on the position of the cell sample.

The initial energies for carbon-ions varied from 106 up to 153 MeV/u. The irradiation was performed using PBS beam delivery system. A dose homogeneity of $\pm 5\%$ was achieved. A few-tens-millimeters thick bolus made of poly(methyl methacrylate) (PMMA) was used to tailor the energy beam so that the desired LET takes place at the position of the cell sample. As an example, the LET_d and the dose versus the depth for carbon-ion radiation (configuration used to obtain a LET_d of 100 keV/ μm , 35-mm depth) is shown in figure III.8.

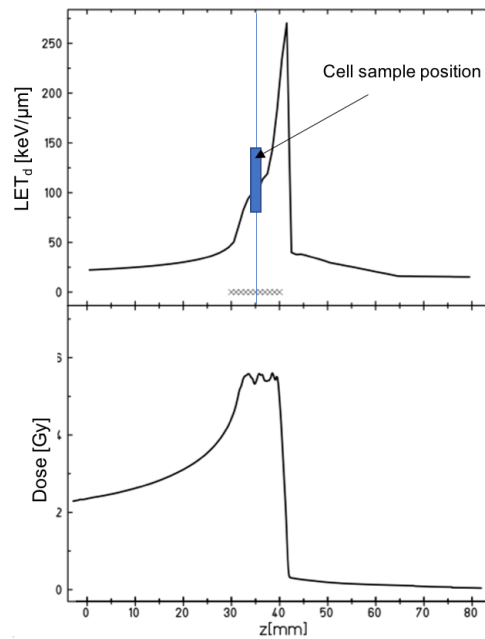


Figure III.8: LET_d and dose versus the depth for carbon-ion radiation (configuration used to obtain a LET_d of $100 \text{ keV}/\mu\text{m}$ 35-mm depth). 5 different energy slices within the range from 124.5 to 136.9 MeV/u were scanned to obtain a homogenous LET over a 10 mm depth.

4.3 Gamma-rays

The experiments were performed with a $^{137}\text{cesium}$ source located at the Institut Curie (Orsay, France). Cells were irradiated with gamma rays of 0.662 MeV energy. The dose rate was close to $0.9 \text{ Gy}/\text{min}$ at the sample position. 200,000 cells were seeded per cell flasks (surface of 25 mm^2) the day before the irradiation. The flasks were placed horizontally so that cell layer face the source.

5 Experimental analysis of radiation effects

5.1 Quantification of cell killing by clonogenic survival assay

The effect of radiation combined with NPs at cellular scale was quantified using the clonogenic survival assay. This method is commonly used in radiobiology and evaluates the cell response to a certain treatment. It allows to determine the ability of a cell to proliferate and form a colony (50 or more cells). After a certain treatment only a fraction of cells has the capacity to produce colonies. The number of colonies is indicative of cells that are not affected by the treatment. In particular, this assay allows us to quantify the efficiency of a radiation treatment with and without NPs.

The method of clonogenic survival assay is the following: after irradiation, cells were harvested and seeded in 10 cm petri dish (in triplicates) at different densities to achieve 100 or 50 colonies per dish for HeLa and BxPC-3 respectively. After two weeks, colonies were fixed and stained using a solution of 0.5% methylene blue and 50% v/v methanol solution in water (figure III.9).

A cell survival curve is therefore defined as a relationship between the radiation dose and the percentage of cells that survived the treatment at a given dose (surviving fraction, SF).

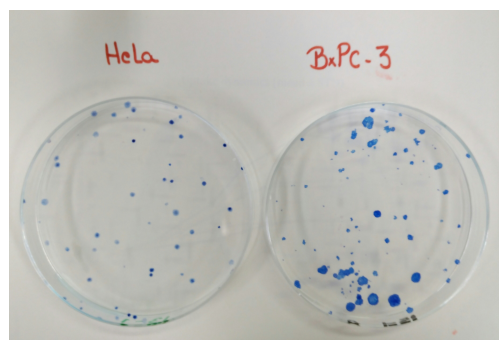


Figure III.9: Petri dishes containing HeLa (left) and BxPC-3 colonies (right). They correspond to control samples (0 Gy, no irradiation).

5.2 Quantification of the NP impact: definition of SER, DEF and RBE

The efficiency of NPs to amplify radiation effects was quantified using various indicators extracted from the SF measurements.

- **Radiation sensitizing enhancement ratio (SER).** This parameter is indicative of the enhancement of the radiation effect in to the presence or not of NPs at a defined dose point.

$$SER (\%) = \frac{SF_{control}^{D_0} - SF_{+NPs}^{D_0}}{SF_{control}^{D_0}} \quad (III.2)$$

where $SF_{control}^{D_0}$ and $SF_{+NPs}^{D_0}$ are the SF of the control cell sample and the cell sample incubated with NPs respectively irradiated at a certain dose (D_0).

- **Dose Enhancing factor (DEF).** It is the ratio between the radiation dose needed to achieve a certain biological effect in the cells free of NPs ($D_{control}^{SF_0}$) and the radiation dose to obtain the same biological effect (SF_0) when NPs are present ($D_{+NPs}^{SF_0}$). This indicator is commonly calculated for 10% of SF.

$$DEF = \frac{D_{control}^{SF_0}}{D_{+NPs}^{SF_0}} \quad (III.3)$$

- **Relative Biological Effectiveness (RBE).** It is used to quantify differences in the biological and clinical effects of radiations. It is the ratio of the irradiation dose of photons used as a reference radiation ($D_{photons}^{SF=0.1}$) to that of another radiation (ions, $D_{ions}^{SF=0.1}$), which results in the same biological effect under identical conditions. The RBE is a key parameter used by oncologist and medical physicists to adapt the dose delivery according to a novel therapeutic approach. In particular, for this work, we determined the RBE of ions in the presence or not of NPs ($D_{ions,control}^{SF=0.1}$ and $D_{ions,+NPs}^{SF=0.1}$) using gamma-rays as reference. The RBE is commonly evaluated at 10% of survival.

$$RBE_{control} = \frac{D_{photons,control}^{SF=0.1}}{D_{ions,control}^{SF=0.1}} \quad (III.4)$$

$$RBE_{+NPs} = \frac{D_{photons;control}^{SF=0.1}}{D_{ions,+NPs}^{SF=0.1}} \quad (III.5)$$

Chapter IV

Results

In this chapter the localization, quantification and biological impact of PtNPs and AuNPs in two human cancer cell lines (HeLa and BxPC-3) are presented. The results of localization of AuNPs in HeLa and BxPC-3 and co-localization with cell organelles are presented in section §1. The quantification of NPs in cells is then presented in section §2. The impact on cell-killing of PtNPs and AuNPs induced in oxic or anoxic conditions using passive scattering and PBS is reported in section 3.1 and section 3.2 respectively. The RBE values obtained for the different radiation qualities are presented in section 3.1.4.

1 Localization of NPs in the cells

The intracellular distribution of PtNPs in HeLa cells was performed by Nanoscale Secondary Ion Mass Spectrometry (Nano-SIMS) analysis during the thesis of Daniela Salado (2013-2016) and it is reviewed in section 1.1. The intracellular distribution of AuNPs labelled with Cy5 in HeLa and BxPC-3 cells and their co-localization with cell organelles were investigated by confocal microscopy (see experimental conditions in chapter III, section 3.1). The results are presented in section 1.2 and section 1.3 respectively.

The concentration of AuNPs-Cy5 and PtNPs used for the experiments was 0.5 mM and the incubation time was 6 h.

1.1 Intracellular distribution of PtNPs in HeLa cells

Nano-SIMS imaging is based on ion microscopy. It is an alternative method to fluorescent microscopy which does not require any fluorescent labelling. In the present study, HeLa cells were incubated with label-free PtNPs (0.5 mM, 6 h) and prepared by cryo-fixation. The morphological cell structure was derived from the detection of CN^- and P^- . Figure IV.1A shows the distribution of carbon and nitrogen containing molecules, an indication of organic matter such as nucleic acids and proteins. Figure IV.1B shows the phosphorus distribution which is used to distinguish the cell nucleus due to its high phosphorus content (DNA). Figure IV.1C shows the distribution of platinum compounds. $^{194}\text{Pt}^-$ was used as isotopic marker of PtNPs.

This analysis clearly demonstrated the presence of platinum inside the cell. In particular, we observe that PtNPs are localized in the cytoplasm (figure IV.1D) and not in the nucleus. This is in agreement with other works performed by the group with platinum complexes [Usami et al., 2008] and other studies with metal-containing NPs [Rima et al., 2013, Jain et al., 2011]. It also shows that PtNPs are preferentially accumulated at cytoplasmic sites found low in phosphorus concentration (region pointed with an arrow), which might be lysosomes or other organelles where no nucleic acids or phospholipids are found. This has been already observed in other works where ^{15}N -labeled peptide vectors co-localize HeLa cytoplasmic zones with low phosphorus concentration [Römer et al., 2006].

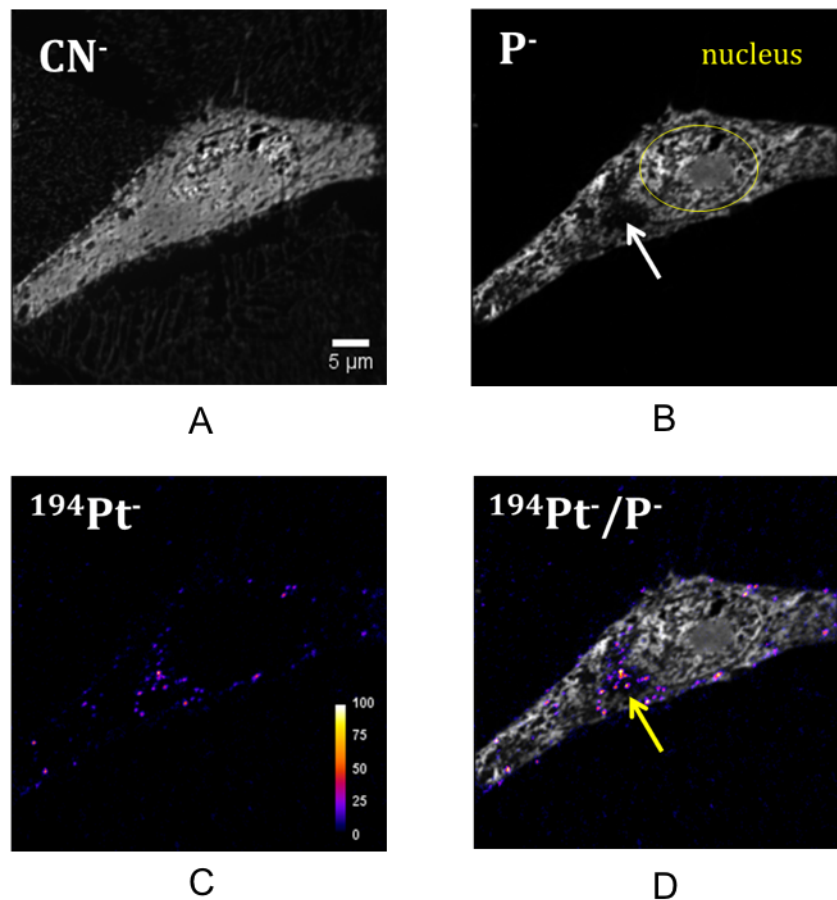


Figure IV.1: Nano-SIMS images of a HeLa cell loaded with PtNPs. Panels (A), (B) and (C) correspond to CN^- , P^- and $^{194}\text{Pt}^-$ respectively. Panel (D) is the merged image of (B) and (C). The arrows show an identified low concentration P^- region in the cell cytoplasm.

1.2 Intracellular distribution of AuNPs in HeLa and BxPC-3 cells

Two representative fluorescence images of HeLa and BxPC-3 cells loaded with AuNPs-Cy5 (0.5 mM, 6 h) are shown in figure IV.2 and figure IV.3 respectively. The cytoplasm, the nucleus and the AuNPs are pointed with arrows.

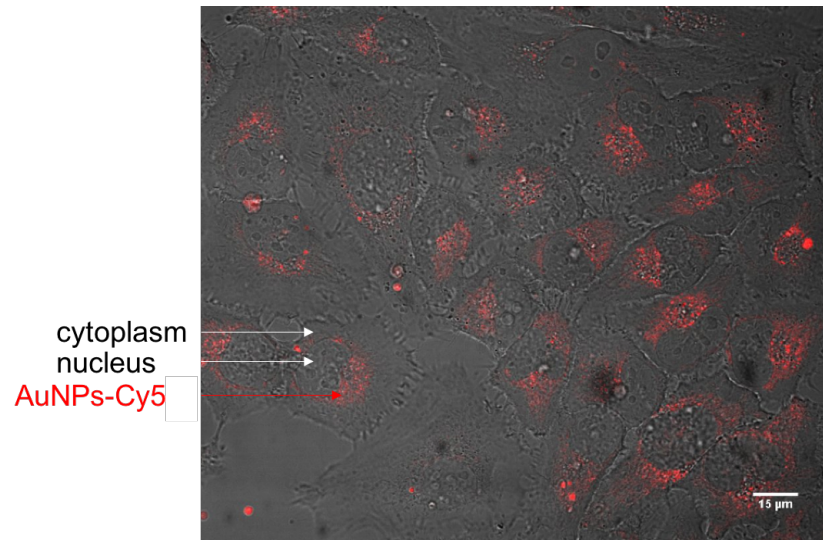


Figure IV.2: Merged image of the transmission and fluorescence images of HeLa cells loaded with AuNPs-Cy5 (red)

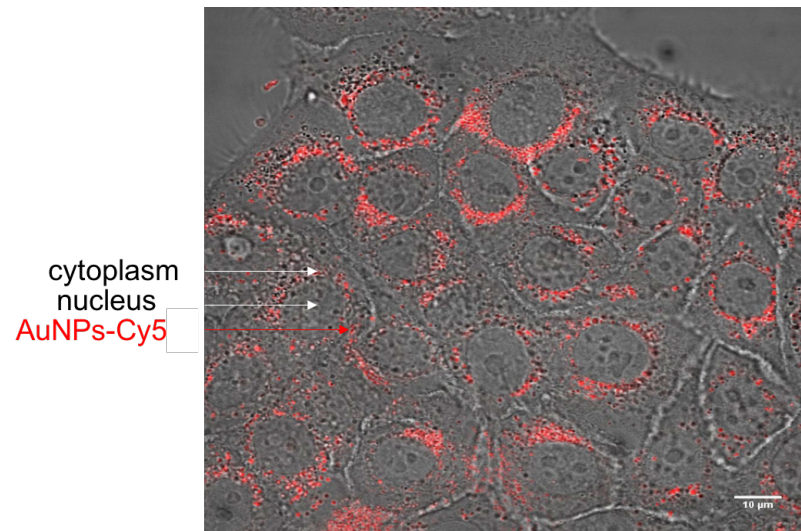


Figure IV.3: Merged image of the transmission and fluorescence images of BxPC-3 cells loaded with AuNPs-Cy5 (red)

We observe that AuNPs sit exclusively in the cytoplasm (figure IV.2 and figure IV.3). They do not penetrate in the nucleus but they are localized in the perinuclear region.

This finding is consistent with other results obtained with 1.4-nm gold NPs labelled with AlexaFluor[®]488 in DU145 (prostate cancer), MDA-MB-231 (breast cancer) and L132 (lung epithelial) cells [Coulter et al., 2012]. The group obtained similar results with 3-nm gadolinium based NPs (AGuix) labelled with Cy5 in U-87-MG (glioblastoma cells) [Štefánčiková et al., 2014], as well as, in Chinese Hamster Ovary (CHO) cells [Porcel et al., 2014]. This results are in agreement with the ones obtained by Daniela Salado with PtNPs in HeLa cells.

1.3 Co-localization of AuNPs with cell organelles in HeLa and BxPC-3 cells

In a second step, the co-localisation of AuNPs-Cy5 with lysosomes and mitochondria was studied in HeLa and BxPC-3 cells.

1.3.1 Co-localisation of AuNPs with lysosomes

Fluorescence images of HeLa cells incubated with the LysoTracker (green) and AuNPs-Cy5 (0.5 mM, 6 h) (red) are presented in figure IV.4A and B respectively. The merged image of (A) and (B) is presented in figure IV.4C. The corresponding fluorescence images of BxPC-3 are presented in figure IV.5A, B and C.

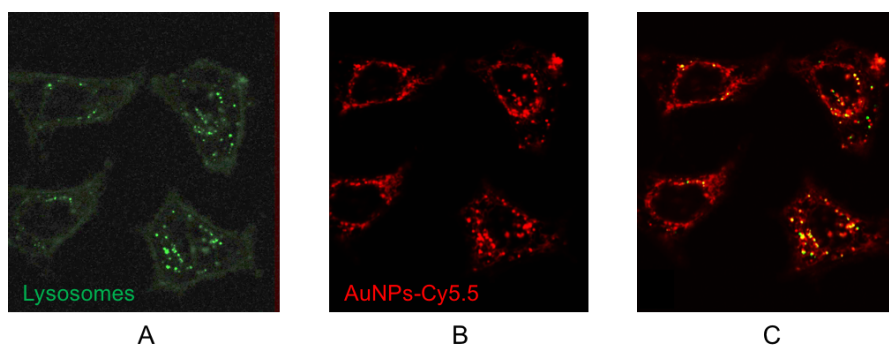


Figure IV.4: Fluorescence image of HeLa cells loaded with LysoTracker (green) (A), AuNPs-Cy5 (0.5 mM, 6 h) (red) (B). (C) is the merged image of (A) and (B) images.

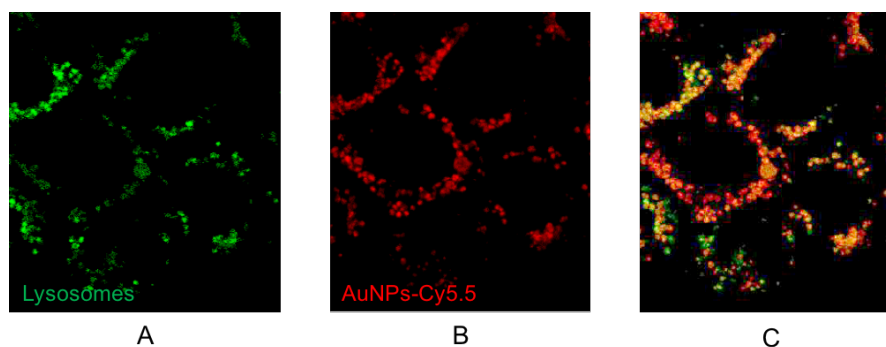


Figure IV.5: Fluorescence image of BxPC-3 cells loaded with Lysotracker-green (A), AuNPs-Cy5 (0.5 mM, 6 h) (red) (B). (C) is the merged image of (A) and (B) images.

The merged image of AuNPs-Cy5 and Lysotracker (green) (figure IV.5C) indicates a co-localisation of AuNPs-Cy5 with lysosomes in BxPC-3 cells but no in HeLa cells.

1.3.2 Co-localisation of AuNPs with mitochondria

Fluorescence images of HeLa cells incubated with the Mitotracker (green) and AuNPs-Cy5 (0.5 mM, 6 h) (red) are presented in figure IV.6A and B respectively. The merge of (A) and (B) images is presented in figure IV.6C. The corresponding fluorescence images of BxPC-3 are presented in figure IV.7A, B and C.

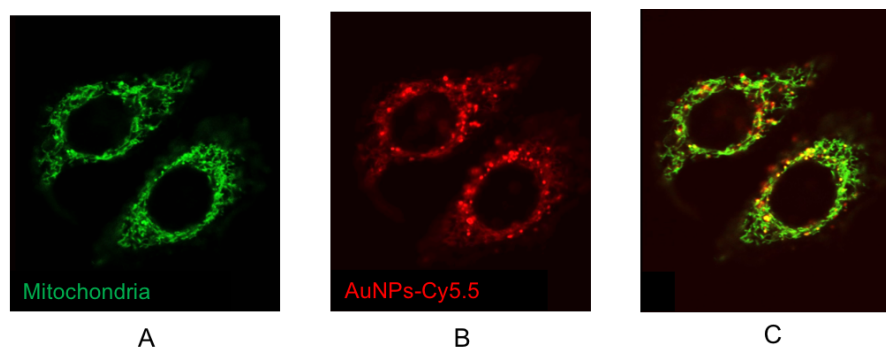


Figure IV.6: Fluorescence image of HeLa cells loaded with Mitotracker (green) (A), AuNPs-Cy5 (0.5 mM, 6 h) (red) (B). (C) is the merged image of (A) and (B) images.

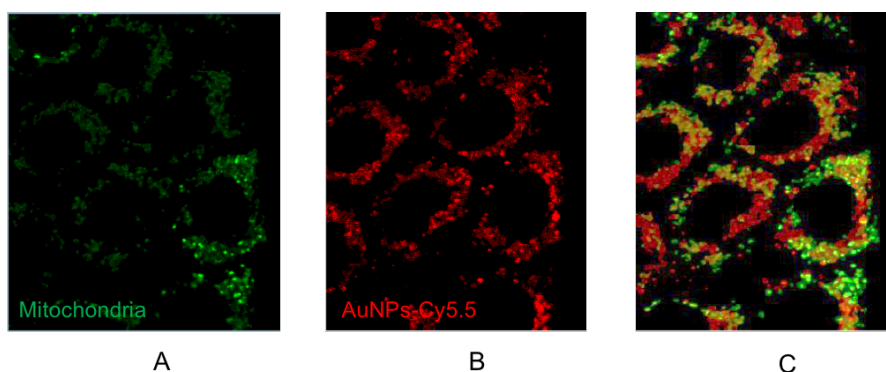


Figure IV.7: Fluorescence image of BxPC-3 cells loaded with Mitotracker (green) (A), AuNPs-Cy5 (0.5 mM, 6 h) (red) (B). (C) is the merged image of (A) and (B) images.

These measurements show that AuNPs are co-localized with mitochondria in the case of HeLa but not in BxPC-3 cells.

1.3.3 Statistical analysis

The Pearson Correlation Coefficient (PCC) [Adler and Parmryd, 2010, Sedgwick, 2012] was used to quantify the co-localization between the AuNPs-Cy5 fluorescence and the lysosomes or mitochondria fluorescence. Coefficient values in between 0.5 and 1 indicate a co-localisation [Zinchuk and Grossenbacher-Zinchuk, 2011]. The average PCC were 0.42 ± 0.04 and 0.56 ± 0.03 for AuNPs-lysosomes in HeLa and BxPC-3 cells respectively. For AuNPs-mitochondria, the average PCC were 0.60 ± 0.06 and 0.34 ± 0.06 for HeLa and BxPC-3 respectively. This analysis demonstrates that AuNPs co-localize with lysosomes in BxPC-3 cells after 6 h of incubation, while no co-localization with mitochondria was observed for the same incubation time. On the contrary, AuNPs co-localize with mitochondria and not lysosomes in HeLa cells. These results show that AuNPs preferential sites are mitochondria and lysosomes in HeLa and BxPC-3 cells respectively, but they may be found elsewhere ($PCC < 0.8$).

Previous works performed by the group have demonstrated the co-localization of GdB-NPs with lysosomes (0.63 ± 0.078) in U-87-MG cells [Štefančíková et al., 2014]. The presence of NPs of different sizes and composition in endosomes and lysosomes was shown by other groups [Bexiga et al., 2011, Lesniak et al., 2010, Shapero et al., 2011, Shi et al., 2010]. The lysosomes are very acidic cellular vesicles that play a role in the transport and the degradation of intracellular and extracellular cargo. A perturbation of

these entities may induce lysosomal pathologies which result in the autophagy of the cells [Neun and Stern, 2011].

Other works have also found nano-agents in mitochondria [Lee et al., 2009, María et al., 2013]. Mitochondria have multiple roles in the metabolism, including the production of adenosine triphosphate (ATP), cell signaling, cell growth, cell cycle progression and cell death [Raimundo, 2014]. Taggart and co-workers demonstrated gold NPs to have a significant impact on mitochondrial function [Taggart et al., 2014].

2 Quantification of PtNPs and AuNPs in cells

The number and mass of PtNPs and AuNPs internalized in HeLa and BxPC-3 cells was quantified. This has been measured by ICP-MS (see experimental conditions in chapter III, section 3.2). The influence of the initial concentration (C_0) and incubation time (t) was investigated. The ICP-MS results for AuNPs and PtNPs incubated in cells in the same conditions than for irradiation experiments are reported in table IV.1.

Cell line	NPs	C_0 (mM)	t (h)	Mass (μg)	pg/cell	NPs/cell (10^5)	NPs/ μm^3
HeLa	Au	0.5	6	0.112 ± 0.001	0.033	2.44	170
		1	6	0.250 ± 0.002	0.064	4.78	333
		1	24	0.387 ± 0.006	0.108	7.99	556
BxPC-3	Au	0.5	6	0.253 ± 0.002	0.146	10.89	757
	Pt	0.5	6	1.635 ± 0.024	0.852	26.28	1830

Table IV.1: Quantification of AuNPs and PtNPs in HeLa cells at different time points and initial concentrations.

A graphical representation of the number of NPs per cell is displayed in figure IV.8.

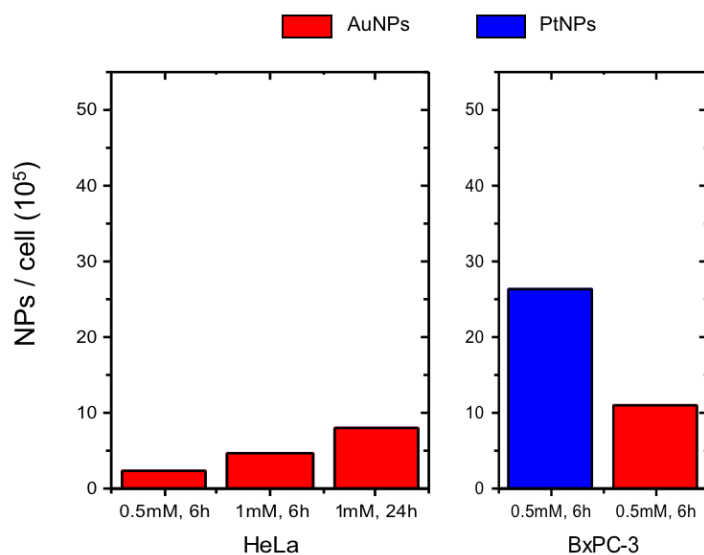


Figure IV.8: AuNPs and PtNPs per cell internalized in HeLa and BxPC-3 cells.

The observations are the following:

- the number of AuNPs in BxPC-3 for 6 h incubation when 0.5 mM is added in the medium is higher than for HeLa.
- the number of AuNPs doubles with the concentration and increases with the incubation time.
- the number of PtNPs is higher than the number of AuNPs (measured in BxPC-3).

This study demonstrates that the internalization of NPs depends on the type of cell line and the NPs composition. This experiment was performed once and other repetitions must be done to perform a statistical analysis of the results.

In summary, AuNPs co-localize with mitochondria (with approx. 2.5×10^5 NPs/cell at 0.5 mM for 6 h incubation) in HeLa. PtNPs penetrate HeLa but the quantity and intracellular localization is unknown. For BxPC-3, AuNPs co-localize with lysosomes (with approx. 1×10^6 NPs/cell at 0.5 mM for 6 h incubation). PtNPs are internalized with approx. 2-3 times more NPs than AuNPs. The co-localization of PtNPs is unknown.

3 Effect of PtNPs and AuNPs on radiation induced cell-killing

The impact of PtNPs and AuNPs on the radiation induced cell-killing was evaluated in HeLa and BxPC-3. Cells free of NPs (control) and cells incubated with NPs were irradiated by carbon-ions, helium-ions or photons in the conditions described in section §4. The effect of NPs was determined by performing clonogenic assays (see chapter III, section 5.1). The efficiency of NPs to amplify radiation effects was quantified using various indicators extracted from the clonogenic assays (see section 5.2). Table IV.2 summarizes the irradiation conditions we used for the experiments.

LET _d (keV/μm)	Passive scattering		PBS		Photons
	Carbon-ions	Helium-ions	Carbon-ions	100	
	50	12	50	100	
HeLa	PtNPs and AuNPs (0.5 mM, 6 h) $pO_2 = 0, 20\%$ section 3.1	—	AuNPs (1 mM, 6 h) $pO_2 = 0, 20\%$ section 3.2.1	AuNPs (1 mM, 6 h) $pO_2 = 0, 20\%$ section 3.2.2	PtNPs/AuNPs (0.5 mM, 6 h)
BxPC-3	PtNPs (0.5 mM, 6 h) $pO_2 = 0, 20\%$ AuNPs (0.5 mM, 6 h) $pO_2 = 0, 0.5, 20\%$ section 3.1.2	PtNPs and AuNPs (0.5 mM, 6 h) $pO_2 = 0, 20\%$ section 3.1.3	—	—	$pO_2 = 0, 20\%$ section 3.1.4

Table IV.2: Outline of section §3 (Effect of PtNPs and AuNPs on radiation induced cell-killing).

3.1 Irradiation experiments using passive scattering delivery system

Carbon- and helium-ion radiation experiments using passive scattering delivery system were performed under the conditions described in section 4.1. In this study, two cell lines (HeLa and BxPC-3) were used. HeLa cells were exposed to carbon-ions (LET_d = 50 keV/μm, SOBP width = 6 cm) in oxic and anoxic conditions. BxPC-3 cells were exposed to carbon-ions at the same LET_d and SOBP width as for HeLa cells in oxic ($pO_2 = 20\%$), hypoxic ($pO_2 = 0.5\%$) and anoxic ($pO_2 = 0\%$) conditions (section 3.1.2). BxPC-3 were also exposed to helium-ion radiation in oxic and anoxic conditions. Additionally, the indirect effect of helium-ion radiation in the presence and absence of AuNPs was investigated in oxic and anoxic conditions (section 3.1.3). Cells were incubated with AuNPs or PtNPs at a concentration of 0.5 mM and an incubation time of 6 h.

The RBE of carbon- and helium-ion radiation using gamma-rays as reference was calculated for the two cell lines and NPs section 3.1.4.

3.1.1 Effect of carbon-ion radiation ($LET_d = 50 \text{ keV}/\mu\text{m}$, SOBP width = 6 cm) in HeLa cells

The oxygen effect of HeLa exposed to carbon-ion radiation in cells free of NPs (control) was evaluated. The resulting survival curves is shown in figure IV.9. The same was investigated in the presence of PtNPs and AuNPs and it is presented in figure IV.10 and figure IV.11 respectively. Irradiation experiments were performed in oxic and anoxic conditions. All the survival curves were fitted with the linear quadratic model.

a) HeLa control cells

Figure IV.9 shows the effect of oxygen on the carbon-ion radiation response of HeLa cells free of NPs.

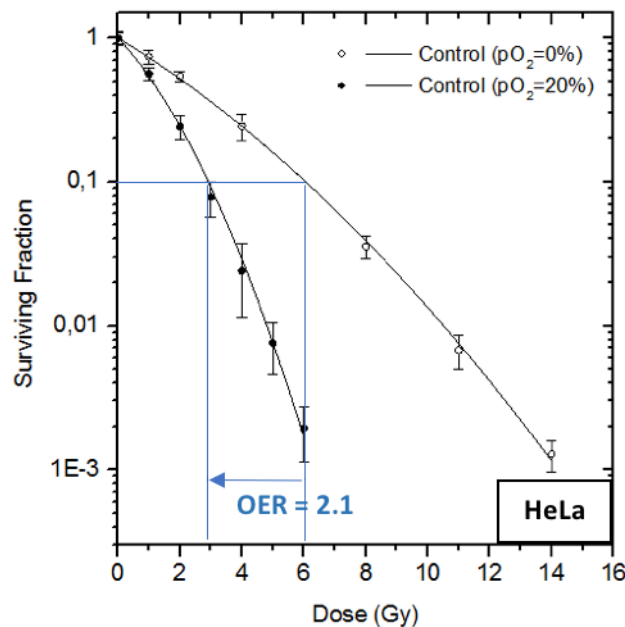


Figure IV.9: Surviving fraction curve for HeLa cells free of NPs (control) irradiated with carbon-ions ($LET_d = 50 \text{ keV}/\mu\text{m}$, SOBP width = 6 cm) in oxic ($pO_2 = 20\%$) and anoxic ($pO_2 = 0\%$) conditions.

3. EFFECT OF PTNPS AND AUNPS ON RADIATION INDUCED CELL-KILLING

The SF curves at a concentration of 20% oxygen is below the SF curve at 0% oxygen, which confirms the radio-sensitizing role of oxygen. We obtained an OER value of 2.1 which is in agreement with other works performed with carbon-ion radiation [Hirayama et al., 2013, Walter Tinganelli, 2012].

b) HeLa cells loaded with PtNPs (0.5 mM, 6 h)

Figure IV.10 shows the effect of PtNPs on the carbon-ion radiation response of HeLa cells in oxic and anoxic conditions.

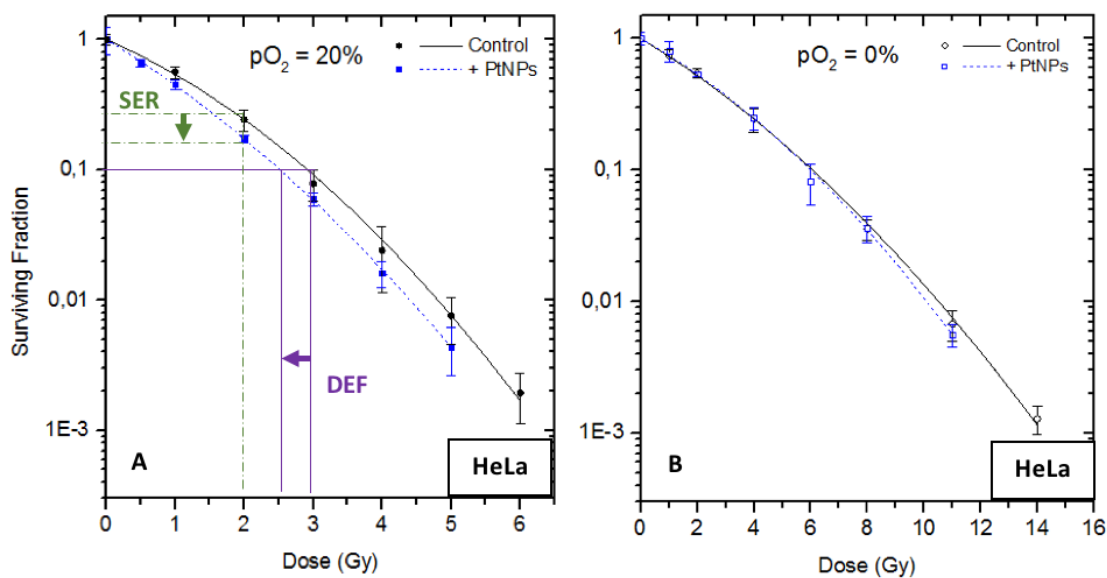


Figure IV.10: Surviving fraction curve for HeLa cells irradiated with carbon-ions ($LET_d = 50 \text{ keV}/\mu\text{m}$, SOBP width = 6 cm) in the presence of PtNPs (0.5 mM, 6 h incubation) in oxic ($pO_2 = 20\%$) (A) and anoxic ($pO_2 = 0\%$) (B) conditions. The green dashed lines and the purple solid lines indicate the surviving fraction at 2 Gy and the dose at 10% of survival respectively.

A radio-enhancement effect in the presence of PtNPs is observed for HeLa cells in oxic condition (figure IV.10A). However, no changes in the radiation response was obtained in anoxic condition (figure IV.10C).

c) HeLa cells loaded with AuNPs (0.5 mM, 6 h)

The same experiment was repeated using AuNPs in the presence and absence of oxygen. The resulting survival curve is shown in figure IV.11.

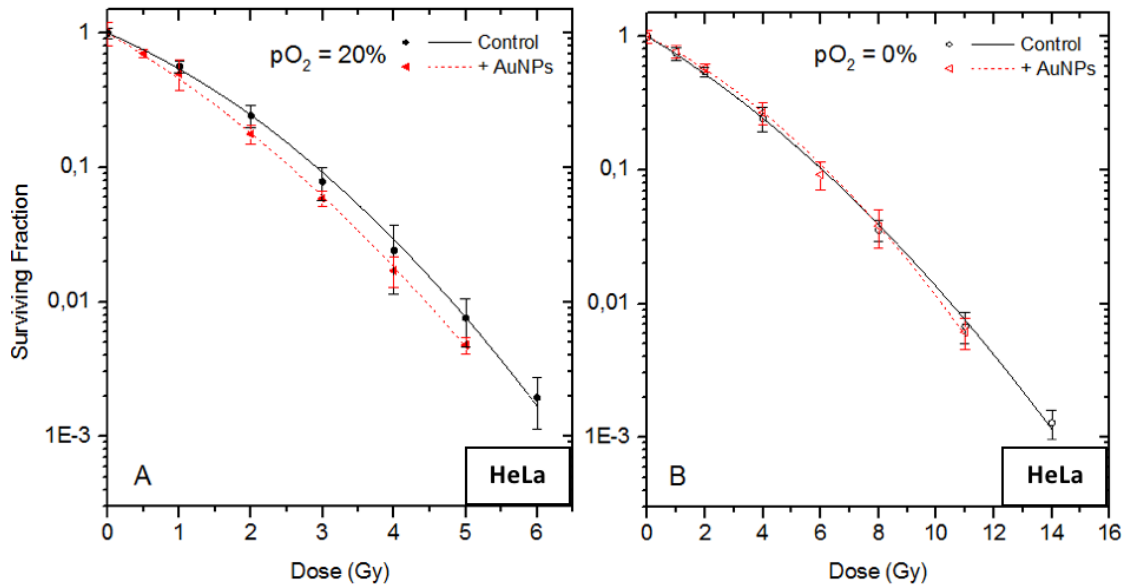


Figure IV.11: Surviving fraction curve for HeLa cells irradiated with carbon-ions ($LET_d = 50 \text{ keV}/\mu\text{m}$, SOBP width = 6 cm) in the presence of AuNPs (0.5 mM, 6 h incubation) in oxic ($pO_2 = 20\%$) (A) and anoxic ($pO_2 = 0\%$) (B) conditions.

Figure IV.11 shows an increase of the radiation effects for HeLa cells loaded with AuNPs in the presence of oxygen. No radio-enhancement was obtained in anoxic condition.

d) Quantitative analysis of radio-induced effects in the presence of NPs

The SF curves were simulated with the linear-quadratic model. The α and β parameters which correspond to different types of lesions (see chapter II, section 1.4.1) were determined. The α and β values are reported in table IV.3.

3. EFFECT OF PTNPS AND AUNPS ON RADIATION INDUCED CELL-KILLING

	Oxic ($pO_2 = 20\%$)		Anoxic ($pO_2 = 0\%$)	
	$\alpha(Gy^{-1})$	$\beta(Gy^{-2})$	$\alpha(Gy^{-1})$	$\beta(Gy^{-2})$
Control	0.53 ± 0.03	0.090 ± 0.008	0.30 ± 0.03	0.013 ± 0.003
PtNPs (0.5 mM, 6 h)	0.72 ± 0.02	0.071 ± 0.006	0.25 ± 0.05	0.020 ± 0.003
AuNPs (0.5 mM, 6 h)	0.74 ± 0.03	0.069 ± 0.005	0.28 ± 0.03	0.017 ± 0.005

Table IV.3: Table of α and β values for HeLa cells irradiated with carbon-ions ($LET_d = 50 \text{ keV}/\mu\text{m}$, SOBP width = 6 cm) in oxic ($pO_2 = 20\%$) and anoxic ($pO_2 = 0\%$) conditions for cells free of NPs (control) and cells loaded with PtNPs or AuNPs (0.5 mM, 6 h incubation).

This analysis (table IV.3) shows that the presence of PtNPs and AuNPs induces an increase of directly lethal lesions and a decrease of sublethal lesions in oxic conditions. However, in anoxic condition no significant difference of α nor β is obtained in the presence of NPs. To summarize, the presence of NPs increases the lethality in oxygenated cells only.

The efficiency of AuNPs and PtNPs to amplify cell death was characterized by the SER and DEF values as defined in chapter III, section 5.2. The values are reported in table IV.4.

	Oxic ($pO_2 = 20\%$)		Anoxic ($pO_2 = 0\%$)	
	SER (D=2Gy) $\pm 5\%$	DEF (SF=10%) ± 0.04	SER(D=2Gy) $\pm 5\%$	DEF (SF=10%) ± 0.04
PtNPs (0.5 mM, 6 h)	27%	1.14	0%	0.98
AuNPs (0.5 mM, 6 h)	29%	1.16	-2%	1.01

Table IV.4: Table of SER and DEF values for HeLa cells irradiated with carbon-ions ($LET_d = 50 \text{ keV}/\mu\text{m}$, SOBP width = 6 cm) in oxic ($pO_2 = 20\%$) and anoxic ($pO_2 = 0\%$) conditions for cells free of NPs (control) and cells loaded with PtNPs or AuNPs (0.5 mM, 6 h incubation).

In oxic conditions, the SER and DEF values for PtNPs and AuNPs are similar ($\sim 28\%$ and ~ 1.15 respectively). In anoxic conditions, the SER and DEF are close to 0% and 1 because no differences were found between the SF curves of control cells and cells loaded with NPs.

Similar experiments were performed with an incubation time of 20 h. The concentrations used for PtNPs and AuNPs were 0.5 mM and 1 mM respectively. The same radiation effect of NPs was found at 6 and 20 h incubation for all the NPs in the presence of oxygen. This shows that the radio-enhancement effect is not proportional to the number of

NPs (AuNPs doubles with the concentration and with the incubation time).

An additional experiment using AuNPs-Gd at a concentration of 1 mM and an incubation time of 20 h was performed in order to evaluate the effect of additional high-Z atoms in the composition of the nanoagents. The same radio-enhancement was found for AuNPs and AuNPs-Gd indicating that the addition of Gd atoms did not increase the radio-enhancement of AuNPs.

3.1.2 Effect of carbon-ion radiation ($LET_d = 50 \text{ keV}/\mu\text{m}$, SOBP width = 6 cm) in BxPC-3 cells

The oxygen effect of BxPC-3 cells exposed to carbon-ion radiation ($LET_d = 50 \text{ keV}/\mu\text{m}$, SOBP width = 6 cm) was evaluated in cells free of NPs and the resulting survival curve is shown in figure IV.12. The SF of irradiated cells in the presence of PtNPs and AuNPs is reported in figure IV.13 and figure IV.14 respectively. Irradiation experiments were performed in oxic and anoxic conditions. In the case of cells loaded with AuNPs, an intermediate oxygen concentration ($pO_2 = 0.5\%$) was also used.

a) BxPC-3 control cells

Figure IV.12 shows the effect of oxygen on the carbon-ion radiation response of BxPC-3 cells free of NPs.

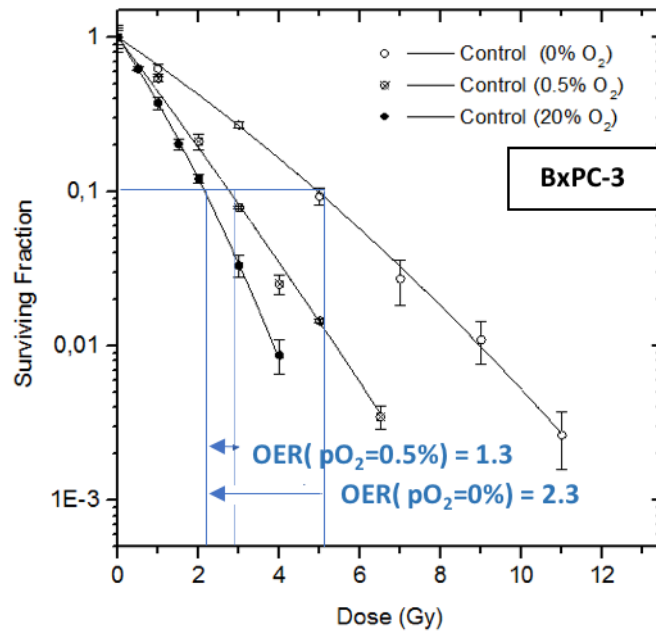


Figure IV.12: Surviving fraction curve for BxPC-3 cells free of NPs (control) irradiated with carbon-ions ($LET_d = 50 \text{ keV}/\mu\text{m}$, SOBP width = 6 cm) in oxic ($pO_2 = 20\%$), hypoxic ($pO_2 = 0.5\%$) and anoxic ($pO_2 = 0\%$) conditions.

As for HeLa, the SF curve for BxPC-3 in oxic is below the SF curve in hypoxic and anoxic conditions. The OER values obtained are 1.3 and 2.3 for hypoxic and anoxic conditions respectively. This shows that a very low amount of oxygen is sufficient to sensitize the radiation effects.

b) BxPC-3 cells loaded with PtNPs (0.5 mM, 6 h)

Figure IV.13 shows the effect of PtNPs on the carbon-ion radiation response of BxPC-3 cells in oxic and anoxic conditions.

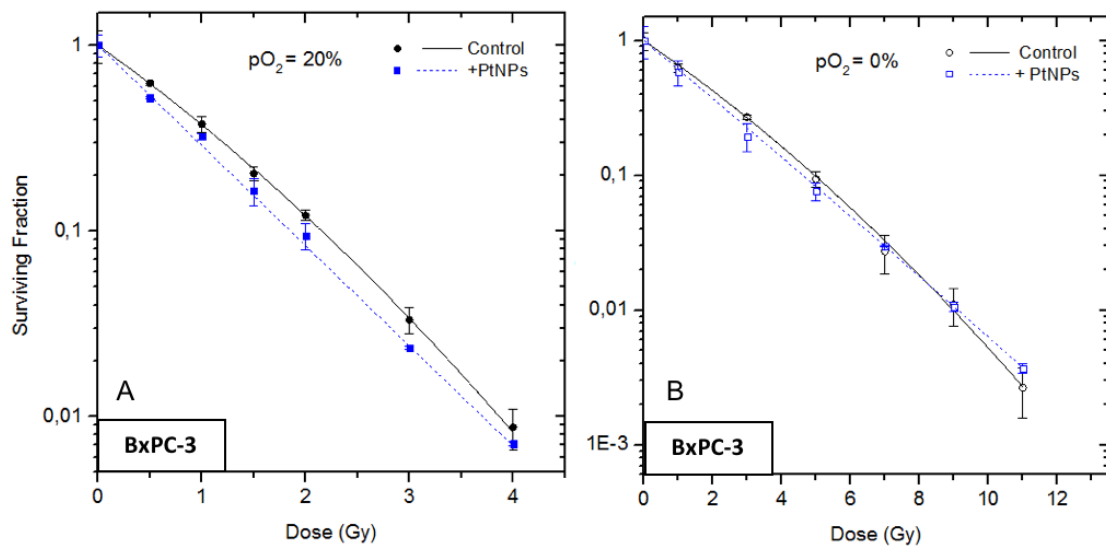


Figure IV.13: Surviving fraction curve for BxPC-3 cells irradiated with carbon-ions ($LET_d = 50 \text{ keV}/\mu\text{m}$, SOBP width = 6 cm) in the presence of PtNPs (0.5 mM, 6 h incubation) in oxic ($pO_2 = 20\%$) (A) and anoxic ($pO_2 = 0\%$) (B) conditions.

An enhancement of carbon-ion radiation effect due to the presence of PtNPs is observed in oxygenated cells (figure IV.13A). However, no significant changes in the radiation response is obtained in anoxic conditions (figure IV.13B).

c) BxPC-3 cells loaded with AuNPs (0.5 mM, 6 h)

The same experiment was repeated using AuNPs but three different oxygen concentrations were used ($pO_2 = 0, 0.5$ and 20%) (figure IV.14).

3. EFFECT OF PTNPS AND AUNPS ON RADIATION INDUCED CELL-KILLING

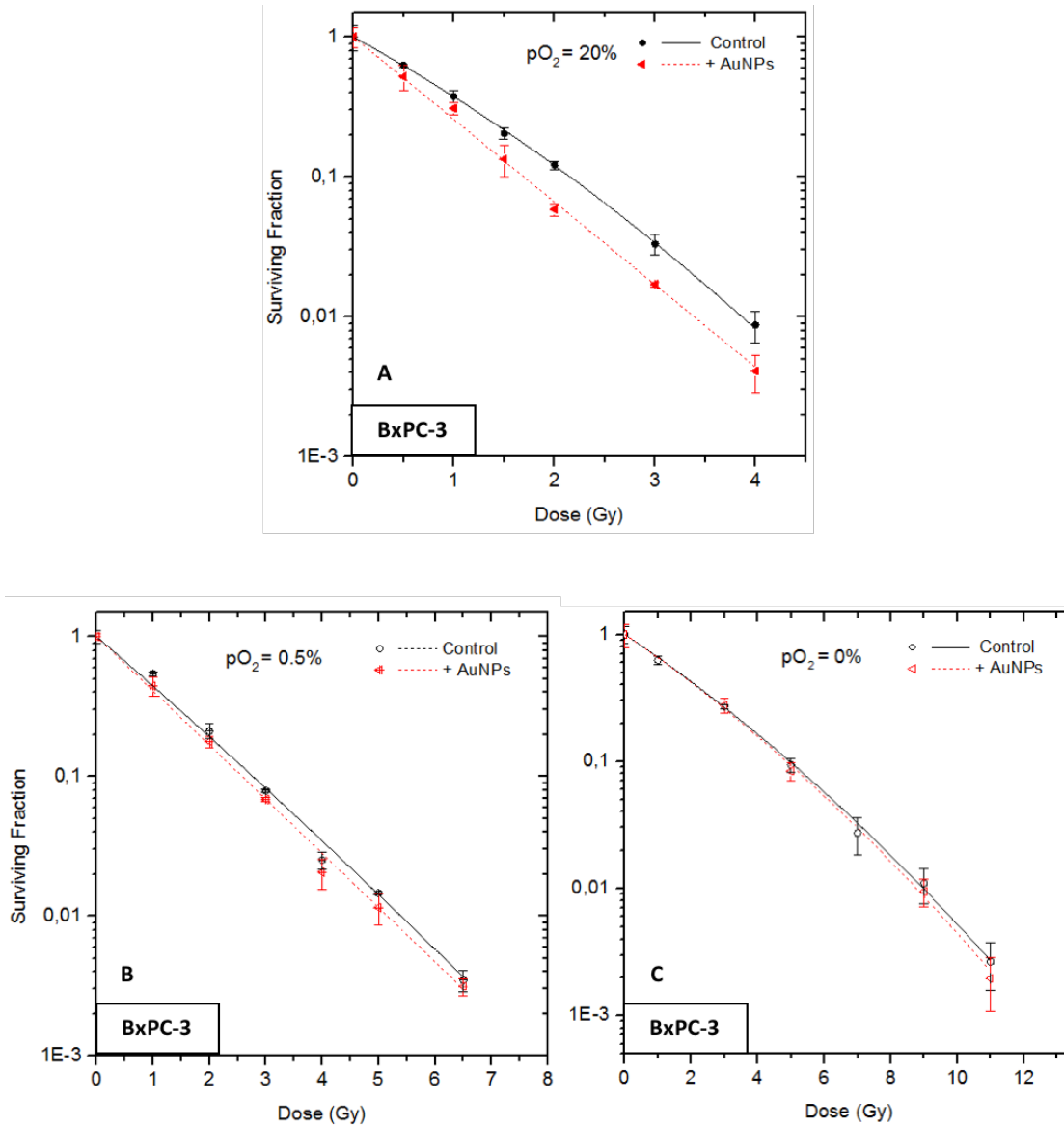


Figure IV.14: Surviving fraction curve for BxPC-3 cells irradiated with carbon-ions ($LET_d = 50 \text{ keV}/\mu\text{m}$, SOBP width = 6 cm) in the presence of AuNPs (0.5 mM, 6 h incubation) in oxalic ($pO_2 = 20\%$) (A), hypoxic ($pO_2 = 0.5\%$) (B) and anoxic ($pO_2 = 0\%$) (C) conditions.

In the presence of AuNPs a significant increase of the radiation effect is observed in oxic condition (figure IV.14A). A lower enhancement is observed in hypoxic conditions (figure IV.14B). No amplification was obtained in the absence of oxygen (figure IV.14C). This result is similar to the one obtained with HeLa. The amplification effect of NPs depends on the presence of oxygen.

d) Quantitative analysis of radio-induced effects in the presence of NPs

The quantification of the type of lesions and the NPs effect was calculated. The values are reported in table IV.5.

	Oxic		Hypoxic		Anoxic	
	$(pO_2 = 20\%)$		$(pO_2 = 0.5\%)$		$(pO_2 = 0\%)$	
	$\alpha(Gy^{-1})$	$\beta(Gy^{-2})$	$\alpha(Gy^{-1})$	$\beta(Gy^{-2})$	$\alpha(Gy^{-1})$	$\beta(Gy^{-2})$
Control	0.91 ± 0.02	0.07 ± 0.01	0.81 ± 0.05	0.01 ± 0.01	0.40 ± 0.02	0.012 ± 0.002
PtNPs (0.5 mM, 6 h)	1.24 ± 0.02	—	—	—	0.50 ± 0.03	—
AuNPs (0.5 mM, 6 h)	1.36 ± 0.01	—	0.89 ± 0.01	—	0.41 ± 0.03	0.013 ± 0.003

Table IV.5: Table of α and β values for BxPC-3 cells irradiated with carbon-ions ($LET_d = 50 \text{ keV}/\mu\text{m}$, SOBP width = 6 cm) in oxic ($pO_2 = 20\%$), hypoxic ($pO_2 = 0, 5\%$) and anoxic ($pO_2 = 0\%$) conditions for cells free of NPs (control) and cells loaded with PtNPs or AuNPs (0.5 mM, 6 h incubation).

The analysis (table IV.5) shows that in oxic conditions the presence of PtNPs and AuNPs induces an increase of α whilst β drops to zero. NPs increases the directly lethal lesions and decreases the sublethal lesions. Using PtNPs, in anoxic condition, a slight increase of lethal damage given by α (0.4 – 0.5) was observed whilst the induction of sublethal decreased (0.012 - 0.0). No enhancement was found for AuNPs in the absence of oxygen. In hypoxic conditions, AuNPs produces non-significant increase of directly lethal damage compared to oxic conditions.

In order to quantify the effects of NPs on cell-killing, the SER and DEF parameters were calculated. The results are presented in table IV.6.

3. EFFECT OF PTNPS AND AUNPS ON RADIATION INDUCED CELL-KILLING

	Oxic ($pO_2 = 20\%$)		Hypoxic ($pO_2 = 0.5\%$)		Anoxic ($pO_2 = 0\%$)	
	SER (D=2Gy) $\pm 5\%$	DEF (SF=10%) ± 0.04	SER (D=2Gy) $\pm 5\%$	DEF (SF=10%) ± 0.04	SER (D=2Gy) $\pm 5\%$	DEF (SF=10%) ± 0.04
PtNPs (0.5 mM, 6 h)	31%	1.16	—	—	14%	1.08
AuNPs (0.5 mM, 6 h)	45%	1.27	12%	1.05	2%	1.02

Table IV.6: Table of SER and DEF values for BxPC-3 cells irradiated with carbon-ions ($LET_d = 50 \text{ keV}/\mu\text{m}$, SOBP width = 6 cm) in oxic ($pO_2 = 20\%$), hypoxic ($pO_2 = 0.5\%$) and anoxic ($pO_2 = 0\%$) conditions for cells free of NPs (control) and cells loaded with PtNPs or AuNPs (0.5 mM, 6 h incubation).

The SER and DEF values found for oxygenated BxP-3 cells in the presence of AuNPs were 45% and 1.27 respectively. This value, higher than the one obtained with HeLa, may be explained by the superior amount of AuNPs internalized in BxPC-3 compared to HeLa (see section §2). It may also be due to the lethality of the perturbation which is maybe more important when it is activated close to lysosomes (BxPC-3) than in mitochondria (HeLa). The SER and DEF values decrease to 12% and 1.07 when the oxygen level of cells was reduced to 0.5%. The radio-enhancement totally vanished in the absence of oxygen. The SER and DEF values for PtNPs are 31% and 1.16 respectively in oxic conditions, and 14% and 1.08 in anoxic condition. As expected from the α and β analysis, the SER and DEF values obtained for AuNPs are greater than for PtNPs although the number of AuNPs is lower than PtNPs.

In summary, the irradiation of HeLa and BxPC-3 by carbon-ions ($LET_d = 50 \text{ keV}/\mu\text{m}$) in the presence of PtNPs and AuNPs leads to similar results: there is a neat amplification of the effects when cells (HeLa and BxPC-3) are irradiated in oxic conditions. There is no amplification in anoxic conditions.

3.1.3 Effect of helium-ion beam ($LET_d = 12 \text{ keV}/\mu\text{m}$, SOBP width = 6 cm) in BxPC-3 cells

In order to compare the oxygen effect on different ion radiations and LET_d s, BxPC-3 cells were irradiated with helium-ions ($LET_d = 12 \text{ keV}/\mu\text{m}$, SOBP width = 6 cm). The LET_d used for helium-ion radiation was lower than the one used for carbon-ion radiation ($LET_d = 50 \text{ keV}/\mu\text{m}$). The resulting survival curve for control cells is presented

in figure IV.15. The SF obtained in the presence of PtNPs and AuNPs is presented in figure IV.16 and IV.17 respectively. Irradiation experiments were done in oxic and anoxic conditions. All the survival curves were fitted to the linear quadratic model.

a) BxPC-3 control cells

Figure IV.15 shows the effect of oxygen in helium-ion radiation response of BxPC-3 cells free of NPs.

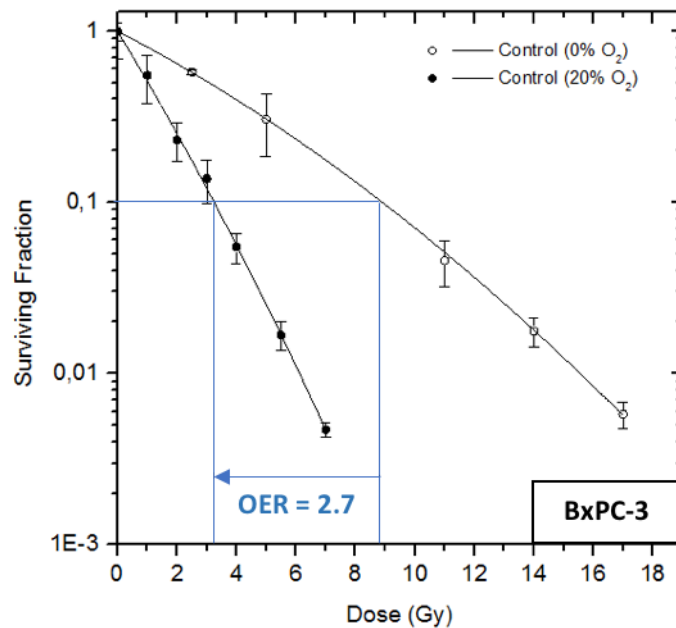


Figure IV.15: Surviving fraction curve for BxPC-3 cells free of NPs (control) irradiated with helium-ions ($LET_d = 12 \text{ keV}/\mu\text{m}$, SOBP width = 6 cm) in oxic ($pO_2 = 20\%$) and anoxic ($pO_2 = 0\%$) conditions.

The OER for BxPC-3 irradiated with helium-ions is higher than for carbon-ions (2.7 and 2.3 respectively). The lethality of the radiation protocol with helium-ions is more oxygen dependent than with carbon-ion radiation. This is because ionization track of carbon-ion beams is more dense and the induced damage more complex. Thus the lethality of the carbon-ions radiation depends less on the "fixation" of organic radicals by O₂ than in the case of helium-ion exposure.

Our results are in agreement with Monte Carlo simulation studies. These studies showed that the OER ($pO_2 = 0\%$) is almost 3 up to $LET_d = 40 \text{ keV}/\mu\text{m}$ and then, the OER

3. EFFECT OF PTNPS AND AUNPS ON RADIATION INDUCED CELL-KILLING

decreases sharply with increasing LET [Scifoni et al., 2013].

b) BxPC-3 cells loaded with PtNPs (0.5 mM, 6 h)

Figure IV.16 shows the effect of PtNPs on the helium-ion radiation response of BxPC-3 cells in oxic and anoxic conditions.

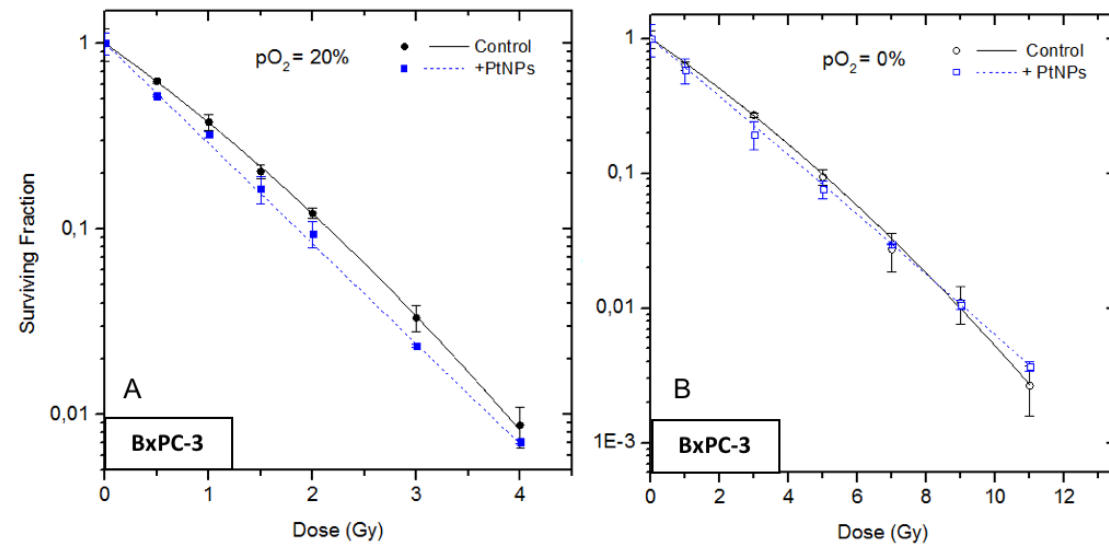


Figure IV.16: Surviving fraction curve for BxPC-3 cells irradiated with helium-ions ($LET_d = 12 \text{ keV}/\mu\text{m}$, SOBP width = 6 cm) in the presence of PtNPs (0.5 mM, 6 h incubation) in oxic ($pO_2 = 20\%$) (A) and anoxic ($pO_2 = 0\%$) (B) conditions.

A radio-enhancement effect in the presence of PtNPs is observed for BxP-3 cells in oxic condition. As for carbon-ion radiation, no effect in the presence of PtNPs is found in anoxic condition.

c) BxPC-3 cells loaded with AuNPs (0.5 mM, 6 h)

BxPC-3 cells were also irradiated with helium-ions in the presence of AuNPs in oxic and anoxic conditions. The resulting survival curve is shown in figure IV.17.

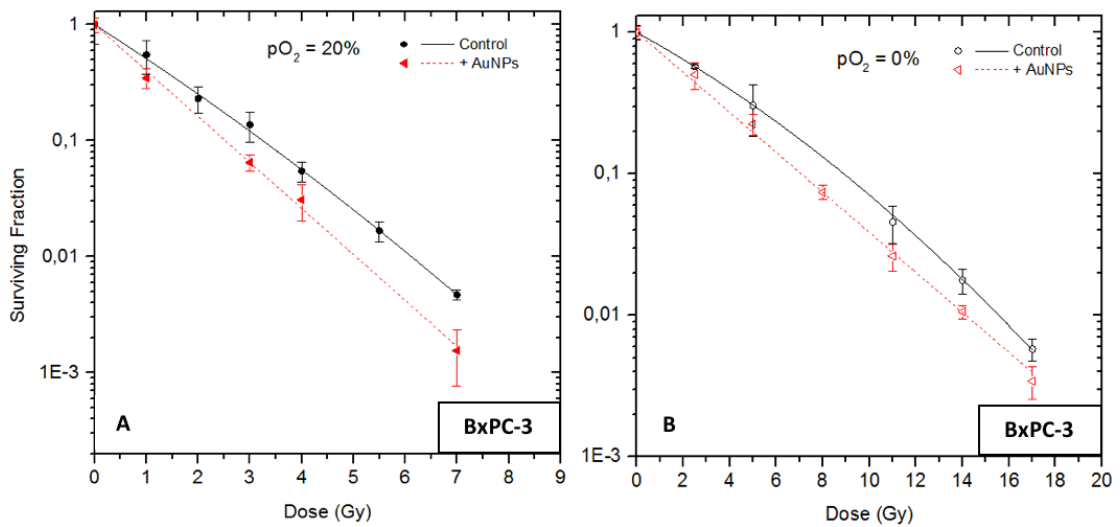


Figure IV.17: Surviving fraction curve for BxPC-3 cells irradiated with helium-ions ($LET_d = 12 \text{ keV}/\mu\text{m}$, SOBP width = 6 cm) in the presence of AuNPs (0.5 mM, 6 h incubation) in oxic ($pO_2 = 20\%$) (A) and anoxic ($pO_2 = 0\%$) (B) conditions.

AuNPs enhance the effect of helium-ion radiation in the presence but also in the absence of oxygen. This last result is different from the findings obtained with carbon-ions radiation ($LET_d = 50 \text{ keV}/\mu\text{m}$) in anoxic conditions (figure IV.17).

In summary, with helium-ion radiation, the two NPs influence differently the radiation effects: PtNPs has little effects (in oxic and anoxic conditions) whilst AuNPs amplify helium-ion radiation with or without O_2 . It indicates that AuNPs amplifies complex damages in the cytoplasm that are directly lethal for the cells.

d) Quantitative analysis of radio-induced effects in the presence of NPs

In order to study the different types of lesions, the SF curves were simulated with the linear-quadratic model and the α and β parameters were determined. The values are reported in table IV.7.

3. EFFECT OF PTNPS AND AUNPS ON RADIATION INDUCED CELL-KILLING

	Oxic ($pO_2 = 20\%$)		Anoxic ($pO_2 = 0\%$)	
	$\alpha(Gy^{-1})$	$\beta(Gy^{-2})$	$\alpha(Gy^{-1})$	$\beta(Gy^{-2})$
Control	0.66 ± 0.02	0.015 ± 0.003	0.208 ± 0.003	0.013 ± 0.003
PtNPs (0.5 mM, 6 h)	0.67 ± 0.03	0.026 ± 0.005	0.175 ± 0.010	0.020 ± 0.002
AuNPs (0.5 mM, 6 h)	0.91 ± 0.02	—	0.326 ± 0.003	—

Table IV.7: Table of α and β values for BxPC-3 cells irradiated with helium-ions ($LET_d = 12 \text{ keV}/\mu\text{m}$, SOBP width = 6 cm) in oxic ($pO_2 = 20\%$) and anoxic ($pO_2 = 20\%$) conditions for cells free of NPs (control) and cells loaded with PtNPs or AuNPs (0.5 mM, 6 h incubation).

The quantitative analysis presented in table IV.7 shows that the presence of PtNPs increases the sublethal damage caused by radiation in oxic condition. Therefore the radio-enhancement due to PtNPs increases with increasing dose of radiation. In the absence of oxygen, a small change in the shape of the survival curve is observed. No significant difference of α nor β is obtained in the presence of PtNPs. The presence of AuNPs induces a strong increase of the lethal damage and a decrease of the sublethal damage ($\beta = 0$) in the two oxygen conditions.

The efficiency of NPs to amplify cell death was characterized by calculating the SER and DEF. The values are reported in table IV.8.

	Oxic ($pO_2 = 20\%$)		Anoxic ($pO_2 = 0\%$)	
	SER (D=2Gy) $\pm 5\%$	DEF (SF=10%) ± 0.04	SER(D=2Gy) $\pm 5\%$	DEF (SF=10%) ± 0.04
PtNPs (0.5 mM, 6 h)	6%	1.06	0%	0.96
AuNPs (0.5 mM, 6 h)	36%	1.29	19%	1.26

Table IV.8: Table of SER and DEF values for BxPC-3 cells irradiated with helium-ions ($LET_d = 12 \text{ keV}/\mu\text{m}$, SOBP width = 6 cm) in oxic ($pO_2 = 20\%$) and anoxic ($pO_2 = 0\%$) conditions for cells free of NPs (control) and cells loaded with PtNPs or AuNPs (0.5 mM, 6 h incubation).

At SF = 10% and D = 2 Gy, no significant effect was observed for PtNPs. However, we obtained a DEF (SF = 1%) of 36% and a SER (6 Gy) of 1.09 in oxic conditions.

A SER (D = 2 Gy) of 36% and 19 % were found for AuNPs in oxic and anoxic conditions respectively. The DEF at SF = 10% is similar for the two oxygen concentrations (~ 1.28).

In summary, the results obtained with BxPC-3 irradiated with helium-ions are very different from the results observed with carbon-ions ($LET_d = 50 \text{ keV}/\mu\text{m}$). In addition, the

effects with PtNPs and AuNPs diverge strongly. Stated differently, with helium-ion radiation, the effects are strongly NPs-dependent but not oxygen-dependent. This indicates that AuNPs induce complex damage directly lethal (even with no O_2 fixation).

e) Quantification of indirect effects

The contribution of indirect action mediated by OH radicals to radiation induced cell-killing was evaluated for helium-ion radiation using the radical scavenger DMSO. DMSO at a concentration of 0.5 mM was added 1 h before the irradiation. No cytotoxicity was observed at this DMSO concentration. BxPC-3 cells in the presence of AuNPs (0.5 mM, 6 h) were used. The experiment was performed in oxic and anoxic conditions. The surviving fraction curves for cells free of NPs and cells loaded with NPs with/without DMSO are presented in figure IV.18.

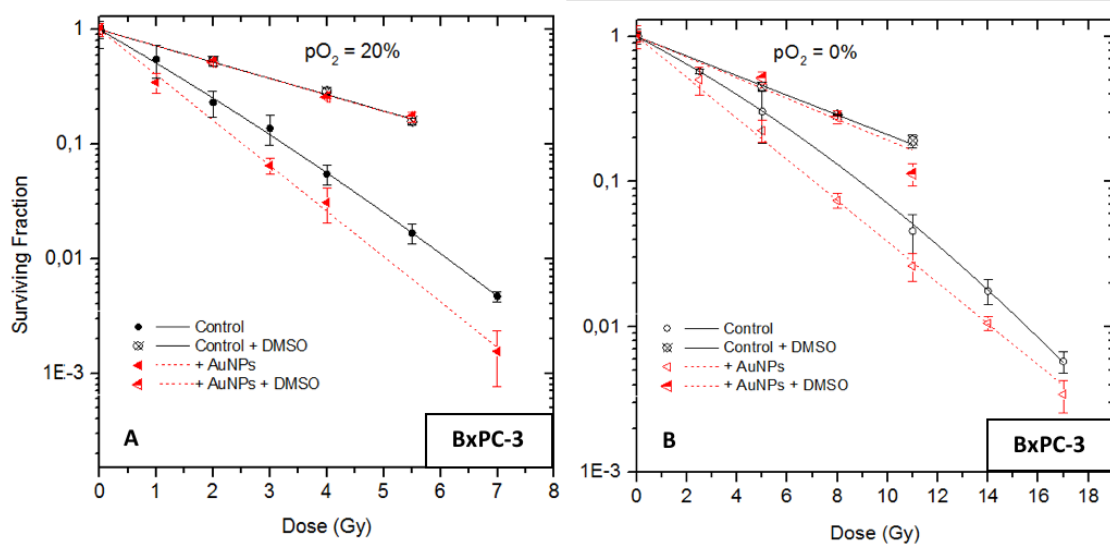


Figure IV.18: Surviving fraction curve for BxPC-3 cells irradiated with helium-ions ($LET_d = 12 \text{ keV}/\mu\text{m}$, SOBP width = 6 cm) in the presence and absence of DMSO (0.5 mM, 1 h): control cells and cells loaded with AuNPs (0.5 mM, 6 h incubation) in oxic ($pO_2 = 20\%$) (A) and anoxic ($pO_2 = 0\%$) (B) conditions.

In the control, SF increases from 0.2 to 0.6 with OH scavenged (at 2 Gy). Approximately 50% of the radiation effects are due to direct effects and 50% to indirect effects. In the presence of NPs, the radio-enhancement effect is totally scavenged showing that it is fully $\bullet\text{OH}$ -mediated even though is not oxygen dependent.

3.1.4 RBE of ion radiation

In order to calculate the RBE of ion treatment with and without NPs, we performed experiments with photon radiation in oxic conditions. The RBE assess the biological effectiveness of each treatment. The RBE was calculated for control cells and cells loaded with NPs irradiated under carbon- and helium-ions. Figure IV.19 shows the surviving curves for HeLa and BxPC-3 cells (free of NPs) irradiated with photon, carbon-ion and helium-ion radiation. The vertical lines indicate the doses at SF = 10% that were used to calculate the RBE of carbon-ion ($LET_d = 50 \text{ keV}/\mu\text{m}$, SOBP width = 6 cm) and helium-ion ($LET_d = 12 \text{ keV}/\mu\text{m}$, SOBP width = 6 cm) radiation.

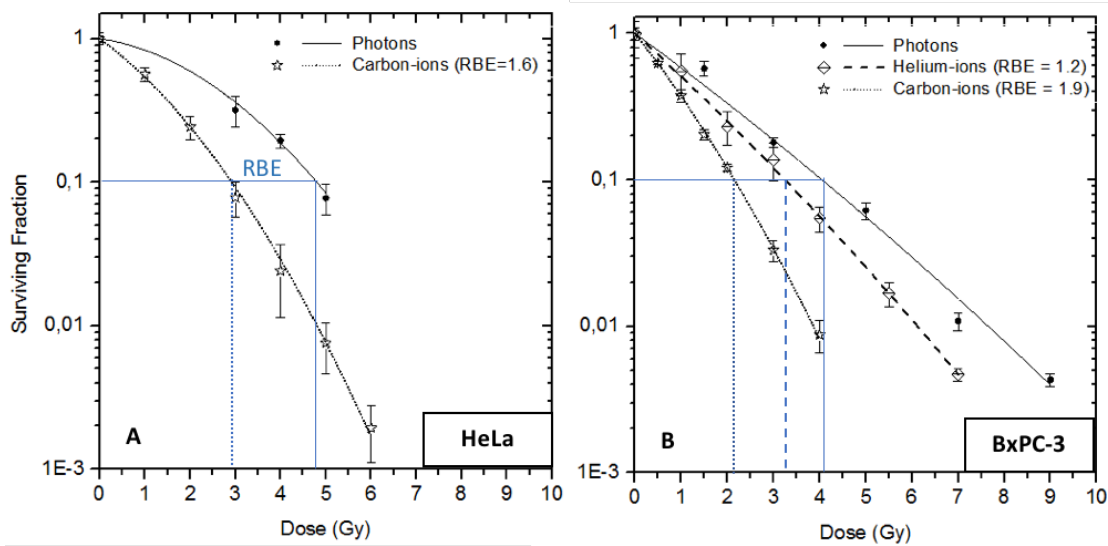


Figure IV.19: Surviving fraction curve for HeLa (A) and BxPC-3 (B) cells free of NPs (control) irradiated with photon, carbon-ion ($LET_d = 50 \text{ keV}/\mu\text{m}$, SOBP width = 6 cm) and helium-ion ($LET_d = 12 \text{ keV}/\mu\text{m}$, SOBP width = 6 cm) radiation.

The RBE results are reported in table IV.9.

	RBE (SF=10%) ± 0.1		
	Carbon-ions		Helium-Ions
	HeLa	BxPC-3	BxPC-3
Control	1.6	1.9	1.2
PtNPs (0.5 mM, 6 h)	1.9	2.2	1.3
AuNPs (0.5 mM, 6 h)	1.9	2.4	1.6

Table IV.9: RBE of carbon- and helium-ions for BxPC-3 and HeLa: cells free of NPs (control) and cells loaded with PtNPs or AuNPs (0.5 mM, 6 h incubation).

For HeLa cells, PtNPs and AuNPs increase by 15% the RBE of carbon-ions. For BxPC-3, the increase of carbon-ion and helium-ions RBE was higher with AuNPs (26%) than with PtNPs (16%). This analysis is summarized in figure IV.20.

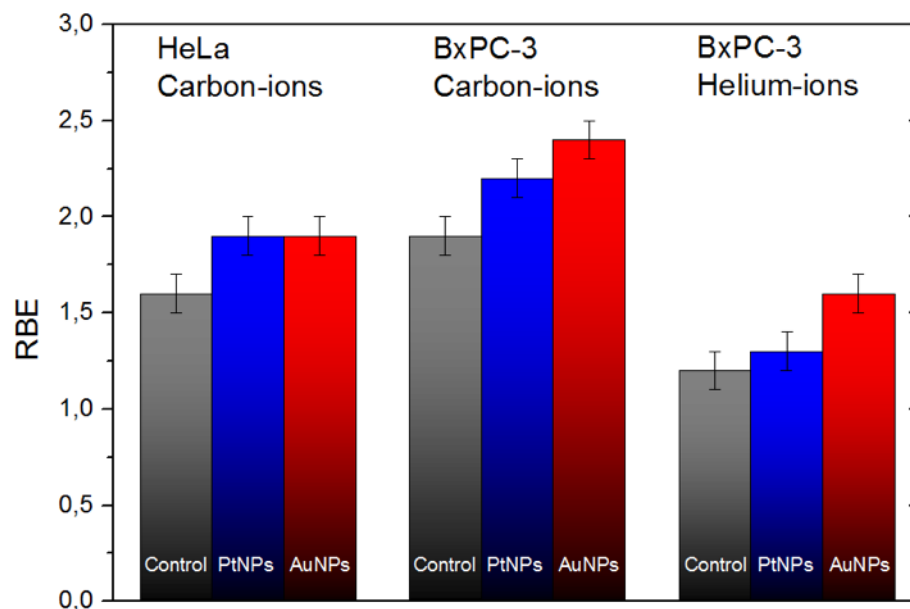


Figure IV.20: RBE of carbon- and helium-ions for BxPC-3 and HeLa: cells free of NPs (control) and cells loaded with PtNPs or AuNPs (0.5 mM, 6 h incubation).

3.2 Irradiation experiments using PBS delivery system

Carbon-ion radiation experiments using PBS delivery system were performed under the conditions described in chapter III, section 4.2. The effect of AuNPs was investigated in HeLa cells in oxic and anoxic conditions. Cells were incubated with AuNPs at a concentration of 1 mM and an incubation time of 6 h. Two LET_ds were used, 50 and

100 keV/ μm . The indirect effect of carbon-ion radiation ($\text{LET}_d = 100 \text{ keV}/\mu\text{m}$) in the presence and absence of AuNPs (1 mM, 6 h) was studied in oxic condition.

3.2.1 Effect of carbon-ion beam ($\text{LET}_d = 50 \text{ keV}/\mu\text{m}$, PBS) in HeLa cells

The oxygen effect of HeLa exposed to carbon-ion radiation ($\text{LET}_d = 50 \text{ keV}/\mu\text{m}$, PBS) is evaluated in cells free of NPs (control) (figure IV.21). Then, the SF obtained in the presence of AuNPs is reported in figure IV.22. Irradiation experiments were done in oxic ($pO_2 = 20\%$) and anoxic ($pO_2 = 0\%$) conditions. All the survival curves were fitted with the linear quadratic model.

a) HeLa control cells

Figure IV.21 shows the effect of oxygen on the carbon-ion radiation ($\text{LET}_d = 50 \text{ keV}/\mu\text{m}$, PBS) response of HeLa cells free of NPs.

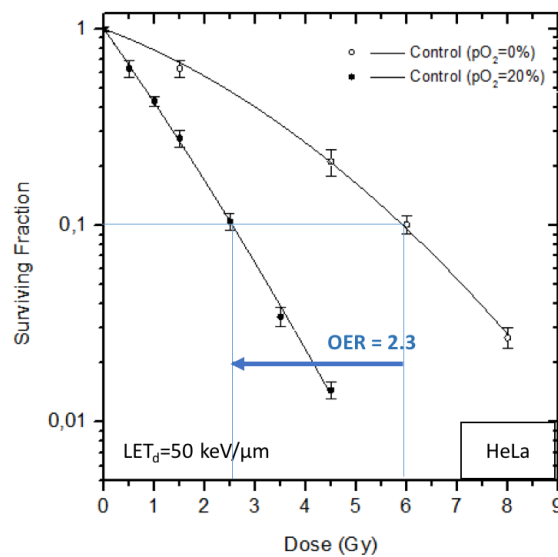


Figure IV.21: Surviving fraction curve for HeLa cells free of NPs (control) irradiated with carbon-ions ($\text{LET}_d = 50 \text{ keV}/\mu\text{m}$, PBS) in oxic ($pO_2 = 20\%$) and anoxic ($pO_2 = 0\%$) conditions.

The OER value was 2.3 which is slightly higher than the one obtained using passive scattering at the same LET (2.1).

b) HeLa cells loaded with AuNPs (1 mM, 6 h)

The effect of AuNPs on the carbon-ion response of HeLa cells in oxic and anoxic conditions is reported in figure IV.22.

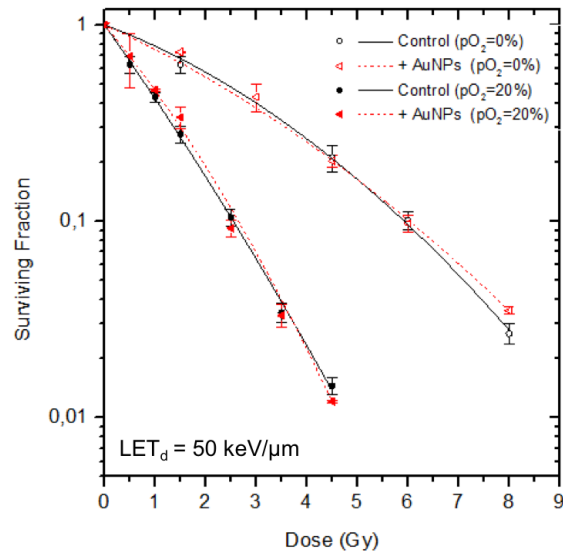


Figure IV.22: Surviving fraction curve for HeLa cells irradiated with carbon-ions ($LET_d = 50 \text{ keV}/\mu\text{m}$, PBS) in the presence of AuNPs (1 mM, 6 h incubation) in oxic ($pO_2 = 20\%$) and anoxic ($pO_2 = 0\%$) conditions.

Surprisingly, no changes in the radiation response were obtained in the presence of AuNPs neither in oxic nor anoxic conditions.

c) Quantitative analysis of radio-induced effects in the presence of NPs

The SF curves were simulated with the linear-quadratic model and the α and β parameters were determined. The values are reported in table IV.10.

3. EFFECT OF PTNPS AND AUNPS ON RADIATION INDUCED CELL-KILLING

	Oxic ($pO_2 = 20\%$)		Anoxic ($pO_2 = 0\%$)	
	$\alpha(Gy^{-1})$	$\beta(Gy^{-2})$	$\alpha(Gy^{-1})$	$\beta(Gy^{-2})$
Control	0.72 ± 0.07	0.210 ± 0.025	0.31 ± 0.02	0.096 ± 0.007
AuNPs (1 mM, 6 h)	0.71 ± 0.03	0.030 ± 0.010	0.27 ± 0.03	0.019 ± 0.002

Table IV.10: Table of α and β values for HeLa cells irradiated with carbon-ions ($LET_d = 50 \text{ keV}/\mu\text{m}$, PBS) in oxic ($pO_2 = 20\%$) and anoxic ($pO_2 = 0\%$) conditions for cells free of NPs (control) and cells loaded with AuNPs (1 mM, 6 h incubation).

This analysis (table IV.10) confirms that there is no radio-enhancement of NPs at this radiation quality.

3.2.2 Effect of carbon-ion beam ($LET_d = 100 \text{ keV}/\mu\text{m}$, PBS) in HeLa cells

In order to compare the oxygen effect of different LET_d , HeLa cells were also irradiated with carbon-ions at $LET_d = 100 \text{ keV}/\mu\text{m}$. The resulting survival curve for control cells is presented in figure IV.23. The SF obtained in the presence of AuNPs (1 mM, 6 h) is presented in figure IV.24. Irradiation experiments were done in oxic ($pO_2 = 20\%$) and anoxic ($pO_2 = 0\%$) conditions. All the survival curves were fitted to the linear quadratic model.

a) HeLa control cells

Figure IV.23 shows the effect of oxygen on the carbon-ion radiation ($LET_d = 100 \text{ keV}/\mu\text{m}$, PBS) response of BxPC-3 cells free of NPs.

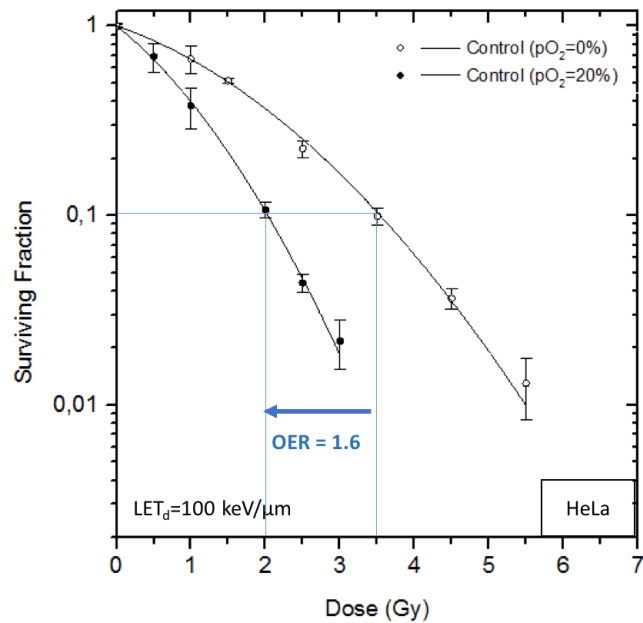


Figure IV.23: Surviving fraction curve for HeLa cells free of NPs (control) irradiated with carbon-ions ($LET_d = 100 \text{ keV}/\mu\text{m}$, PBS) in oxic ($pO_2 = 20\%$) and anoxic ($pO_2 = 0\%$) conditions.

The OER obtained was 1.6. The OER decreased drastically with increasing LET (OER = 2.3 at $LET_d = 50 \text{ keV}/\mu\text{m}$).

b) HeLa cells loaded with AuNPs (1 mM, 6 h)

HeLa cells were exposed to carbon-ions in the presence of AuNPs in oxic and anoxic conditions. The resulting survival curve is shown in figure IV.24.

3. EFFECT OF PTNPS AND AUNPS ON RADIATION INDUCED CELL-KILLING

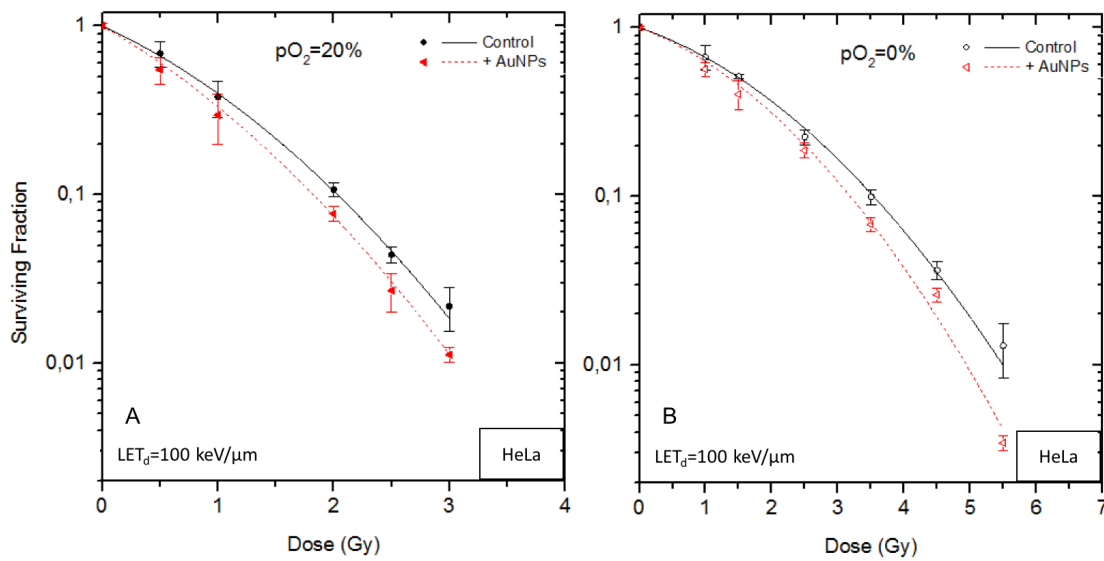


Figure IV.24: Surviving fraction curve for HeLa cells irradiated with carbon-ions ($LET_d = 100 \text{ keV}/\mu\text{m}$, PBS) in the presence of AuNPs (1 mM, 6 h incubation) in oxic ($pO_2 = 20\%$) (A) and anoxic ($pO_2 = 0\%$) conditions (B).

AuNPs enhance the effect of carbon-radiation in the presence and also in the absence of oxygen at $LET_d = 100 \text{ keV}/\mu\text{m}$. This results are similar at the ones obtained with BxPC-3 cells exposed to helium-ions. It indicates that AuNPs amplifies complex damages in the cytoplasm that are directly lethal.

c) Quantitative analysis of radio-induced effects in the presence of NPs

In order to study the different types of lesions, the SF curves were simulated with the linear-quadratic model and the α and β parameters were determined. The values are reported in table IV.11.

	Oxic ($pO_2 = 20\%$)		Anoxic ($pO_2 = 0\%$)	
	$\alpha(Gy^{-1})$	$\beta(Gy^{-2})$	$\alpha(Gy^{-1})$	$\beta(Gy^{-2})$
Control	0.84 ± 0.03	0.025 ± 0.008	0.22 ± 0.03	0.028 ± 0.004
AuNPs (0.5 mM, 6 h)	0.91 ± 0.06	0.060 ± 0.007	0.34 ± 0.09	0.119 ± 0.020

Table IV.11: Table of α and β values for HeLa cells irradiated with carbon-ions ($LET_d = 100 \text{ keV}/\mu\text{m}$, PBS) in oxic ($pO_2 = 20\%$) and anoxic ($pO_2 = 0\%$) conditions for cells free of NPs (control) and cells loaded with AuNPs (1 mM, 6 h incubation).

The quantitative analysis presented in table IV.11 shows that the presence of AuNPs increases both the lethal and sublethal damage caused by radiation in oxic and anoxic conditions.

The efficiency of NPs to amplify cell death was characterized by calculating the SER and DEF values. These values are reported in table IV.12.

	Oxic ($pO_2 = 20\%$)		Anoxic ($pO_2 = 0\%$)	
	SER (D=2Gy) $\pm 5\%$	DEF (SF=10%) ± 0.04	SER(D=2Gy) $\pm 5\%$	DEF (SF=10%) ± 0.04
AuNPs (1 mM, 6 h)	30%	1.12	15%	1.11

Table IV.12: Table of SER and DEF values for HeLa cells irradiated with carbon-ions ($LET_d = 100 \text{ keV}/\mu\text{m}$, PBS) in oxic ($pO_2 = 20\%$) and anoxic ($pO_2 = 0\%$) conditions for cells free of NPs (control) and cells loaded with AuNPs (1 mM, 6 h incubation).

In the presence of oxygen, we obtained a DEF and a SER of 29% and 1.12 respectively. In anoxic condition, the same DEF was obtained, but lower SER (15%).

d) Quantification of indirect effects

The contribution of indirect action mediated by OH radicals to radiation cell-killing was evaluated for carbon-ion radiation using the radical scavenger DMSO. DMSO at a concentration of 1 mM was added 1 h before the irradiation. HeLa cells were incubated with AuNPs (1 mM, 6 h). No cytotoxicity was observed at this DMSO concentration. The experiment was performed in oxic conditions only. The surviving fraction curves for cells free of NPs and cells loaded with NPs with/without DMSO are presented in figure IV.25.

3. EFFECT OF PTNPS AND AUNPS ON RADIATION INDUCED CELL-KILLING

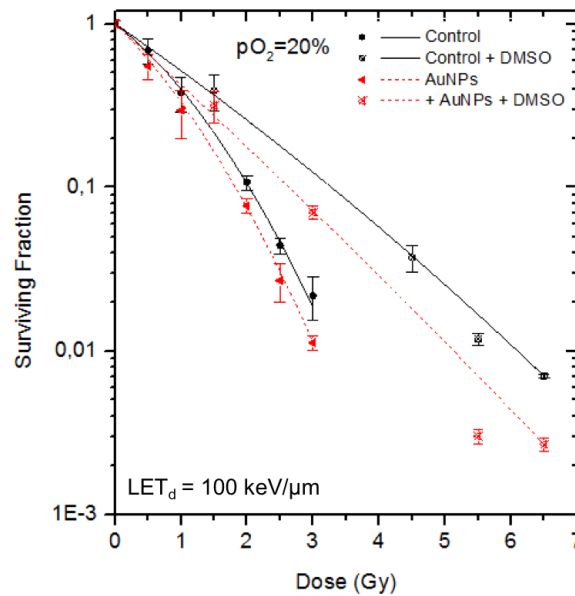


Figure IV.25: Surviving fraction curve for HeLa cells irradiated with carbon-ions ($LET_d = 100 \text{ keV}/\mu\text{m}$, PBS) in the presence and absence of DMSO (1 mM, 1 h): cells free of NPs and cells loaded with AuNPs (0.5 mM, 6 h incubation) in oxic ($pO_2 = 20\%$) condition.

SF varies from 0.1 for the control at 2 Gy to 0.25 when DMSO is added. This indicates that carbon ions ($LET_d = 100 \text{ keV}/\mu\text{m}$, PBS) induce damage produced by direct effects for more than 75% (and less than 25% by OH radicals). This confirms that the participation of complex damage is strongly enhanced due to the ionization density of the track. More interesting, the amplification effect by the NPs is not completely scavenged by DMSO showing that direct effects are responsible for the radio-enhancement when carbon ions PBS are used as ionizing radiation. This result is strongly different from the one obtained with helium-ion radiation ($LET_d = 50 \text{ keV}/\mu\text{m}$, SOBP) in which OH radical was the major contribution of amplification effects.

Chapter V

Discussion

This chapter aims at shedding some light on the molecular processes involved in the combination of ion radiation with NPs, and particularly on the role of oxygen. The results obtained in this work are first summarized within a simple table (section §1). Then an attempt to discuss the molecular scale effects involved in passive scattering beam delivery system for helium and carbon ion beams is made (section §2). In particular, the mechanism of oxidative stress induced by radiation is reviewed and applied to the amplification of the ion beam effects in the presence of NPs (section §3). The influence of the radiation quality (defined by the LET) in the biological response in oxic and anoxic conditions is raised.

1 Summary of the radio-enhancement of NPs activated by ion beams

In this work, the properties of AuNPs have been evaluated for all the radiation scenarios and oxygen concentrations applied in the two cell lines. PtNPs have been tested in some of these scenarios only, in particular under radiation by helium and carbon ion beams delivered by passive scattering system (SOBP mode). The effects of the two NPs on cell-killing of HeLa and BxPC-3 cells exposed to ion radiation (passive scattering) were rather similar, although uptake properties were slightly different.

Briefly, in oxic conditions, the two NPs presented significant radio-enhancement (with HeLa and BxPC-3 cells). In anoxic conditions, amplification effect was observed for helium-ion radiation only (although low for PtNPs) but, interestingly, no effect was found for carbon-ion radiation (passive scattering).

The effect of NPs using carbon-ion radiation delivered by PBS, was studied with AuNPs only. We observed an amplification of the carbon-ion radiation effects at the highest LET_d (100 keV/ μ m) in both oxic and anoxic conditions. On the contrary, no effect was found at a LET_d of 50 keV/ μ m.

In order to describe the main differences, the discussion is focused on the effects of oxygen and the beam quality on the radio-enhancement effect. The radio-enhancement effects of NPs with the different conditions are summarized in table V.1.

			Passive scattering (SOBP)				PBS	
			PtNPs		AuNPs		AuNPs	
	Ion	LET_d (keV/ μ m)	Oxic	Anoxic	Oxic	Anoxic	Oxic	Anoxic
BxPC-3	Helium	12	+	-	++	+	/	
BxPC-3	Carbon	50	++	-	++	-	/	
HeLa	Carbon	50	+	-	+	-	/	
HeLa	Carbon	50	/	/	/	/	-	-
HeLa	Carbon	100	/	/	/	/	++	+

Table V.1: Radio-enhancement of PtNPs and AuNPs activated by helium-ions ($LET_d = 12$ keV/ μ m, SOBP), carbon-ions ($LET_d = 50$ keV/ μ m, SOBP), carbon-ions ($LET_d = 50$ keV/ μ m, PBS) and carbon-ions ($LET_d = 100$ keV/ μ m, PBS) for BxPC-3 and HeLa cells. The following symbology was used: $SER \leq 5\%$ (-), $5\% < SER < 30\%$ (+), $SER \geq 30\%$ (++) .

2 Molecular scale effects

To ease the discussion, different scenarios of molecular scale processes as function of the radiation quality and the oxygen environment are schematized in figure V.1. This scheme includes the processes involved in the nucleus and in the cytoplasm of the cells. The processes potentially generated by carbon ions alone, carbon ions in the presence of NPs, helium ions alone and helium ions in the presence of NPs are represented.

The early stage effects of radiation, namely electron emission and water radiolysis in the close vicinity of the ion track, are represented in figure V.1, left column. The physico-chemical effects in anoxic and oxic conditions are reported in the central and right column respectively.

2.1 From early stage processes to the action of oxygen

The interaction of radiation with water is responsible for the production of $\bullet\text{OH}$, $\text{H}\bullet$ and secondary electrons along the track (see figure V.1, left column).

The effect of radiation on biosystems is commonly attributed to the production of $\bullet\text{OH}$ because it interacts with biomolecules (RH) with a high reaction rate ($R > 2.10^{10} \text{ mol}^{-1} \cdot \text{L} \cdot \text{s}^{-1}$). The interaction of OH radicals with biomolecules results in the production of unstable species in DNA ($\text{DNA}\bullet$, figure V.1, central column) and in the cytoplasm (organic radicals, $\text{R}\bullet$, figure V.1, central column) as due to hydrogen abstraction or $\bullet\text{OH}$ addition. These unstable species may also be produced by the direct interaction of e^- with the biomolecules (direct effect). The interaction of $\bullet\text{OH}$ clusters or e^- spurs with biomolecules is responsible for the induction of complex lesions (DNA: and R:).

It was shown that cell-killing induced by photon radiation is due to the production of $\bullet\text{OH}$ for 60-90% [Roots and Okada, 1972, Chapman et al., 1973, Shinohara et al., 1996]. In the case of carbon ion radiation (180 keV/ μm) the action of OH radicals counts for more than 50% [Chapman et al., 1979]. Our study demonstrated that 50% of the radiation effects is due to direct effects and 50% to $\bullet\text{OH}$ -mediated damage (at 2 Gy) when using helium ion radiation ($\text{LET}_d = 12 \text{ keV}/\mu\text{m}$, SOBP). Carbon ions ($\text{LET}_d = 100 \text{ keV}/\mu\text{m}$, PBS) induce damage produced by direct effects for more than 75% (and less than 25% by OH radicals). This confirms that the participation of complex damage is strongly enhanced due to the increase of the ionization density of the track.

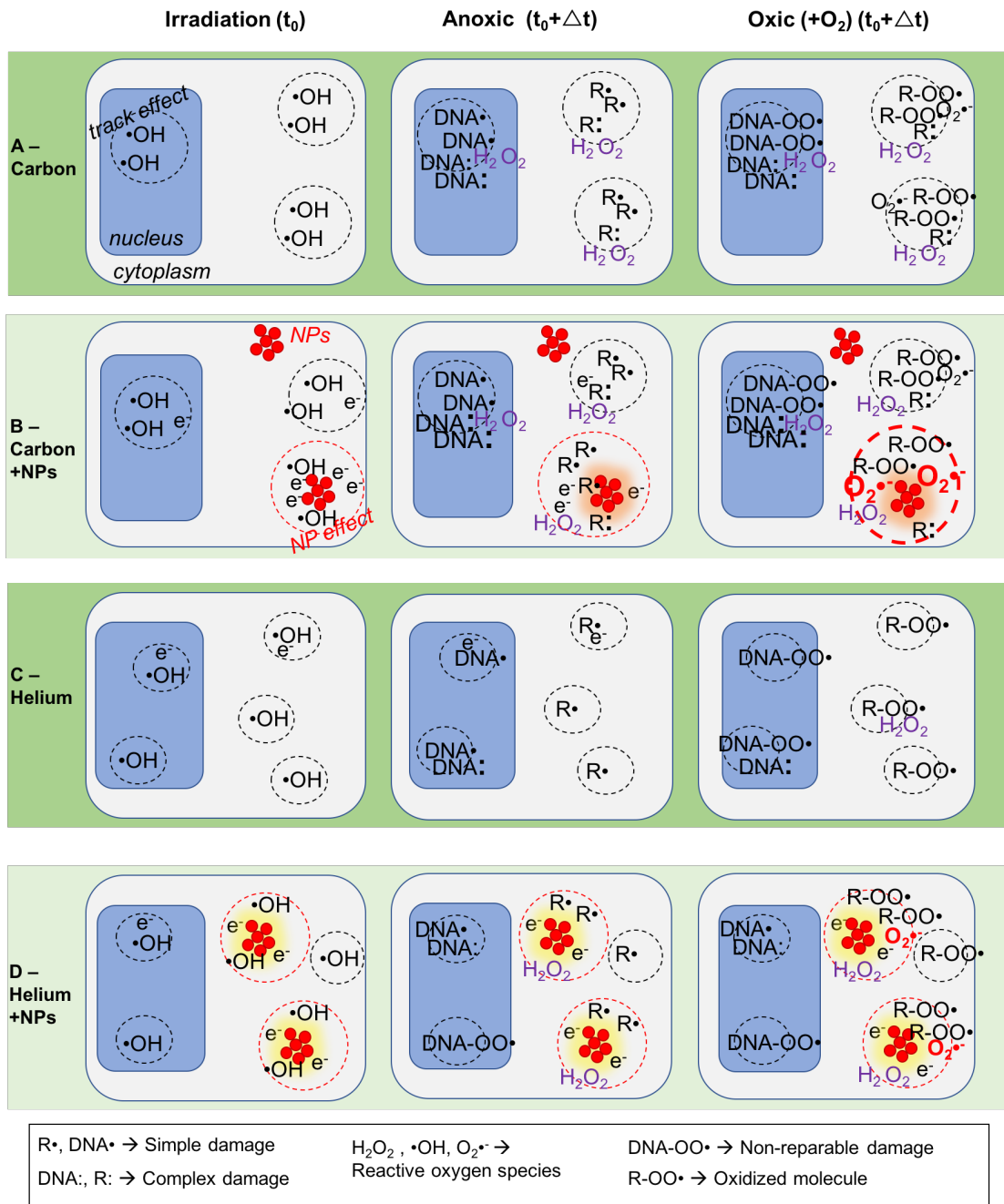


Figure V.1: Processes involved in the cells at molecular scale when cells are irradiated by A) carbon-ions, B) carbon-ions in the presence of NPs, C) helium-ions, D) helium-ions in the presence of NPs. The early stage effects (left column), and physico-chemical effects in anoxic (central central) or oxidic conditions (right column) are depicted.

2. MOLECULAR SCALE EFFECTS

In oxic conditions (figure V.1, right column), R^\bullet species and DNA^\bullet may react with molecular oxygen resulting in the “fixation” of radical defects to form oxidized molecules species (ROO^\bullet and $DNA-OO^\bullet$) (see figure V.2 and figure V.1, right column). The fixation of these defects makes their repair unlikely. Note that R^\bullet (and DNA^\bullet) can also be “fixed” by $O_2^{\bullet-}$, a byproduct produced by the attachment of e_{aq}^- with O_2 . $O_2^{\bullet-}$ does not react directly with biomolecules but with R^\bullet radicals.

In anoxic conditions (figure V.1, central column), the “fixation” of radicals by O_2 is shut down. On the other hand, radicals may rearrange or react with radical-reducing species, which results in chemical repair. In the case of nuclear DNA, a single lesion in the backbone or in a base (DNA^\bullet) may be repaired. However complex lesions (i.e. several defects within a volume of 2-10 nm) are not reparable.

In summary, the sensitizing effect of oxygen is commonly believed to be caused by the “fixation” of radiation-induced damage by O_2 or $O_2^{\bullet-}$ which makes the organic lesions permanent. However, complex lesions are intrinsically lethal independently from the presence of oxygen.

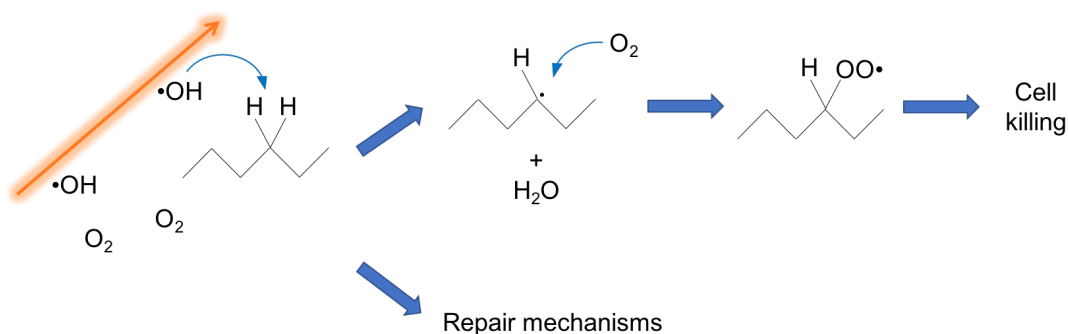


Figure V.2: Oxidation of organic molecules by $\bullet OH$ and fixation by O_2 .

2.2 Influence of the radiation LET

Figure V.3 shows a schematic representation of a cell irradiated with high LET (carbon-ions) and low LET (helium-ions) beam. A larger halo around the incident tracks represents a greater electron emission and $\bullet OH$ production. For 1 Gy dose deposition, the

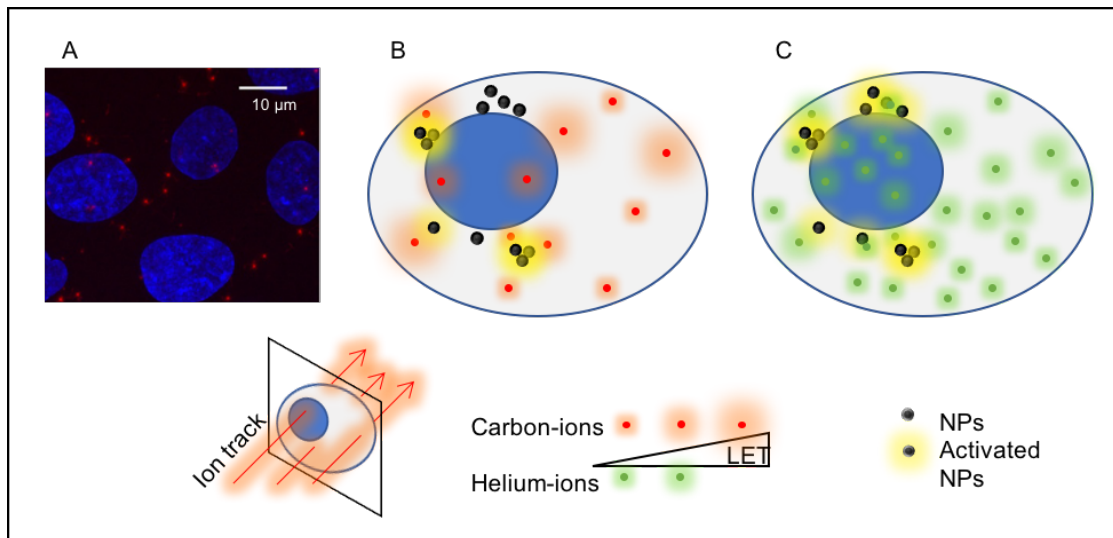


Figure V.3: (A) Correlation between carbon ion tracks (red) and a cell layer (cell nucleus in blue) (adapted from [Niklas et al., 2013]). (B) and (C) Scheme of a cell loaded with nanoparticles (black dots) exposed to carbon (red) and helium (green) ion radiation. A larger halo represents a higher LET.

number of helium tracks ($LET_d = 12 \text{ keV}/\mu\text{m}$) is 4-5 times higher than the number of carbon ion tracks ($LET_d = 50 \text{ keV}/\mu\text{m}$).

When the LET increases, the production of $\bullet\text{OH}$ in the ion track decreases because of the recombination of $\bullet\text{OH}$ in H_2O_2 [Yamashita et al., 2008, Burns, 1981, Appleby and Schwarz, 1969, LaVerne, 2000]. Nonetheless, cell-killing increases with the LET [Furusawa et al., 2000]. This is attributed to the induction of complex lesions, which increases with the ionizing density of the incident track (see figure V.1, rows A and C). The induction of complex lesions (by $\bullet\text{OH}$ clusters or e^- spurs) is responsible for the high lethality of ion beams. Note that H_2O_2 is also toxic and contribute to radiation lethality, but less than $\bullet\text{OH}$.

Our work confirmed this result. Cell-killing with incident ions was found stronger than with gamma rays ($RBE = 1.2$ for helium-ions and 1.6 to 1.9 for carbon ions) and cell-killing was higher with carbon-ions ($LET_d = 50 \text{ keV}/\mu\text{m}$) than with helium-ions ($LET_d = 12 \text{ keV}/\mu\text{m}$).

This work confirms that the lethality of radiation protocols depends not only on the yield but also on the density and diffusion of OH radicals, and on the complexity of damages.

2.3 Dependence of the oxygen effect on the LET

The influence of oxygen is different depending on the radiation quality as shown by comparison of the OER values. In the present work, OER values of 2.1-2.3 were found for HeLa and BxPC-3 exposed to carbon-ion radiation (SOBP, $LET_d = 50 \text{ keV}/\mu\text{m}$). For helium ions (SOBP, $LET_d = 12 \text{ keV}/\mu\text{m}$), the OER increased to 2.7 for BxPC-3 cells (compared to 2.3 with carbon ions). The decrease of OER with increasing LET is attributed to the production of complex damages for which the lethality does not depend on the “fixation” by O_2 . The same trend was observed with the PBS modality: the OER increased from 1.6 with a carbon-ion beam $100 \text{ keV}/\mu\text{m}$ to 2.3 with a beam of $50 \text{ keV}/\mu\text{m}$ (for HeLa cells).

3 Influence of NPs on radiation induced effects

The activation of NPs by the incident track (i.e. incident particle and the electrons emitted in the track) amplifies the emission of secondary electrons in their close vicinity (see figure V.1, rows B and D). This increases the production of OH radicals close to the NPs by interaction of secondary electrons with water molecules thus forming radical clusters.

The result of the NP activation/relaxation is the perturbation of the cytoplasm due to the following processes:

- a) The interaction of highly reactive OH clusters or electrons spurs with cytoplasmic constituents may induce complex lesions in cytoplasmic constituents (e.g. proteins, enzymes) (R: in figure V.1, central column).
- b) The production of H_2O_2 is enhanced due to the recombination of $\bullet OH$.

These two processes are oxygen independent and may take place in oxic and anoxic conditions.

- c) In oxic conditions, $R\bullet$ may be “fixed” by O_2 (or $O_2\bullet^-$ produced in the vicinity) forming other oxidative species $ROO\bullet$.

Stated differently, the processes involved in anoxic conditions may take place in the presence of O_2 but the contrary is not true. Moreover, it is important to remind that the effect of NPs on cell-killing results from the superimposition of the cytoplasmic perturbation and the nuclear DNA damage together. From these simple principles, we may draw some general trends as a function of the radiation modality.

3.1 Ion radiation using passive scattering delivery system

In anoxic conditions, the effects of NPs were strongly radiation dependent. NPs did not amplify radiation effects in the case of HeLa and BxPC-3 exposed to carbon ions

(passive scattering, SOBP). The processes (1) and (2) only apply. The induction of complex damages and production of H_2O_2 increase with the LET. Obviously the increase of nuclear damage has a stronger impact than the contribution of the cytoplasm and no radio-enhancement is observed. In the case of helium ions, the damages in nuclear DNA are less lethal and the cytoplasm contributes more to cell-killing when NPs are present.

In the presence of O_2 , the lethality due to nuclear damage and to the cytoplasmic perturbation increase but the additional superimposition of the process (3) increases the contribution of the cytoplasmic perturbation in cell-killing.

The "fixation" of radiation-induced effects by O_2 (or $O_2^{\bullet-}$) plays a major role in the radio-enhancement by NPs. Interestingly, the location of the perturbation in the cytoplasm (mitochondria or lysosomes) is not critical.

3.2 Ion radiation using PBS delivery system

Using the PBS delivery system, the effect of NPs is fully independent of the oxygen concentration. Radio-enhancement by AuNPs was observed for carbon-ion ($LET_d = 100$ keV/ μm) in both oxic and anoxic conditions. On the contrary, no variation was observed with $LET_d = 50$ keV/ μm (in oxic and anoxic conditions). These trends are different from the effect of carbon ion ($LET_d = 50$ keV/ μm – passive scattering) described before.

In the combination of NPs with carbon ion radiation (PBS), the process (3) (O_2 “fixation” of damage) does not prevail. The induction of complex lesions and production of H_2O_2 only count for cell-killing enhancement. In these experiments, ion radiation with PBS may be considered as mono-energetic beams where the major LET component is 50 keV/ μm or 100 keV/ μm . We attribute the amplification of cell-killing with carbon ions 100 keV/ μm – PBS to a stronger activation of NPs by the electrons emitted along the high density track, which increases the induction of complex lesions in cytoplasmic constituents. In this case, the resulting cytoplasmic perturbation exceeds the impact of nuclear DNA damage.

The efficiency of the quasi mono-energetic carbon 50 keV/ μm – PBS to induce complex damages in the cytoplasm is weaker and the NPs do not balance the impact of DNA damage.

The effect of NPs is strongly dependent on the radiation field (LET spectra) and thus it depends on the ion beam delivery system.

Chapter VI

Conclusion and perspectives

The **main goal** of my PhD was to study the effect of molecular oxygen (O_2) in ion beam radiation combined with nanoparticles (NPs).

In this perspective, **experiments** were carried out on human cancer cell lines exposed to nanoparticles and treated by different medical ion radiations. Three concentrations of oxygen were considered. The specific conditions used for this study are summarized below.

- HeLa (cervix uterine cancer) and BxPC-3 (pancreas cancer) were used as cellular models because of their radioresistance to conventional x-ray radiation.
- Two small metallic nanoparticles (~ 3 nm core diameter), platinum nanoparticles (PtNPs) and gold nanoparticles (AuNPs) with already proven good properties of electron emission were tested. In particular PtNPs coated with PEG-OH polymers are synthesized by radiolysis, a singular method optimized by the group, which consists in a one-step protocol with water used as main buffer. At the end of the synthesis, a sterile colloid solution ready-to-use for *in vitro/in vivo* application (without filtering) is produced. AuNPs developed by S. Roux and co-workers (Bourgogne - Franche - Comté University, Besançon, France) are functionalized with DTDTPA, an agent that is biocompatible and able to host multimodal compounds such as fluorescent tags (i.e. cyanine 5) or MRI active compounds (i.e. Gd atoms). It has been shown that AuNPs accumulate in mice tumors.

- Various ion beam radiations including carbon (50 keV/ μm) and helium (12 keV/ μm) ion beam radiations delivered by a passive scattering system – SOB mode (HIMAC, Chiba, Japan), and carbon (50 and 100 keV/ μm) ion radiations provided by a pencil beam scanning (PBS) system (HIT, Heidelberg, Germany) were considered.
- Three different oxygen conditions ($p\text{O}_2 = 0, 0.5$ and 20%) were used.

The first results concern the uptake and localization of NPs in cancer cells. We observed that: i) the uptake in BxPC-3 is 4-5 times higher than in HeLa (for instance 2×10^5 NPs/cell for AuNPs in HeLa compared to 1×10^6 NPs/cell in BxPC-3), ii) the uptake of PtNPs (2×10^6 NPs/cell in BxPC-3) is 2 times higher than the uptake of AuNPs in the same cells (1×10^6 NPs/cell in BxPC-3), iii) a major finding is that PtNPs and AuNPs are located in the cytoplasm exclusively. AuNPs in particular sit in mitochondria of HeLa cells, whilst they co-localize with lysosomes in BxPC-3 cells. A detailed study of the AuNPs uptake is currently performed by another PhD within the ITN ARGENT Project (thesis of Vladimir Ivosev supervised by Sandrine Lacombe).

The ion radiation studies with NPs-free cells exposed to passive ion beam scattering (SOBP mode) confirmed that cell-killing induced by high LET radiation (carbon ions) is more lethal than by low LET (helium ions or protons). This effect is explained by the induction of nuclear DNA damage, which is more complex for high ionization density tracks (high LET). We also found that 50% of the cell-killing is due to $\bullet\text{OH}$ -mediated processes when the cells are exposed to helium ion beam (this experiment was not performed for carbon ions). The other 50% of the cell-killing may be attributed to DNA damage induced by electrons (independent from $\bullet\text{OH}$) or by the action of toxic species produced by radiation such as H_2O_2 (resulting from $\bullet\text{OH}$ recombination and not scavenged by DMSO). The contribution of $\bullet\text{OH}$ -mediated damage decreases when LET increases (25% with carbon ion beams of $\text{LET} = 100 \text{ keV}/\mu\text{m}$).

The radiation effect increased with the concentration of oxygen (from $p\text{O}_2 = 0\%$ in anoxic condition to $p\text{O}_2 = 20\%$ in oxic condition). This corresponds to the well-known sensitizing effect of O_2 [Furusawa et al., 2000]. A concentration of O_2 as low as 0.5% is sufficient to sensitize the cells. The sensitization effect is explained by the “fixation” of the radiation-induced defects by O_2 with production of peroxy radicals (for instance $\text{DNA-OO}\bullet$), which makes the lesions permanent [Brown and Wilson, 2004]. A significant decrease of the OER was observed when increasing the LET (OER = 2.7 with

helium ions $LET_d = 12 \text{ keV}/\mu\text{m}$, SOBP; OER = 2.3 with carbon ions $LET_d = 50 \text{ keV}/\mu\text{m}$, SOBP). This indicates that the role of O_2 fixation becomes minor when the induction of lethal DNA lesions increases. This is in full agreement with other studies, which have demonstrated that carbon ions are responsible for the induction of complex DNA lesions [Hirayama et al., 2015]. This conclusion stems from the irradiation with PBS where a lower OER (OER = 1.6) was observed with carbon-ions $LET_d = 100 \text{ keV}/\mu\text{m}$ than with carbon-ions $LET_d = 50 \text{ keV}/\mu\text{m}$ (OER = 2.3).

The studies of NPs effect on the ion radiation performances, **major focus of this work**, demonstrated that the results are not significantly different for the two NPs (PtNPs and AuNPs) and for the two cell lines (although NPs sit in different cell compartments). The effects of NPs depend predominantly on the radiation quality (helium or carbon ions, passive scattering or PBS delivery modes) and on the oxygen concentration.

In oxic condition a significant enhancement of radiation effect by PtNPs and AuNPs was found for most of the radiation protocols (carbon $50 \text{ keV}/\mu\text{m}$ and helium $12 \text{ keV}/\mu\text{m}$ – passive scattering, and carbon $100 \text{ keV}/\mu\text{m}$ – PBS). This is in agreement with previous results obtained with gadolinium based NPs, which demonstrated for the first time the possibility to enhance carbon ion radiation (passive scattering) induced cell-killing by adding NPs [Porcel et al., 2014]. The effect of NPs is well explained by the succession of nanoscale effects: i) amplification of electron emission in the close vicinity (due to the electronic activation of NPs by incident ions or by electrons produced in the tracks), ii) consecutive production of OH radicals due to water radiolysis (and possibly H_2O_2) and iii) induction of lethal damages by OH radicals or electrons.

It is important to mention that this perturbation is initiated in the cytoplasm exclusively. The total effect of NPs results from the additive effects of nuclear damage and cytoplasmic perturbation. In summary, the enhancement of cell-killing depends not only on the efficiency of the incident beam to activate NPs but also on the relative contribution of the cell compartments (nucleus versus cytoplasm).

The effect of NPs is observed only when the perturbation in the cytoplasm exceeds the effect of nuclear damage.

This is the first time that the effect of NPs on carbon ion radiation - PBS delivery system is tested. We found that NPs enhance the radiation effects in the case of carbon ions $LET_d = 100 \text{ keV}/\mu\text{m}$ but not at lower LET ($LET_d = 50 \text{ keV}/\mu\text{m}$). This is in agreement with results obtained recently with 150 MeV protons, where a higher effect of NPs was found

when combined with a beam of higher LET [Schlatholter et al., 2016]. This is explained by the activation of NP that increases with the ionization density of the track resulting in the production of complex (nanosize) lesions in cell cytoplasmic constituents.

This work shows that NPs may improve carbon ion radiation (PBS) treatments by enhancing the effects of ions at the end of the tracks, in the tumor.

Another major contribution of my work is the understanding of the radio-enhancement mechanisms by changing the O₂ concentration. When radiation effects are enhanced in oxic conditions only, it tells that the production of O₂-“fixed” lesions plays a major role and increases the contribution of the cytoplasmic perturbation, which becomes significant compared to nuclear damage. This is the case of NPs combined with carbon LET_d = 50 keV/μm (passive scattering) (with rather similar effect for the two NPs, independently from their localization in mitochondria or lysosomes). On the other hand, an amplification of the radiation effect in anoxic and oxic conditions means that NPs enhance rather the production of complex damages or toxic species such as H₂O₂. This is the case of helium ions (passive scattering) and carbon ions LET_d = 100 keV/μm (PBS system).

In **summary**, NPs impact differently the radiation treatments depending on the radiation quality and the concentration in oxygen:

- In the case of helium ion radiation (LET_d = 12 keV/μm – passive scattering), NPs enhance radiation effects in oxic and anoxic conditions because the contribution of the cytoplasm always exceeds the effect of DNA damage.
- In the case of carbon ion radiation (LET_d = 50 keV/μm – passive scattering), the induction of complex DNA damages makes the relative role of the cytoplasm weaker. So an enhancement of radiation effects with NPs is observed when molecular oxygen is present and enhance the cytoplasmic contribution to cell-killing.
- In the case of “quasi-monoenergetic” carbon-ion radiation (LET_d = 100 keV/μm – PBS), the scenario is different. The activation of NPs by high ionizing tracks increases the induction of complex (nanosize) damage in cytoplasmic constituents and/or the production of H₂O₂. This balances the impact of DNA damage and makes radio-enhancement by NPs very efficient in both oxic and anoxic conditions.
- The effect of “quasi-monoenergetic” carbon-ion radiation (LET_d = 50 keV/μm – PBS) to activate NPs is weaker than with 100 keV/μm – PBS carbon ions. Damage

in nuclear DNA exceeds the effects of cytoplasmic perturbation. NPs do not amplify efficiently this radiation treatment.

In **conclusion**, this work has contributed to demonstrate the high potential of NPs to improve ion radiation effects in tumor cells in oxic, hypoxic and anoxic conditions. This strategy opens the perspective to improve the treatment of hypoxic tumors by amplifying the effect of radiation and reduce the total dose given to the patient. The effectiveness of the combined protocol depends on the radiation modality. Treatments with helium ions in particular, which have a lower RBE than carbon ion beam, may benefit from the radio-enhancement by NPs. These major results encourage the group to perform *in vivo* experiments.

As a major **perspective**, the evaluation of the combined protocols of PtNPs and/or AuNPs with medical ion beams (helium, carbon but also protons) to treat various tumor cases in mice would be a major step.

In addition, to further develop the strategy combining NPs and ion radiation, theoretical models and simulations are strongly needed to better characterize but also implement the effects of NPs in treatment planning. This is the work initiated by Daria Boscolo and Martina Fuss, under the supervision of Emanuele Scifoni, Michael Krämer and Marco Durante within the frame of the ARGENT project.

Another major challenge is the development of novel nanoagents. Intravenous injection is used to concentrate NPs in the tumors. Enhanced permeability and retention (EPR) effect is the main mechanism that concentrate NPs in the tumors. It is known that diffusion distances from tumor vasculature to hypoxic cells may be large. In the perspective of enriching hypoxic regions with nanoagents, sophisticated mechanisms of delivery are required. For instance, a novel approach using the phagocytic actions of blood monocytes to internalizes 60 nm diameter gold nanoshells and transport them to hypoxic tumor regions [Choi et al., 2007] has been proposed and its efficacy was demonstrated in 3D tumor models *in vitro*. The development of novel nano-carriers able to reach hypoxic regions and containing electron emitters is thus an important challenge. In contrast, nanoagents may be designed to concentrate in the peripheral oxygenated region of the tumor. This application may be of interest with the view to delineate and effectively treats the peripheral extension of the tumor specifically (without increasing the total dose to healthy tissue). Nanoagents also opens the perspective to carry multimodal compounds able to not only enhance radiation effects but also improve medical imaging

(gadolinium for instance). The implementation of theranostic in particle therapy would improve the observation of NPs in the body before and after irradiation as well as the tumor diagnosis.

Finally, this thesis has contributed to a deeper understanding of the role of oxygen and radiation quality in the radio-enhancement of ion radiation by small metallic NPs (figure VI.1). The sum of the three milestones proposed above (*in vivo* evidence, simulations, new nanocarriers) will ultimately contribute to the development of new ion beam/NPs clinical protocols.

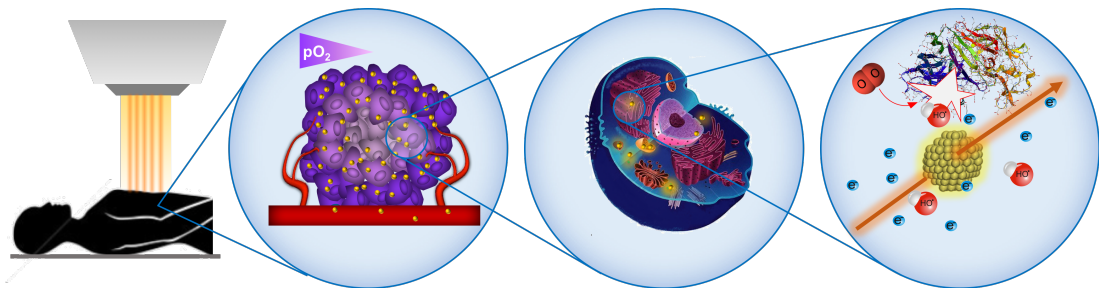


Figure VI.1: Oxygen effect in medical ion beam radiation combined with metallic nanoparticles. From nanoscopic mechanisms to cellular effects.

Bibliography

- [Adler and Parmryd, 2010] Adler, J. and Parmryd, I. (2010). Quantifying colocalization by correlation: The pearson correlation coefficient is superior to the Mander's overlap coefficient. *Cytometry Part A*, 77(8):733–742.
- [Alpen, 1997] Alpen, E. L. (1997). *Radiation biophysics*. Academic Press.
- [Alric et al., 2013] Alric, C., Miladi, I., Kryza, D., Taleb, J., Lux, F., Bazzi, R., Billotey, C., Janier, M., Perriat, P., Roux, S., and Tillement, O. (2013). The biodistribution of gold nanoparticles designed for renal clearance. *Nanoscale*, 5(13):5930.
- [Alric et al., 2008] Alric, C., Taleb, J., Duc, G. L., Mandon, C., Billotey, C., Meur-herland, A. L., Brochard, T., Vocanson, F., Janier, M., Perriat, P., Roux, S., Tillement, O., Cnrs, U. M. R., Inserm, U., Lyon, I. D., Uni, V., Bernard, C., and Lyon, C. B. (2008). Agents for Both X-ray Computed Tomography and Magnetic Resonance Imaging. (13):5908–5915.
- [Appleby and Schwarz, 1969] Appleby, A. and Schwarz, H. A. (1969). Radical and Molecular Yields in Water Irradiated by γ rays and heavy ions. *Journal of Physical Chemistry*, 73(6):1937–1941.
- [Attix, 2004] Attix, F. H. (2004). *Introduction to radiological physics and radiation dosimetry*. Wiley-VCH.
- [Barendsen, 1968] Barendsen, G. (1968). Response of cultured cells, tumours and normal tissues to radiations of different linear energy transfer. *Current topics in radiation research quarterly*, 4.
- [Belli et al., 2008] Belli, M., Bettega, D., Calzolari, P., Cherubini, R., Cuttone, G., Durante, M., Esposito, G., Furusawa, Y., Gerardi, S., Gialanella, G., Grossi, G., Manti,

- L., Marchesini, R., Pugliese, M., Scampoli, P., Simone, G., Sorrentino, E., Tabocchini, M. A., and Tallone, L. (2008). Effectiveness of monoenergetic and spread-out bragg peak carbon-ions for inactivation of various normal and tumour human cell lines. *Journal of Radiation Research*, 49(6):597–607.
- [Berger et al., 1993] Berger, M. J., Inokuti, M., Andersen, H. H., Bichsel, H., Powers, D., Seltzer, S. . M., Thwaites, D. ., and Watt, D. E. (1993). Report 49. *Journal of the International Commission on Radiation Units and Measurements*, os25(2):NP–NP.
- [Bexiga et al., 2011] Bexiga, M. G., Varela, J. A., Wang, F., Fenaroli, F., Salvati, A., Lynch, I., Simpson, J. C., and Dawson, K. A. (2011). Cationic nanoparticles induce caspase 3-, 7- and 9-mediated cytotoxicity in a human astrocytoma cell line. *Nanotoxicology*, 5(4):557–567.
- [Bhide and Nutting, 2010] Bhide, S. and Nutting, C. (2010). Recent advances in radiotherapy. *BMC Medicine*, 8(1):25.
- [Bichsel, 1990] Bichsel, H. (1990). Barkas effect and effective charge in the theory of stopping power. *Physical Review A*, 41(7):3642–3647.
- [Bimbot et al., 2005] Bimbot, R., Geissel, H., Paul, H., Schinner, A., Sigmund, P., Wambersie, A., DeLuca, P. M., and Seltzer, S. M. (2005). *Stopping of ions heavier than helium*, volume 5.
- [Blakely et al., 1983] Blakely, E. A., Ngo, F. Q., Curtis, S. B., and Tobias, C. A. (1983). HEAVY-ION RADIOBIOLOGY: CELLULAR STUDIES. *Advances in Radiation Biology*, Spring/Summer 1983.
- [Bolsa Ferruz et al., 2017] Bolsa Ferruz, M., Ivošev, V., Haume, K., Ellis-Gibblings, L., Traore, A., Thakare, V., Rosa, S., de Vera, P., Tran, V.-L., Mika, A., Boscolo, D., Grellet, S., Verkhovtsev, A., Huber, B. A., Butterworth, K. T., Prise, K. M., Currell, F. J., Mason, N. J., Golding, J., Scifoni, E., García, G., Boschetti, F., Lux, F., Tillement, O., Louis, C., Stokbro, K., Solov'yov, A. V., and Lacombe, S. (2017). New Research in Ionizing Radiation and Nanoparticles: The ARGENT Project. *Nanoscale Insights into Ion-Beam Cancer Therapy*, pages 379–434.
- [Bonvalot et al., 2017] Bonvalot, S., Le Pechoux, C., De Baere, T., Kantor, G., Buy, X., Stoeckle, E., Terrier, P., Sargos, P., Coindre, J. M., Lassau, N., Sarkouh, R. A., Dimitriu, M., Borghi, E., Levy, L., Deutsch, E., and Soria, J. C. (2017). First-in-human

- study testing a new radioenhancer using nanoparticles (NBTXR3) activated by radiation therapy in patients with locally advanced soft tissue sarcomas. *Clinical Cancer Research*, 23(4):908–917.
- [Bragg and Kleeman, 1905] Bragg, W. H. and Kleeman, R. (1905). XXXIX. On the α particles of radium, and their loss of range in passing through various atoms and molecules. *Philosophical Magazine Series 6*, 10(57):318–340.
- [Brown and Giaccia, 1998] Brown, J. M. and Giaccia, A. J. (1998). The unique physiology of solid tumors: opportunities (and problems) for cancer therapy. *Cancer research*, 58(7):1408–1416.
- [Brown and Wilson, 2004] Brown, J. M. and Wilson, W. R. (2004). Exploiting tumour hypoxia in cancer treatment. *Nat Rev Cancer*, 4(6):437–447.
- [Brust et al., 1995] Brust, M., Fink, J., Bethell, D., Schiffrin, D. J., and Kiely, C. (1995). Synthesis and reactions of functionalised gold nanoparticles. *Journal of the Chemical Society, Chemical Communications*, (16):1655–1656.
- [Burns, 1981] Burns, W. G. (1981). Effect of Radiation Type in Water Radiolysis. *J. Chem. SOC. Faraday Trans. I*, 77(11):2803–2813.
- [Butterworth et al., 2012] Butterworth, K. T., McMahon, S. J., Currell, F. J., and Prise, K. M. (2012). Physical basis and biological mechanisms of gold nanoparticle radiosensitization. *Nanoscale*, 4(16):4830–8.
- [Butterworth et al., 2016] Butterworth, K. T., Nicol, J. R., Ghita, M., Rosa, S., Chaudhary, P., McGarry, C. K., McCarthy, H. O., Jimenez-Sanchez, G., Bazzi, R., Roux, S., Tillement, O., Coulter, J. A., and Prise, K. M. (2016). Preclinical evaluation of gold-DTDTPA nanoparticles as theranostic agents in prostate cancer radiotherapy. *Nanomedicine*, 11(16):2035–2047.
- [Chapman et al., 1979] Chapman, J. D., Doern, S. D., Reuvers, A. P., Gillespie, C. J., Chatterjee, A., Blakely, E. A., Smith, K. C., and Tobias, C. A. (1979). Radioprotection by DMSO of mammalian cells exposed to X-rays and to heavy charged-particle beams. *Radiation and Environmental Biophysics*, 16(1):29–41.
- [Chapman et al., 1973] Chapman, J. D., Reuvers, A. P., Borsa, J., and Greenstock, C. L. (1973). Chemical Radioprotection and Radiosensitization of Mammalian Cells Growing in Vitro. *Radiation Research*, 56(2):291.

- [Choi et al., 2007] Choi, M. R., Stanton-Maxey, K. J., Stanley, J. K., Levin, C. S., Bardhan, R., Akin, D., Badve, S., Sturgis, J., Robinson, J. P., Bashir, R., Halas, N. J., and Clare, S. E. (2007). A cellular trojan horse for delivery of therapeutic nanoparticles into tumors. *Nano Letters*, 7(12):3759–3765.
- [Combs et al., 2010] Combs, S. E., Jakel, O., Haberer, T., and Debus, J. (2010). Particle therapy at the Heidelberg Ion Therapy Center (HIT) - Integrated research-driven university-hospital-based radiation oncology service in Heidelberg, Germany. *Radiother Oncol*, 95(1):41–44.
- [Coulter et al., 2012] Coulter, J. A., Jain, S., Butterworth, K. T., Taggart, L. E., Dickson, G. R., McMahon, S. J., Hyland, W. B., Muir, M. F., Trainor, C., Hounsell, A. R., O’Sullivan, J. M., Schettino, G., Currell, F. J., Hirst, D. G., and Prise, K. M. (2012). Cell type-dependent uptake, localization, and cytotoxicity of 1.9 nm gold nanoparticles. *Int J Nanomedicine*, 7:2673–2685.
- [Debouttière et al., 2006] Debouttière, P.-J., Roux, S., Vocanson, F., Billotey, C., Beuf, O., Favre-Réguillon, a., Lin, Y., Pellet-Rostaing, S., Lamartine, R., Perriat, P., and Tillement, O. (2006). Design of Gold Nanoparticles for Magnetic Resonance Imaging. *Advanced Functional Materials*, 16(18):2330–2339.
- [Feldman and Mayer, 1986] Feldman, L. C. and Mayer, J. W. (1986). Fundamentals of surface and thin film analysis. *North Holland, Elsevier Science Publishers, P. O. Box 211, 1000 AE Amsterdam, The Netherlands, 1986.*
- [Furusawa et al., 2000] Furusawa, Y., Fukutsu, K., Aoki, M., Itsukaichi, H., Eguchi-Kasai, K., Ohara, H., Yatagai, F., Kanai, T., and Ando, K. (2000). Inactivation of aerobic and hypoxic cells from three different cell lines by accelerated (3)He-, (12)C- and (20)Ne-ion beams. *Radiation research*, 154(5):485–496.
- [Garrido-Laguna and Hidalgo, 2015] Garrido-Laguna, I. and Hidalgo, M. (2015). Pancreatic cancer: from state-of-the-art treatments to promising novel therapies. *Nature reviews Clinical oncology*, 12(6):319–334.
- [Guan et al., 2015] Guan, F., Peeler, C., Bronk, L., Geng, C., Taleei, R., Randeniya, S., Ge, S., Mirkovic, D., Grosshans, D., Mohan, R., and Titt, U. (2015). Analysis of the track- and dose-averaged LET and LET spectra in proton therapy using the GEANT4 Monte Carlo code. *Medical physics*, 42(11):6234.

- [Gueulette et al., 2004] Gueulette, J., Octave-Prignot, M., De Coster, B.-M., Wambersie, A., and Gregoire, V. (2004). Intestinal crypt regeneration in mice : a biological system for quality assurance in non-conventional radiation therapy. *Radiotherapy and Oncology*, 73(Supplement 2):S148–S154.
- [Haberer et al., 1993] Haberer, T., Becher, W., Schardt, D., and Kraft, G. (1993). Magnetic scanning system for heavy ion therapy. *Nuclear Inst. and Methods in Physics Research, A*, 330(1-2):296–305.
- [Hatano et al., 2011] Hatano, Y., Katsumura, Y., and Mozumder, A. (2011). *Charged particle and photon interactions with matter : recent advances, applications, and interfaces*. CRC Press.
- [Hirayama et al., 2009] Hirayama, R., Matsumoto, Y., Kase, Y., Noguchi, M., Ando, K., Ito, A., Okayasu, R., and Furusawa, Y. (2009). Radioprotection by DMSO in nitrogen-saturated mammalian cells exposed to helium ion beams. *Radiation Physics and Chemistry*, 78(12):1175–1178.
- [Hirayama et al., 2015] Hirayama, R., Uzawa, A., Obara, M., Takase, N., Koda, K., Ozaki, M., Noguchi, M., Matsumoto, Y., Li, H., Yamashita, K., Koike, S., Ando, K., Shirai, T., Matsufuji, N., and Furusawa, Y. (2015). Determination of the relative biological effectiveness and oxygen enhancement ratio for micronuclei formation using high-LET radiation in solid tumor cells: An in vitro and in vivo study. *Mutat Res Genet Toxicol Environ Mutagen*, 793:41–47.
- [Hirayama et al., 2013] Hirayama, R., Uzawa, A., Takase, N., Matsumoto, Y., Noguchi, M., Koda, K., Ozaki, M., Yamashita, K., Li, H., Kase, Y., Matsufuji, N., Koike, S., ichiro Masunaga, S., Ando, K., Okayasu, R., and Furusawa, Y. (2013). Evaluation of SCCVII tumor cell survival in clamped and non-clamped solid tumors exposed to carbon-ion beams in comparison to X-rays. *Mutation Research - Genetic Toxicology and Environmental Mutagenesis*, 756(1-2):146–151.
- [Höckel et al., 1991] Höckel, M., Schlenger, K., Knoop, C., and Vaupel, P. (1991). Oxygenation of carcinomas of the uterine cervix: evaluation by computerized O₂ tension measurements. *Cancer research*, 51(22):6098–6102.
- [Houée-Lévin et al., 2015] Houée-Lévin, C., Bobrowski, K., Horakova, L., Karademir, B., Schöneich, C., Davies, M. J., and Spickett, C. M. (2015). Exploring oxidative modifications of tyrosine: An update on mechanisms of formation, advances in analysis and biological consequences. *Free radical research*, 5762(December):1–27.

- [IAEA, 2008] IAEA (2008). Relative Biological Effectiveness in Ion Beam Therapy. *IAEA Technical Reports*, (461):1–165.
- [Jain et al., 2014] Jain, S., Coulter, J. A., Butterworth, K. T., Hounsell, A. R., McMahon, S. J., Hyland, W. B., Muir, M. F., Dickson, G. R., Prise, K. M., Currell, F. J., Hirst, D. G., and O’Sullivan, J. M. (2014). Gold nanoparticle cellular uptake, toxicity and radiosensitisation in hypoxic conditions. *Radiotherapy and Oncology*, 110(2):342–347.
- [Jain et al., 2011] Jain, S., Coulter, J. A., Hounsell, A. R., Butterworth, K. T., McMahon, S. J., Hyland, W. B., Muir, M. F., Dickson, G. R., Prise, K. M., Currell, F. J., O’Sullivan, J. M., and Hirst, D. G. (2011). Cell-Specific Radiosensitization by gold nanoparticles at megavoltage radiation energies. *International Journal of Radiation Oncology Biology Physics*, 79(2):531–539.
- [Jeynes et al., 2014] Jeynes, J. C. G., Merchant, M. J., Spindler, A., Wera, A.-C., and Kirkby, K. J. (2014). Investigation of gold nanoparticle radiosensitization mechanisms using a free radical scavenger and protons of different energies. *Physics in Medicine and Biology*, 59(21):6431–6443.
- [Joiner and Van der Kogel, 2009] Joiner, M. and Van der Kogel, A. (2009). *Basic clinical radiobiology*. Hodder Arnold London.
- [Joiner and der Kogel, 2016] Joiner, M. C. and der Kogel, A. (2016). *Basic clinical radiobiology*. CRC press.
- [Kamada et al., 2015] Kamada, T., Tsujii, H., Blakely, E. A., Debus, J., De Neve, W., Durante, M., Jäkel, O., Mayer, R., Orecchia, R., and Pötter, R. (2015). Carbon ion radiotherapy in Japan: an assessment of 20 years of clinical experience. *The Lancet Oncology*, 16(2):e93–e100.
- [Kanai et al., 1999] Kanai, T., Endo, M., Minohara, S., Miyahara, N., Koyama-Ito, H., Tomura, H., Matsufuji, N., Futami, Y., Fukumura, A., Hiraoka, T., Furusawa, Y., Ando, K., Suzuki, M., Soga, F., and Kawachi, K. (1999). Biophysical characteristics of HI-MAC clinical irradiation system for heavy-ion radiation therapy. *International Journal of Radiation Oncology Biology Physics*, 44(1):201–210.
- [Kanai et al., 1997] Kanai, T., Furusawa, Y., Fukutsu, K., Itsukaichi, H., Eguchi-Kasai, K., and Ohara, H. (1997). Irradiation of mixed beam and design of spread-out Bragg peak for heavy-ion radiotherapy. *Radiation Research*, 147(1):78–85.

- [Kanai et al., 2006] Kanai, T., Matsufuji, N., Miyamoto, T., Mizoe, J., Kamada, T., Tsuji, H., Kato, H., Baba, M., and Tsujii, H. (2006). Examination of GyE system for HIMAC carbon therapy. *Int J Radiat Oncol Biol Phys*, 64(2):650–656.
- [Kaur et al., 2013] Kaur, H., Pujari, G., Semwal, M. K., Sarma, A., and Avasthi, D. K. (2013). In vitro studies on radiosensitization effect of glucose capped gold nanoparticles in photon and ion irradiation of HeLa cells. *Nuclear Instruments and Methods in Physics Research Section B: Beam Interactions with Materials and Atoms*, 301:7–11.
- [Kim et al., 2012] Kim, J.-K., Seo, S.-J., Kim, H.-T., Kim, K.-H., Chung, M.-H., Kim, K.-R., and Ye, S.-J. (2012). Enhanced proton treatment in mouse tumors through proton irradiated nanoradiator effects on metallic nanoparticles. *Physics in medicine and biology*, 57(24):8309–23.
- [Kočiček et al., 2013] Kočiček, J., Lengyel, J., Fárnik, M., and Slavíček, P. (2013). Energy and charge transfer in ionized argon coated water clusters. *Journal of Chemical Physics*, 139(21):214308.
- [Koong et al., 2000] Koong, A. C., Mehta, V. K., Le, Q. T., Fisher, G. A., Terris, D. J., Brown, J. M., Bastidas, A. J., and Vierra, M. (2000). Pancreatic tumors show high levels of hypoxia. *International Journal of Radiation Oncology* Biology* Physics*, 48(4):919–922.
- [Kotb et al., 2016a] Kotb, S., Detappe, A., Lux, F., Appaix, F., Barbier, E. L., Tran, V. L., Plissonneau, M., Gehan, H., Lefranc, F., Rodriguez-Lafrasse, C., Verry, C., Berbeco, R., Tillement, O., and Sancey, L. (2016a). Gadolinium-based nanoparticles and radiation therapy for multiple brain melanoma metastases: Proof of concept before phase I trial. *Theranostics*, 6(3):418–427.
- [Kotb et al., 2016b] Kotb, S., Detappe, A., Lux, F., Appaix, F., Barbier, E. L., Tran, V.-L., Plissonneau, M., Gehan, H., Lefranc, F., Rodriguez-Lafrasse, C., Verry, C., Berbeco, R., Tillement, O., and Sancey, L. (2016b). Gadolinium-Based Nanoparticles and Radiation Therapy for Multiple Brain Melanoma Metastases: Proof of Concept before Phase I Trial. *Theranostics*, 6(3):418–27.
- [Kraft, 2000] Kraft, G. (2000). Tumor therapy with heavy charged particles. *Progress in Particle and Nuclear Physics*, 45(Supplement 2):S473–S544.
- [Krämer, 1995] Krämer, M. (1995). Calculation of heavy-ion track structure. *Nuclear Inst. and Methods in Physics Research, B*, 105(1-4):14–20.

- [Krämer and Kraft, 1994] Krämer, M. and Kraft, G. (1994). Calculations of heavy-ion track structure. *Radiation and Environmental Biophysics*, 33(2):91–109.
- [Krause, 1979] Krause, M. O. (1979). Atomic radiative and radiationless yields for K and L shells. *Journal of Physical and Chemical Reference Data*, 8(2):307–327.
- [Laprie et al., 2015] Laprie, A., Hu, Y., Alapetite, C., Carrie, C., Habrand, J. L., Bolle, S., Bondiau, P. Y., Ducassou, A., Huchet, A., Bertozzi, A. I., Perel, Y., Moyal, and Balosso, J. (2015). Paediatric brain tumours: A review of radiotherapy, state of the art and challenges for the future regarding protontherapy and carbontherapy.
- [LaVerne, 2000] LaVerne, J. A. (2000). Track Effects of Heavy Ions in Liquid Water. *Radiation Research*, 153(5):487–496.
- [Lee et al., 2009] Lee, J. H., Cha, K. E., Kim, M. S., Hong, H. W., Chung, D. J., Ryu, G., and Myung, H. (2009). Nanosized polyamidoamine (PAMAM) dendrimer-induced apoptosis mediated by mitochondrial dysfunction. *Toxicology Letters*, 190(2):202–207.
- [Lesniak et al., 2010] Lesniak, A., Campbell, A., Monopoli, M. P., Lynch, I., Salvati, A., and Dawson, K. A. (2010). Serum heat inactivation affects protein corona composition and nanoparticle uptake. *Biomaterials*, 31(36):9511–9518.
- [Li et al., 2016] Li, S., Penninckx, S., Karmani, L., Heuskin, A.-C., Watillon, K., Marega, R., Zola, J., Corvaglia, V., Genard, G., Gallez, B., Feron, O., Martinive, P., Bonifazi, D., Michiels, C., and Lucas, S. (2016). LET-dependent radiosensitization effects of gold nanoparticles for proton irradiation. *Nanotechnology*, 27(45):455101.
- [Lin et al., 2015] Lin, Y., McMahon, S. J., Paganetti, H., and Schuemann, J. (2015). Biological modeling of gold nanoparticle enhanced radiotherapy for proton therapy. *Physics in Medicine & Biology*, (MAY):4149.
- [Liu et al., 2015] Liu, Y., Liu, X., Jin, X., He, P., Zheng, X., Dai, Z., Ye, F., Zhao, T., Chen, W., and Li, Q. (2015). The dependence of radiation enhancement effect on the concentration of gold nanoparticles exposed to low- and high-LET radiations. *Physica Medica*, 31(3):210–218.
- [Lousada et al., 2016] Lousada, C. M., Soroka, I. L., Yagodzinsky, Y., Tarakina, N. V., Todoshchenko, O., Hänninen, H., Korzhavyi, P. A., and Jonsson, M. (2016). Gamma radiation induces hydrogen absorption by copper in water. *Scientific Reports*, 6(1):24234.

- [Ma and Lomax, 2013] Ma, C.-M. M. and Lomax, A. J. (2013). *Proton and Carbon Ion Therapy*. Taylor & Francis.
- [María et al., 2013] María, T., Goerne, L., La Colaboración De María De Lourdes, C., Olivares, P. R., Patiño, J. G., Elisa, E., and Islas, O. (2013). *Nanomedicina Catalítica: Ciencia y Cáncer*. Arkhé edic edition.
- [Martinez-Rovira and Prezado, 2015] Martinez-Rovira, I. and Prezado, Y. (2015). Evaluation of the local dose enhancement in the combination of proton therapy and nanoparticles. *Med Phys*, 42(11):6703–6710.
- [Maurizot, 2008] Maurizot, M. S. (2008). *Radiation chemistry: from basics to applications in material and life sciences*. EDP Sciences.
- [McMahon et al., 2011] McMahon, S. J., Hyland, W. B., Muir, M. F., Coulter, J. A., Jain, S., Butterworth, K. T., Schettino, G., Dickson, G. R., Hounsell, A. R., O’Sullivan, J. M., Prise, K. M., Hirst, D. G., and Currell, F. J. (2011). Biological consequences of nanoscale energy deposition near irradiated heavy atom nanoparticles. *Sci Rep*, 1:18.
- [Miladi et al., 2014] Miladi, I., Alric, C., Dufort, S., Mowat, P., Dutour, A., Mandon, C., Laurent, G., Bräuer-Krisch, E., Herath, N., Coll, J. L., Dutreix, M., Lux, F., Bazzi, R., Billotey, C., Janier, M., Perriat, P., Le Duc, G., Roux, S., and Tillement, O. (2014). The in vivo radiosensitizing effect of gold nanoparticles based mri contrast agents. *Small*, 10(6):1116–1124.
- [Mozumder and Hatano, 2004] Mozumder, A. and Hatano, Y. (2004). *Charged particle and photon interactions with matter : chemical, physicochemical, and biological consequences with applications*. Marcel Dekker.
- [Neun and Stern, 2011] Neun, B. W. and Stern, S. T. (2011). Monitoring lysosomal activity in nanoparticle-treated cells. *Methods Mol Biol*, 697:207–212.
- [Niklas et al., 2013] Niklas, M., Greilich, S., Melzig, C., Akselrod, M. S., Debus, J., Jäkel, O., and Abdollahi, A. (2013). Engineering cell-fluorescent ion track hybrid detectors. *Radiation Oncology*, 8(1):141.
- [Noda et al., 2017] Noda, K., Furukawa, T., Fujimoto, T., Hara, Y., Inaniwa, T., Iwata, Y., Katagiri, K., Kanematsu, N., Mizushima, K., Mori, S., Saotome, N., Saraya, Y., Sato, S., Shirai, T., Takada, M., Takei, Y., Tansyo, R., and Yonai, S. (2017). Recent progress and future plans of heavy-ion cancer radiotherapy with HIMAC. *Nuclear Instruments and Methods in Physics Research Section B: Beam Interactions with Materials and Atoms*.

- [Polf et al., 2011] Polf, J. C., Bronk, L. F., Driessen, W. H., Arap, W., Pasqualini, R., and Gillin, M. (2011). Enhanced relative biological effectiveness of proton radiotherapy in tumor cells with internalized gold nanoparticles. *Appl Phys Lett*, 98(19):193702.
- [Porcel et al., 2010] Porcel, E., Liehn, S., Remita, H., Usami, N., Kobayashi, K., Furusawa, Y., Le Sech, C., and Lacombe, S. (2010). Platinum nanoparticles: a promising material for future cancer therapy? *Nanotechnology*, 21(8):85103.
- [Porcel et al., 2014] Porcel, E., Tillement, O., Lux, F., Mowat, P., Usami, N., Kobayashi, K., Furusawa, Y., Le Sech, C., Li, S., and Lacombe, S. (2014). Gadolinium-based nanoparticles to improve the hadrontherapy performances. *Nanomedicine : nanotechnology, biology, and medicine*, 10(8):1601–8.
- [Rahbari et al., 2009] Rahbari, R., Sheahan, T., Modes, V., Collier, P., Macfarlane, C., and Badge, R. M. (2009). A novel L1 retrotransposon marker for HeLa cell line identification. *Biotechniques*, 46(4):277.
- [Raimundo, 2014] Raimundo, N. (2014). Mitochondrial pathology: Stress signals from the energy factory.
- [Rima et al., 2013] Rima, W., Sancey, L., Aloy, M. T., Armandy, E., Alcantara, G. B., Epicier, T., Malchère, A., Joly-Pottuz, L., Mowat, P., Lux, F., Tillement, O., Burdin, B., Rivoire, A., Boulé, C., Anselme-Bertrand, I., Pourchez, J., Cottier, M., Roux, S., Rodriguez-Lafrasse, C., and Perriat, P. (2013). Internalization pathways into cancer cells of gadolinium-based radiosensitizing nanoparticles. *Biomaterials*, 34(1):181–195.
- [Römer et al., 2006] Römer, W., Wu, T. D., Duchambon, P., Amessou, M., Carrez, D., Johannes, L., and Guerin-Kern, J. L. (2006). Sub-cellular localisation of a ¹⁵N-labelled peptide vector using NanoSIMS imaging. *Applied Surface Science*, 252(19):6925–6930.
- [Roots and Okada, 1972] Roots, R. and Okada, S. (1972). Protection of DNA Molecules of Cultured Mammalian Cells from Radiation-induced Single-strand Scissions by Various Alcohols and SH Compounds. *International Journal of Radiation Biology and Related Studies in Physics, Chemistry and Medicine*, 21(4):329–342.
- [Schardt, 2016] Schardt, D. (2016). Hadrontherapy. In *Basic Concepts in Nuclear Physics: Theory, Experiments and Applications*, pages 55–86.

- [Schardt et al., 2010] Schardt, D., Elsässer, T., and Schulz-Ertner, D. (2010). Heavy-ion tumor therapy: Physical and radiobiological benefits.
- [Schicker et al., 2009] Schicker, C., von Neubeck, C., Kopf, U., and Kraft-Weyrather, W. (2009). Patent: Ep 09 002 402.7.
- [Schlatholter et al., 2016] Schlatholter, T., Eustache, P., Porcel, E., Salado, D., Stefanikova, L., Tillement, O., Lux, F., Mowat, P., Biegun, A. K., van Goethem, M. J., Remita, H., and Lacombe, S. (2016). Improving proton therapy by metal-containing nanoparticles: nanoscale insights. *Int J Nanomedicine*, 11:1549–1556.
- [Schoemers et al., 2015] Schoemers, C., Feldmeier, E., Naumann, J., Panse, R., Peters, A., and Haberer, T. (2015). The intensity feedback system at Heidelberg Ion-Beam Therapy Centre. *Nuclear Instruments and Methods in Physics Research Section A: Accelerators, Spectrometers, Detectors and Associated Equipment*, 795:92–99.
- [Scholz and Kraft, 1996] Scholz, M. and Kraft, G. (1996). Track structure and the calculation of biological effects of heavy charged particles. *Advances in Space Research*, 18(1-2):5–14.
- [Scifoni et al., 2013] Scifoni, E., Tinganelli, W., Weyrather, W. K., Durante, M., Maier, A., and Kramer, M. (2013). Including oxygen enhancement ratio in ion beam treatment planning: model implementation and experimental verification. *Phys Med Biol*, 58(11):3871–3895.
- [Sedgwick, 2012] Sedgwick, P. (2012). Pearson’s correlation. *Statistics*, 1:1–4.
- [Seltzer et al., 2011a] Seltzer, S. M., Bartlett, D. T., Burns, D. T., Dietze, G., Menzel, H.-G., Paretzke, H. G., Wambersie, A., and Tada, J. (2011a). Fundamental Quantities And Units For Ionizing Radiation (Revised) ICRU-report No 85. *Journal of the ICRU*, 11(1):1–35.
- [Seltzer et al., 2011b] Seltzer, S. M., Bartlett, D. T., Burns, D. T., Dietze, G., Menzel, H.-G., Paretzke, H. G., Wambersie, A., and Tada, J. (2011b). Fundamental Quantities And Units For Ionizing Radiation (Revised) ICRU-report No 85. *Journal of the ICRU*, 11(1):1–35.
- [Shapero et al., 2011] Shapero, K., Fenaroli, F., Lynch, I., Cottell, D. C., Salvati, A., and Dawson, K. A. (2011). Time and space resolved uptake study of silica nanoparticles by human cells. *Molecular bioSystems*, 7(2):371–8.

- [Shi et al., 2010] Shi, H., He, X., Yuan, Y., Wang, K., and Liu, D. (2010). Nanoparticle-based biocompatible and long-life marker for lysosome labeling and tracking. *Analytical Chemistry*, 82(6):2213–2220.
- [Shinohara et al., 1996] Shinohara, K., Nakano, H., and Ohara, H. (1996). Detection of Auger Enhancement Induced in HeLa Cells Labeled with Iododeoxyuridine and Irradiated with 150 Kv X-Rays: Effects of Cysteamine and Dimethylsulfoxide. *Acta Oncologica*, 35(7):869–875.
- [Štefančíková et al., 2014] Štefančíková, L., Porcel, E., Eustache, P., Li, S., Salado, D., Marco, S., Guerquin-Kern, J.-L., Réfrégiers, M., Tillement, O., and Lux, F. (2014). Cell localisation of gadolinium-based nanoparticles and related radiosensitising efficacy in glioblastoma cells. *Cancer Nanotechnology*, 5(1):6.
- [Sun et al., 2011] Sun, X., Niu, G., Chan, N., Shen, B., and Chen, X. (2011). Tumor Hypoxia Imaging. *Molecular Imaging and Biology*, 13(3):399–410.
- [Taggart et al., 2014] Taggart, L. E., McMahon, S. J., Currell, F. J., Prise, K. M., and Butterworth, K. T. (2014). The role of mitochondrial function in gold nanoparticle mediated radiosensitisation. *Cancer nanotechnology*, 5(1):5.
- [Tan et al., 1986] Tan, M. H., Nowak, N. J., Loo, R., Ochi, H., Sandberg, A. A., Lopez, C., Pickren, J. W., Berjian, R., Douglass, H. O., and Chu, T. M. (1986). Characterization of a new primary human pancreatic tumor line. *Cancer investigation*, 4(1):15–23.
- [Terasawa et al., 2009] Terasawa, T., Dvorak, T., Ip, S., Raman, G., Lau, J., and Trikalinos, T. a. (2009). Review Annals of Internal Medicine Systematic Review : Charged-Particle Radiation Therapy for Cancer. (5).
- [Thambi et al., 2014] Thambi, T., Deepagan, V. G., Yoon, H. Y., Han, H. S., Kim, S. H., Son, S., Jo, D. G., Ahn, C. H., Suh, Y. D., Kim, K., Chan Kwon, I., Lee, D. S., and Park, J. H. (2014). Hypoxia-responsive polymeric nanoparticles for tumor-targeted drug delivery. *Biomaterials*, 35(5):1735–1743.
- [Thomlinson and Gray, 1955] Thomlinson, R. H. and Gray, L. H. (1955). The Histological Structure of Some Human Lung Cancers and the Possible Implications for Radiotherapy. *British journal of cancer*, 9:539–549.
- [Torikoshi et al., 2007] Torikoshi, M., Minohara, S., Kanematsu, N., Komori, M., Kanazawa, M., Noda, K., Miyahara, N., Itoh, H., Endo, M., and Kanai, T. (2007). Irradiation System for HIMAC. *Journal of radiation research*, 48 Suppl A:A15–A25.

- [Tubiana M., Dutreix J., 1990] Tubiana M., Dutreix J., W. A. (1990). Introduction to Radiobiology. *Medical Physics*, page 371.
- [Twentyman, 1993] Twentyman, P. (1993). The Basic Science of Oncology. 2nd Edition. *British Journal of Cancer*, 67(5):1159.
- [Usami et al., 2005] Usami, N., Furusawa, Y., Kobayashi, K., Frohlich, H., Lacombe, S., and Le Sech, C. (2005). Fast He²⁺ ion irradiation of DNA loaded with platinum-containing molecules. *International journal of radiation biology*, 81(7):515–22.
- [Usami et al., 2008] Usami, N., Furusawa, Y., Kobayashi, K., Lacombe, S., Reynaud-Angelin, A., Sage, E., Wu, T. D., Croisy, A., Guerquin-Kern, J. L., and Le Sech, C. (2008). Mammalian cells loaded with platinum-containing molecules are sensitized to fast atomic ions. *Int J Radiat Biol*, 84(7):603–611.
- [Vaupel et al., 1989] Vaupel, P., Kallinowski, F., and Okunieff, P. (1989). Blood flow, oxygen and nutrient supply, and metabolic microenvironment of human tumors: a review. *Cancer research*, 49(23):6449–65.
- [Verkhovtsev et al., 2014a] Verkhovtsev, A. V., Korol, A. V., and Solov, A. V. (2014a). Electron Production by Sensitizing Gold Nanoparticles Irradiated by Fast Ions.
- [Verkhovtsev et al., 2014b] Verkhovtsev, A. V., Korol, A. V., and Solov'yov, A. V. (2014b). Revealing the Mechanism of Low-Energy Electron Yield Enhancement from Sensitizing Nanoparticles. page 6.
- [Verry et al., 2016] Verry, C., Dufort, S., Barbier, E. L., Montigon, O., Peoc'h, M., Chartier, P., Lux, F., Balosso, J., Tillement, O., Sancey, L., and Le Duc, G. (2016). MRI-guided clinical 6-MV radiosensitization of glioma using a unique gadolinium-based nanoparticles injection. *Nanomedicine*, 11(18):2405–2417.
- [Walter Tinganelli, 2012] Walter Tinganelli (2012). Influence of LET and oxygen status on cell survival and adhesion molecule expression.
- [Walzlein et al., 2014] Walzlein, C., Scifoni, E., Kramer, M., and Durante, M. (2014). Simulations of dose enhancement for heavy atom nanoparticles irradiated by protons. *Phys Med Biol*, 59(6):1441–1458.
- [Wishart and Rao, 2010] Wishart, J. F. and Rao, B. S. M. (2010). Recent Trends in Radiation Chemistry. (April 2014):607.

- [Wozny et al., 2017] Wozny, A.-S., Aloy, M.-T., Alphonse, G., Magné, N., Janier, M., Tillement, O., Lux, F., Beuve, M., and Rodriguez-Lafrasse, C. (2017). Gadolinium-based nanoparticles as sensitizing agents to carbon ions in head and neck tumor cells. *Nanomedicine: Nanotechnology, Biology and Medicine*.
- [Yamashita et al., 2008] Yamashita, S., Katsumura, Y., Lin, M., Muroya, Y., Miyazaki, T., and Murakami, T. (2008). Water radiolysis with heavy ions of energies up to 28 GeV. 1. Measurements of primary g values as track segment yields. *Radiation Physics and Chemistry*, 77(4):439–446.
- [Ziegler, 1998] Ziegler, J. (1998). RBS/ERD simulation problems: Stopping powers, nuclear reactions and detector resolution. *Nuclear Instruments and Methods in Physics Research Section B: Beam Interactions with Materials and Atoms*, 136-138(97):141–146.
- [Zinchuk and Grossenbacher-Zinchuk, 2011] Zinchuk, V. and Grossenbacher-Zinchuk, O. (2011). Quantitative colocalization analysis of confocal fluorescence microscopy images. *Current Protocols in Cell Biology*, (SUPPL. 52):4.16.1–4.16.19.

Annex A. List of publications

Bolsa, M.; Boscolo, D.; Porcel, E.; Lacombe, S.; Sokol, S.; Wiedemann, J.; Scifoni, E.; Tinganelli, W.; Jakob, B.; Roux, S.; Jimenez, G.; Durante, M.; and Kraemer, M. (2016). Nanoparticles radio-enhancement of ion beams at different oxygenation conditions. GSI SCIENTIFIC REPORT 2016.

Bolsa Ferruz, M.; Ivo[˘]sev, V.; Haume, K.; Ellis-Gibbins, L.; Traore, A.; Thakare, V.; Rosa, S.; de Vera, P.; Tran, V.-L.; Mika, A.; Boscolo, D.; Grellet, S.; Verkhovtsev, A.; Huber, B.; Butterworth, K. T.; Prise, K. M.; Currell, F. J.; Mason, N.; Golding, J.; Scifoni, E.; Garcia, G.; Boschetti, F.; Lux, F.; Tillement, O.; Louis, C.; Stokbro, K.; Solov'yov, Andrey V. and Lacombe, S. (2016). New Research in Ionizing Radiation and Nanoparticles: The ARGENT Project. In: Solov'yov, Andrey V. ed. Nanoscale insights into ion-beam cancer therapy. Cham: Springer International Publishing, pp. 379–434.

Annex B. Synthèse en français

De nos jours, le cancer est devenu l'une des premières causes de mortalité, notamment dans les pays développés. La chirurgie, la radiothérapie et la chimiothérapie en constituent les principales méthodes de traitement. La radiothérapie dite « conventionnelle », basée sur l'utilisation de rayons X de haute énergie (2-30 MV), permet de traiter des tumeurs situées en profondeur de manière non-invasive.

Malheureusement, les rayons endommagent également des cellules saines sur leur passage, ce qui peut induire des effets secondaires. C'est pourquoi d'importants efforts sont déployés afin de limiter l'exposition des tissus sains aux radiations. Des améliorations majeures dans la radiothérapie conventionnelle sont associées à des progrès technologiques significatifs tels que des outils de diagnostic et des systèmes de délivrance de faisceaux plus efficaces [Bhide and Nutting, 2010]. Une approche prometteuse consiste à introduire des nanoparticules métalliques (NPs) dans la tumeur, ce qui a pour effet d'y amplifier les effets radiatifs dans le volume cible. La dose totale de radiation peut ainsi être diminuée sans pour autant réduire l'efficacité du traitement. Le nombre de travaux publiés dans la presse spécialisée est en train d'exploser et les premiers essais cliniques utilisant des nanoagents composés d'éléments lourds tels que l'hafnium (NBTXR3) [Bonvalot et al., 2017] et le gadolinium (AGuIX) [Kotb et al., 2016b, Verry et al., 2016] (développés respectivement par les sociétés Nanobiotix à Paris et Nano-H à Saint-Quentin Fallavier, France) ont montré des résultats prometteurs en ce qui concerne l'association de la nanomédecine avec la radiothérapie conventionnelle.

Malgré ces développements qui améliorent significativement la radiothérapie conventionnelle, l'utilisation de photons hautement pénétrants demeure problématique pour le traitement de tumeurs situées au sein d'organes fragiles (cerveau, yeux, etc.) [Kraft, 2000] ou bien dans les cas de traitements pédiatriques [Laprie et al., 2015]. En outre, certaines formes de cancer semblent résister à la radiothérapie conventionnelle. C'est

le cas notamment des tumeurs contenant des régions faiblement oxygénées (également appelées régions hypoxiques).

Une technique plus récente, appelée hadronthérapie, pourrait surmonter ces limitations. Elle consiste à utiliser des faisceaux d'ions accélérés à de hautes énergies (70 à 400 MeV/u). Le principal avantage de cette technique tient au fait que les ions déposent la quasi-totalité de leur énergie à la fin de leur trajectoire. En choisissant correctement l'énergie du faisceau, il est possible de faire en sorte que le dépôt d'énergie se fasse dans la tumeur. Un autre avantage de l'hadronthérapie est lié à la nature complexe des dommages induits par les ions, ce qui permet de réduire la dépendance aux concentrations d'oxygène.

En hadronthérapie, le dépôt d'énergie en amont de la tumeur est faible, mais pas négligeable pour autant. Afin d'améliorer cela, l'équipe de recherche du laboratoire ISMO a proposé une nouvelle stratégie basée sur l'utilisation des nanoparticules pour amplifier les effets radiatifs des ions au sein de la tumeur [Porcel et al., 2010]. L'hadronthérapie étant utilisée pour traiter les tumeurs contenant des cellules hypoxiques, il est primordial de se poser la question suivante : l'effet amplificateur des nanoparticules dépend-il de la concentration d'oxygène ? Le but de ma thèse a été de répondre à cette question.

Des expériences ont été menées sur deux lignées cellulaires cancéreuses humaines : HeLa (col de l'utérus) et BxPC3 (pancréas). Deux types de nanoparticules (environ 3 nm de diamètre) ont été utilisées : or (AuNPs) et platine (PtNPs). Plusieurs techniques d'irradiation ont été mises en place : des faisceaux d'ions carbone (TEL¹ = 50 keV/ μ m) et hélium (TEL = 12 keV/ μ m) délivré par « passive scattering » (HIMAC, Chiba, Japon) et des faisceaux d'ions carbone délivré par « pencil beam scanning (PBS) » (HIT, Heidelberg, Allemagne). Les expériences ont été réalisées dans trois conditions d'oxygénation différentes ($pO_2 = 0, 0.5$ et 20%).

Les premiers résultats concernent l'internalisation et la localisation des NPs dans les cellules cancéreuses. Découverte importante, les PtNPs et AuNPs sont exclusivement situées dans le cytoplasme. En particulier, les AuNPs se concentrent dans les mitochondries des cellules HeLa, tandis qu'elles sont co-localisées avec les lysosomes dans les cellules BxPC-3.

En l'absence de nanoparticules, les expériences en « passive scattering » ont montré que les dommages causés par des radiations avec un TEL élevé (ions carbone) sont plus

¹TEL, transfert d'énergie linéique

létaux que pour des TEL plus faibles (ions hélium). Cela s'explique par la présence de dommages complexes causés à l'ADN. Par ailleurs, les effets radiatifs augmentent avec la concentration en oxygène. Les molécules d'O₂ ont en effet la capacité de « fixer » des dommages causés par l'irradiation, rendant ainsi les lésions permanentes [Furusawa et al., 2000, Brown and Wilson, 2004]. Toutefois, cet effet sensibilisateur de l'oxygène - exprimé par l'OER (oxygen enhancement ratio) - diminue lorsque le TEL augmente [Scifoni et al., 2013]. Cette dépendance est attribuée à la production de dommages complexes pour lesquels la létalité ne dépend pas de leur « fixation » par l'oxygène.

En présence de nanoparticules, les résultats ne sont pas significativement différents pour les deux types de NPs et pour les deux lignées cellulaires. Les effets amplificateurs dépendent essentiellement des conditions d'irradiation (ions carbone ou hélium, irradiation par passive scattering ou par PBS) et de la concentration en oxygène.

En condition oxygène, les expériences ont mis en évidence une amplification significative des effets radiatifs par les PtNPs et les AuNPs (carbone 50 keV/μm et hélium 12 keV/μm - passive scattering, et ions carbone 100 keV/μm - PBS). Cela s'explique par une succession d'effets à l'échelle nanoscopique : i) amplification de l'émission d'électron dans le voisinage immédiat des NPs, ii) production de radicaux libres, iii) mort cellulaire par action des radicaux libres ou des électrons.

A noter que les perturbations dues aux NPs sont déclenchées exclusivement dans le cytoplasme. Or les effets radiatifs résultent du cumul des dommages causés dans le noyau et des perturbations cytoplasmiques. L'effet amplificateur des NPs dépend donc non seulement de la capacité du faisceau incident à les activer, mais également de la contribution relative des perturbations cytoplasmique à la mort cellulaire.

En mode PBS, l'effet des NPs sur l'irradiation par ions carbone a été testé pour la première fois. Dans ces conditions, il a été établi que les NPs amplifient les effets radiatifs lorsque le TEL est de 100 keV/μm, mais pas de 50 keV/μm. Cela s'explique par le fait que l'activation des NPs augmente avec la densité d'ionisation, ce qui conduit à la production de lésions complexes dans le milieu cytoplasmique.

Autre contribution importante, mon travail a permis de comprendre les mécanismes de radio amplification en modifiant la concentration en oxygène. Si les effets radiatifs ne sont amplifiés qu'en condition oxygène, cela signifie que le phénomène de « fixation » des lésions par l'oxygène joue un rôle majeur et augmente significativement la contribution du cytoplasme dans le processus de mort cellulaire. C'est le cas des ions carbone, TEL

= 50 keV/ μm - passive scattering. A l'inverse, si l'amplification est également observée en condition anoxique, on en déduit que les NPs amplifient la production de dommages complexes ou de molécules toxiques comme H_2O_2 dans le cytoplasme. C'est le cas des ions carbone, TEL = 100 keV/ μm , PBS, et des ions hélium, TEL = 12 keV/ μm .

En conclusion, ce travail a mis en évidence le potentiel des NPs à améliorer les techniques d'hadronthérapie, en conditions oxygène, hypoxique et anoxique. Leur utilisation pourrait en effet permettre d'amplifier les effets radiatifs dans la tumeur, et donc de réduire la dose totale administrée aux patients. L'efficacité de cette combinaison de techniques dépend cependant des conditions d'irradiation.

La conception de nano-agents contenant des émetteurs d'électron et capables d'atteindre les régions hypoxiques représente un autre défi important. Par contraste, des nano-agents pourraient être conçus pour se concentrer dans les régions périphériques oxygénées de la tumeur. Cela permettrait d'en délimiter les contours et de traiter efficacement ces extensions périphériques, sans augmenter la dose totale dans les tissus sains. Les nano-agents ouvrent également la perspective de transporter des composants multimodaux capables non seulement d'amplifier les effets radiatifs, mais également d'améliorer l'imagerie médicale (gadolinium par exemple).

Enfin, cette thèse a contribué à une meilleure compréhension du rôle de l'oxygène et du protocole d'irradiation mis en place dans la radio-amplification par les NPs.

Acknowledgements

Thanks to... Gracias a... Merci à...

Pr. Lacombe, my thesis director, for giving me the opportunity to conduct this research project and challenging me along the way. Thanks for the scientific discussions we had all around the world. Dr. Porcel, my co-supervisor, for sharing her knowledge and skills with me. Thanks for her support as well as for the pleasant city tours we had between the experiments.

Dr. Hirayama, for welcoming me in his laboratory and teaching me his expertise. Thanks to my colleagues at NIRS for their hospitality and the unforgettable moments we had. You made me discover the taste of Japan! Unagi has become my absolute favorite dish. Thanks to Pr. Furusawa, for his wise advises and his kindness. I would also like to thank to NIRS and HIMAC for the beam time provided to this project and the use of the facilities.

My colleagues from GSI and TIFPA for the fruitful collaboration and for all I could learn from working with them. Thanks for the great atmosphere during the shifts (and the uncountable hours of “cut and paste”!) and outside the lab (Darmstadt and its butter-filled pretzel). I would also like to thank to HIT and GSI for the beam time provided to this project and the use of the facilities.

To all the ARGENT Project, for the opportunity of developing my thesis in an unique environment, the summer school, trainings and divers project meetings. Thanks to the ESRs for all the good time we shared. Thanks to all supervisors for guiding us along the research. Thanks to the managers for helping me to follow the European requests. Thanks to the SERP-Chem professors and in particular, to Pr. Mostafavi for the valuable discussions.

Pr. Roux, for making gold nanoparticles available in this project and for his precious knowledge. Thanks to Gloria, not only for the synthesis but for her reactivity and professional, as well as personal, support.

Frank, for training me at SOLEIL synchrotron and for all the insightful discussions.

Sandrine, pour m'avoir accueillie au CLUPS toujours avec un grand sourire. Merci d'avoir toujours volé à mon secours.

My colleagues at ISMO, for all those coffees and relaxed chats. Thanks to Sylvie for her immense patience and kindness. My PhD experience would not have been fulfilled without the laughs, the trips, the soirées. . . with my office- and PhD- mates. To whom, I am very thankful. Thanks Fiona and Michaela for supporting some of the experiments. I hope you enjoyed your time at ISMO as much as I appreciated your company. Thanks to Lenka for bringing joy to the lab. Thanks to Daniela, for providing PtNPs to my project as well as for being my PhD mentor and helping me through all these years.

My friends in Japan, for listening to me anytime at NIRS or at the karaoke. Mis amigos, que, desde España, Francia, Suiza y Polonia, siempre encontraron el momento de llamarme, de coger el coche, el tren o el avión y abrazarme. Ma team chartreuse, pour m'avoir toujours attendue lorsque je revenais de voyage (inlassablement prêts pour chasser des zombies à Paris!).

Mi ángel de la guarda, por estar siempre a mi lado: pasando de compartir el día a día a estar separadas por el océano. Por todos y cada uno de los recuerdos que coleccionamos.

Mon cher, mon coach et cuisinier ! Pour les trajets en RER vers et depuis l'aéroport, ainsi que pour toutes les fois où nous avons partagé les voyages. Ton grand soutien, aide inconditionnelle et ton écoute ont été la pierre angulaire.

Mi tía y Santi, por reconfortarme en todo momento desde el otro lado del teléfono sin importar la hora ni el día. Mis padres, por aconsejarme y darme al mismo tiempo la libertad de tomar mis propias decisiones. Por haberme permitido llevar a cabo la aventura de estudiar en el extranjero, por los envíos de jamón, chocolate valor, las cartas. . . por estar a mi lado para celebrar cada victoria al igual que para superar las dificultades. Mi hermano, su ambición y perseverancia le han convertido en mi modelo a seguir. Gracias por tener siempre las palabras justas y haberme ayudado con sus consejos en cada etapa de mi carrera.

The research leading to these results has received funding from the People Programme (Marie Curie Actions) of the European Union's Seventh Framework Programme FP7/2007 - 2013/ under REA – Grant Agreement n° 608163.

This work was partially supported by the Japan Society for the Promotion of Science (JSPS) Postdoctoral fellowship program for North American and European researchers (FY2016).

Titre : Effet de l'oxygène dans l'irradiation par des ions médicaux combinés avec des nanoparticules

Mots clés : faisceau d'ions, hadronthérapie, nanoparticules, radio-sensibilisation

Résumé : Environ 50% des patients recevant un traitement contre le cancer bénéficient de la radiothérapie. La radiothérapie conventionnelle consiste à utiliser des rayons X de haute énergie capables de traverser les tissus et de traiter des tumeurs situées en profondeur de façon non-invasive. Malheureusement, les rayons X ne font pas la distinction entre les tumeurs et les tissus sains, qui peuvent donc être endommagés. Cette non-sélectivité est à l'origine de graves effets secondaires, voire du développement de cancers secondaires. Par conséquent, l'amplification des effets radiatifs au sein de la tumeur par rapport aux tissus environnants représente un défi majeur.

L'hadronthérapie (traitement par faisceaux de protons ou d'ions carbone) est considérée comme l'une des techniques les plus prometteuses car, contrairement aux rayons X, la quantité d'énergie déposée atteint son maximum en fin de trajectoire. Lorsque le faisceau est réglé de manière à ce que ce maximum atteigne la tumeur, aucun dommage n'est causé aux tissus situés au-delà. Un autre avantage majeur est que les ions lourds sont plus efficaces pour traiter les tumeurs radiorésistantes. L'utilisation de cette technique est cependant restreinte du fait des dommages – plus faibles mais néanmoins significatifs – causés aux tissus normaux situés sur la trajectoire du faisceau d'ions en amont de la tumeur.

Afin d'améliorer les performances de l'hadronthérapie, l'équipe a développé à l'ISMO une nouvelle stratégie combinant l'utilisation de nanoparticules (NPs) métalliques avec l'irradiation par faisceaux d'ions. L'utilisation de NPs a pour but non seulement d'amplifier les effets des rayonnements dans la tumeur mais également d'améliorer l'imagerie médicale à l'aide des mêmes agents (théranostic).

Les NPs possèdent une chimie de surface

permettant leur fonctionnalisation avec des ligands capable d'améliorer la biocompatibilité, la stabilité ainsi que la circulation sanguine et l'accumulation dans la tumeur. L'équipe a déjà démontré que les petites NPs d'or et de platine (≈ 3 nm) avaient la capacité d'amplifier les effets causés par les faisceaux d'ions carbone médicaux en présence d'oxygène. Cependant, les tumeurs radiorésistantes sont susceptibles de contenir des régions hypoxiques. Il est donc urgent de quantifier et de caractériser l'influence de l'oxygène sur l'effet radio-amplificateur.

Le but de ma thèse était d'étudier l'influence de l'oxygène lors d'irradiations par des faisceaux d'ions médicaux en présence de NPs d'or et de platine. Pour cela, deux lignes de cellules cancéreuses humaines radiorésistantes ont été testées: HeLa (col de l'utérus) et BxPC-3 (pancréas). Plusieurs techniques d'irradiation ont été utilisées : des faisceaux d'ions carbone et hélium générés par « passive scattering » et des faisceaux d'ions carbone générés par « pencil beam scanning ». Les principaux résultats de cette étude sont les suivants. En condition oxique (concentration d'O₂ = 20%), une amplification des effets radiatifs a été observée pour les deux types de NPs (à concentration de métal égale). Ce phénomène se réduit à mesure que la concentration d'oxygène diminue mais reste significatif jusqu'à 0.5%. Aucune différence significative n'a été observée entre les deux lignes cellulaires. Il est intéressant de noter que la dépendance à l'oxygène varie en fonction de la technique d'irradiation utilisée. Une tentative d'explication de l'influence de l'oxygène par des processus moléculaires est proposée. Des perspectives de développements ultérieurs sont suggérées.



Title : Oxygen effect in medical ion beam radiation combined with nanoparticles

Keywords : ion beam radiation, hadrontherapy, nanoparticles, radio-enhancement

Abstract : About 50% of the cancer patients who are treated benefit from radiation therapy. Conventional radiotherapy consists of high energy X-rays traveling through the tissues, so that deeply sited tumors are treated in a non-invasive way. Unfortunately, X-rays are not tumor selective and healthy tissues may be damaged. This lack of selectivity is responsible for severe side effects and/or secondary cancers. Hence, improving the differential of radiation effects between the tumor and surrounding tissues remains a major challenge.

Particle therapy (treatment by protons or carbon ion beams) is considered as one of the most promising technique because, by opposition to X-rays, the energy deposition of ions is maximum at the end of their tracks. When the beam is tuned so that the maximum reaches the tumor, there is no damage induced in tissues siting after the tumor. Another important added value is that heavy ions are more efficient to treat radioresistant tumors. The use of this modality is however restricted by the low but significant damage that is induced to normal tissues located at the entrance of the track prior to reaching the tumor.

To improve the performance of particle therapy, a new strategy based on the combination of high-Z nanoparticles with ion beam radiation has been developed by the group at ISMO. This approach aims at using nano-agents not only to increase radiation effects in the tumor but also to improve medical imaging with the same agent (theranostic). Nanoparticles present a remarkable surface chemistry, which allows functionalization with ligands able

to improve biocompatibility, stability as well as blood circulation and accumulation in tumors. The group already demonstrated the efficiency of small (≈ 3 nm) gold and platinum nanoparticles to amplify the effects of medical carbon ions in normoxic conditions (in the presence of oxygen). However, radioresistant tumors may host hypoxic regions. It is thus urgent to quantify and characterize the influence of oxygen on the radio-enhancement effect.

The goal of my thesis was to study the influence of oxygen on medical ion radiation effects in the presence of gold and platinum nanoparticles. This was performed using two radioresistant human cancer cell lines: HeLa (uterine cervix) and BxPC-3 (pancreas). Different radiation modalities were used: carbon and helium ion beams delivered by a passive scattering delivery system and carbon ion beams delivered by a pencil beam scanning system.

The major results of this work are the following. In oxidic conditions (O_2 concentration = 20%), an enhancement of ion radiation effects was observed for the two nanoparticles (at the same concentration in metal). This effect decreased with the oxygen concentration but remained significant for a concentration of 0.5%. No significant difference was found between the cell lines. Interestingly, the oxygen-dependence varied with the type of radiation.

An attempt to explain the effect of oxygen by molecular processes is proposed. Perspectives of further developments are suggested.

